Experimental and Numerical Investigations on the Hydrodynamic Loading of Tsunami-like Surges on Infrastructures

Shilong Liu

Thesis submitted to the University of Ottawa

in partial Fulfillment of the requirements for the

Doctorate in Philosophy degree in Civil Engineering

Department of Civil Engineering

Faculty of Engineering

University of Ottawa

Abstract

Tsunamis have caused severe damage to coastal communities and associated infrastructure over the past decades. Thus, researchers deemed necessary to investigate and better understand the mechanisms loading associated with tsunami waves and the inundation caused by them. Over the past few years, researchers have demonstrated that the dam-break waves are hydrodynamically similar to the onshore propagation of tsunami inundation; hence, dam-break waves are now widely used to investigate tsunami impacts. Various studies related to dam-break waves have been conducted to investigate their characteristics: the kinematic behavior, including free surface profiles, wave height, wave front velocity, and dynamics including the impact pressure and associated force. Most dam-break experiments have been conducted on a horizontal bed, in a tank or a flume, while few studies had employed sloped surfaces. However, natural and artificial beaches usually have slopes ranging from 0-degrees to 20-degrees (or more).

In this study, downstream slopes are considered to investigate the influence of slope effects on the kinematic behaviors and associated hydrodynamic loadings due to dam-break waves. The Volume of Fluid method (VOF) code of the OpenFOAM and the Smoothed Particle Hydrodynamics (SPH) code of the DualSPHysics were applied to reproduce the results of physical tests and provide a comparison with the experimental results. First, existing boundary treatment methods in the SPH were studied and compared to a self-developed code in order to select the best performing method by checking the flow behaviors. In the second part of the thesis, experimental investigation of the impact of dam-break induced surges over a horizontal bed against a vertical wall was conducted by analysing the rapidly varying correlation between the wave height and the associated dynamic pressure. In the third part of this study, three

different downstream slopes were added in the experimental setup to investigate the beach effects on the kinematics of dam-break flow, including the free surface profiles, wave height, wave front location and its velocity. In the last part, the impact dynamic pressure on the vertical straight wall from the horizontal and sloped cases were captured to investigate the slope effects on the hydrodynamic loading. The impact force integrated from the dynamic pressure was determined with a simplified calculation formula. In addition, the physical experiments were also reproduced by the numerical models of OpenFOAM and DualSPHysics to compare and investigate their accuracy and to analyze the differences between the physical tests and numerical simulations.

Acknowledgements

My deepest gratitude and appreciation go first and foremost to my supervisors, Prof. Nistor, Prof. Mohammadian and Prof. Azimi, for their high-standard supervision, professional guidance, valuable suggestions throughout my doctoral study, as well as the kind assistant and inspiring encouragement. The benefits I gained from my supervisors and their inputs will definitely and continuously have profound influence on me, and greatly enlighten me both in the current academic study and the future career.

Also thanks to Prof. Colin Rennie, Adjunct Prof. Xin Liu, Adjunct Prof. Hamidreza Shirkhani, whose suggestions and help on my study program and research project. I would like to thank the technical officer of Water Resources Engineering Laboratory, Mark Lapointe, with helping with the experimental setting; technical officer, Leo Denner, and graduate student and colleague Steven Douglas on transducers consulting and connecting; visiting student, Camille Paul from France and Geunse Lee from South Korea, on helping with the early stage of experimental setting; the Machine Shop, MarkerSpace, Brunsfield Centre at the Faculty of Engineering, and the CANUS Plastics Inc. in Ottawa.

I really appreciate the joint scholarships received from China Scholarship (CSC) University of Ottawa for my doctoral study and research, as well as the financial support from the Discovery grants of Drs. Ioan Nistor and Majid Mohammadian which are awarded by the Natural Science and Engineering Research Council of Canada (NSERC).

I would like to thank my parents, Yulu Liu and Rongmei Yuan, for their sincere love, earnest education and constant support on my study since I started school. I would like to thank my beloved wife, Shihui Wang, who gives me continuous and generous support on my study and

life, and endless love on taking care of our beloved son, Noah NuoAn Liu. My beloved wife and son not only bring me happiness in the life, but also encouragement on my study. I also would like to thank my parents-in-law, Guanghua Wang and Zhenjiao Liu, for their endless love on my wife and son, and their continuous support for us. I am so lucky to have this big family with endless love, supports and encouragements.

Last but not least, I would like to thank the group fellows and friends at University of Ottawa, for their friendship and help: Huade Cao, Xiaohui Yan, Xueming Wang, Saideh Kh, Iman Behreini, Kate Neigel, Hassan Y Alfaifi, Hossein Kheirkhah Gildeh, Jacob Stolle, Saber Ansari, Behnaz Ghodoosipou, Mohammad A. Gazizadeh, Amanj Jamal, Gabriella Mauti, Marieh Rajaie, Wenjun Zhang, Xinyun Wang, Xiatong Cai, and Yi Man.

Table of Contents

List of Figures

List of Tables

List of Symbols

c = sound speed, m/s;

C_d = drag coefficient;

D = depth of the ocean, m;

f = bed friction coefficient;

g = gravitational acceleration, m/s^2;

G = donated to the virtual/ghost particle;

h = wave height along the right wall, m;

h_0 = initial impoundment depth, m;

h_e = inundation height, m;

$h_{\max}$ = maximum wave elevation, m;

H = initial impoundment depth, m;

h_L = vertical distance of the interface above the location, m;

h_B = vertical distance of the interface above the lowest boundary, m;

Hz = frequency, s^{-1};

I_{tsu} = importance factor;

L = left;

L_0 = distance between the reservoir and the right wall, m;

m_i = mass of the particle, kg;

m_j = mass of the neighbouring particle, kg;

$m_{reference}$ = reference mass, kg;

N = total number of neighbouring particles of particle i;

p = pressure of the particle, Pa;

p_i = pressure of particle i, Pa;

P_i = pressure in the specified location, Pa;

P_j = pressure of the neighbouring particles, Pa;

P_x = dynamic pressure on the transducers, kPa;

q = discharge per unit width, m^2/s;

R = right;

t = time, s;

t_m = time since the initial impact, s;

T = characteristic time scale;

u = wave front velocity, m/s;

U = wave front velocity in wave tip region, m/s;

v = velocity,m/s;

v_i = velocity of particle i, m/s;

$v_{ij} = v_i - v_j$, velocity difference between particle i and j, m/s;

v_n = normal velocity, m/s;

v_t = tangential velocity, m/s;

w = tank width, m;

W_{ij} = kernel function;

x = horizontal direction, m;

x_1 = interface location between the main dam-break flow and the tip region, m;

x_s = coordinate of the wave front, m;

x_w =position of the rigid boundary, m;

X = horizontal direction;

Y = transverse direction;

Z = vertical direction, perpendicular to the XY plane;

z = elevation, mm;

α_{water} = phase fraction describes the volume in each computational cell;

γ = parameter, used as 7;

ε = a constant, in the range of $0 \le \varepsilon \le 1$;

η = force reduction factor;

θ = bed slope, °;

ρ = density, kg/m^3;

ρ_0 = reference density, $1000\,kg/m^3$;

ρ_i = density of particle i, kg/m$^{3;}$

ρ_j = density of neighbouring particle j, kg/m^3;

μ = dynamic viscosity, N·s/m^2;

Π_{ij} = artificial viscosity term;

List of Acronyms

ASCE = American Society of Civil Engineering;

ASIC = Application Specific Integrated Circuit;

CFD = Computation Fluid Dynamics;

CFL = Courant- Friedrichs-Lewy;

CIP = Constrained Interpolation Profile;

DAQ = Data Acquisition;

DBP = Dynamic Boundary Particle;

DualSPHysics = A combined CUDA and OpenMP implementation of the Smoothed Particle Hydrodynamics (SPH) method based on the advanced SPHysics codes;

GPU = Graphic Processing Unit;

HBM = an HBK company in testing and analysis;

HBK = Hottinger, Brüel & Kjær;

HPT = Honeywell Pressure Transducers;

LMPS = TE connectivity LM-series Pressure Sensor;

mDBC = modified dynamic boundary condition;

MPS = Moving Particle Semi-implicit;

MUSS = MASSA M-5000/220 Ultra-sonic sensor;

NOAA = National Oceanic and Atmospheric Administration;

N-S = Navier-Stokes;

OpenFOAM = Open-source Field Operation and Manipulation;

RANS – Reynolds-Averaged Navier-Stokes;

SMBTR = Structural Design Method of Buildings for Tsunami Resistance;

SPH = Smoothed Particle Hydrodynamics;

SPHysics = A open-source platform of Smoothed Particle Hydrodynamics (SPH) codes;

SST = Shear Stress Transport;

VOF = Volume of Fluid;

XSPH = corrected SPH method by using averaged velocity;

2D = two-dimensional;

3D = three-dimensional.

Chapter 1 Introduction

1.1 Introduction

Over the past decades, tsunami events have caused severe damage to coastal infrastructure and claimed many deaths in near-shore communities due to the extreme hydrodynamic loading, such as the 2004 Indian Ocean Tsunami, 2010 Chile Tsunami, 2011 Japan Tsunami, 2013 Solomon Islands Tsunami, 2015 Central Chile Tsunami, and 2018 Indonesia Tsunami. The coastal areas play an important role in the world as they contain high-density populations, tourism, the seafood industry and many other economic activities. In addition, the coastline can provide protection for the inland area during such highly destructive disasters. The research covering tsunami waves on costal areas has thus attracted more and more attention and will continue to in the future.

As tsunamis are difficult to forecast, it becomes necessary to investigate the characteristics of tsunamis in order to optimally design onshore infrastructure to resist this natural hazard. Extensive research studies have been conducted in the past to investigate the mechanism of generating tsunami waves; for example, the field survey by Nistor et al., (2005), Saatcioglu et al., (2005), Ghobarah et al., (2006), Palermo et al., (2013), and Mikami et al., (2019), the experimental work by Palermo et al., (2009), Nouri et al., (2010), and Al-Faesly et al., (2012a), the analysis by Yeh et al., (2014), Suppasri et al., (2019), the analytical research by Chanson (2005, 2006a), and Ginting et al., (2019). In the field survey, walls of the lower levels of many buildings near shore were found to be destroyed by the tsunami wave, which made the buildings hazardous to the lives of the people living within. In addition, the floods caused by

tsunamis threaten life due to the severe inundation by wave runup on the beach. Therefore, understanding the kinetic behaviors and hydrodynamic loadings is critical in tsunami research.

In the research by Chanson (2006a), it was revealed that the type of wave generated by dam-break was demonstrated to be similar to a tsunami broken wave approaching the shoreline. Thus, the dam-break model has been widely used to generate tsunami-like waves in laboratory experiments (Nouri et al., 2010; St-Germain et al., 2012; Wuthrich et al., 2019a) and numerical simulations (Kamra et al., 2018), to investigate the characteristics of tsunami waves. Earlier in the experiments studying dam break waves, Lauber et al., (1998) provided the vertical gate opening time criteria, which can be used to check if the ideal dam break flow could be generated; for example, in the dam break experiments by Lobovsky et al., (2014). These findings have provided a good understanding of tsunami waves and laid a solid foundation for conducting dam break experiments to investigate the characteristics of tsunamis.

In the past research, the kinetic behaviors of dam break flow, including the free surface profiles at different time instances, wave front location and velocity**,** were analytically and physically investigated to study the propagation of this tsunami-like waves. The analytical solution proposed by Chanson (2005, 2006a, 2009) described the properties of the tip region accurately and showed good performance in calculating and predicting the propagation of dam break flow over a horizontal bed. Using high-speed camera and image-processing techniques, the free surface profiles were captured experimentally to study the kinetic characteristics of dam-break flow in different stages, such as the experiments by Kleefsman et al., (2005). In addition, the free surface profile study provided detailed propagation data of dam break flow, and the complex interaction between the flow and structures, such as in the study by St-Germain et al.,

(2012). Another research concern of the kinetics of dam break flow is the wave elevation data at certain locations, which is measured by the wave probes and gauges in experiments, such as the studies by Kleefsman et al., (2005), Nouri et al., (2010), and St-Germain et al., (2012). Meanwhile, the wave runup and inundation situation could also be obtained by this measurement for the design of costal infrastructure.

The extreme hydrodynamic loading caused by tsunami waves is the main cause of failure of the coastal buildings and infrastructure. In dam-break experimental studies, pressure transducers were implemented to record the impact dynamic pressure on structures. The pressure transducers were embedded into the wall and kept flush with the structure's surface to measure the dynamic pressure in the short impacting and subsequent stages. In earlier experiments, larger-diameter pressure transducers were used, which caused unexpected oscillations of the pressure time-history and discrepancies when compared with results of numerical simulations; for example, in the study by Zhou et al., (1999). With material technology development, pressure transducers with smaller sensing areas, higher acquisition frequency and reliability were implemented in the dynamic pressure measurement of dam break experiments, and could reasonably accurate physical results could be obtained, such as in the experimental studies by Nouri et al., (2010) and Lobovsky et al., (2014). The dynamic pressure transducers could be installed at different heights and locations to obtain the spatial distribution of dynamic pressure to evaluate the hydrodynamic loading exerted on structures, and to provide a design water reference level for critical coastal infrastructure.

Furthermore, the extreme impact loading on structures can be monitored and measured directly by installing a force load cell (dynamometer) at the bottom of structures, usually for

slender structures, i.e., column to simulate the bridge pier. In the hydraulic forces on structures caused by tsunami-induced bores, Nouri et al., (2010) conducted a series of dam-break experiments to investigate the interaction between the impacting bores and freestanding vertical structures. The time-history of the global force acting on the cylindrical structure and the square structure were measured by dynamometer installed at the base of the structures. A force plate was also used in the experimental study to determine the horizontal impact force on buildings with openings by Wuthrich et al., (2018a). The captured forces on buildings with different openings revealed a linear reduction on the maximum horizontal force. In a subsequent research, (Wuthrich et al., 2018b), provided a more comprehensive study which also included the moment and impulse estimation on a building model, to further investigate the hydrodynamic impact on structures.

In addition to the experimental investigations, numerical simulations based on the VOF method in OpenFOAM (Sánchez-Cordero et al., 2017; Xie et al., 2019; Nguyen et al., 2020; Larocque et al., 2013; Evtushok et al., 2021) and SPH methods in DualSPHysics (Gomez-Gesteira et al., 2012a; Crespo et al., 2015a; Gu et al., 2017; English et al., 2021) have been widely applied in the characteristic research about tsunami-like wave, including the free surface profile, time-history of dynamic pressure and impact force acting on structures.

As described in the previous section, various experimental and numerical dam break studies were conducted on a horizontal bed, in tanks, flumes and channels to study the characteristics of the tsunami-like waves. The free surface profiles at different instances, the time-history of wave height at certain locations and the hydrodynamic loading were obtained for the analysis by high-speed camera and corresponding sensors, separately. However, few dam

break studies with slopes located downstream of the release mechanisms (gates) have been conducted. Most natural or man-made beaches in nature do have a slope, ranging from almost flat surfaces to maximum slopes of 20 degrees or more. It is also important to determine how the kinematics and hydrodynamic loading of dam break flow will perform on the onshore structures when considering the actual slope effects.

1.2 Objectives

The primary objective of this study is to investigate the bed slope effects on the kinematics and associated hydrodynamic loading of tsunami-like waves when propagating overland and impinging on coastal infrastructure. This study applied both experimental models and numerical simulation and aimed to investigate the influence of slope effects on the kinetics and hydrodynamic loading, as well as to provide some informed findings or guidance for engineers when designing the coastal infrastructure located on sloped beaches.

The first part of this thesis aims to evaluate the solid boundary treatment methods using the Smoothed Particle Hydrodynamics (SPH) method. Two commonly used boundary treatment methods, the ghost particle method and dynamic boundary condition method, are used in the numerical simulation of dam break by code, DualSPHysics and PySPH. Both of these methods can simulate the free surface well, but the ghost particle method causes particle leakage near the boundary, while the dynamic boundary method performs better when treating the boundary and in the wave breaking stage. In this study, the dynamic boundary condition method is suggested as the treatment method in SPH simulation due to its accuracy and stability. Furthermore, in a recent study, the modified dynamic boundary condition method (mDBC), presented by English et al., (2019) showed perfect performance with respect to eliminating the small gap between the

fluid and the boundary caused by the impulsive effect of the boundary method. Moreover, this improved boundary treatment method can improve the accuracy of the simulation domain by providing a more accurate approximation of the boundary layer. Thus, this newly developed boundary treatment method was applied in the SPH model for better performance in the following work in the last part.

The second part of the thesis is experimentally conducted to investigate the dynamics of dam break bores on a continuous vertical wall during the short period of impact and the subsequent instants. A series of dam break experiments were conducted in the Hydraulic Laboratory at the University of Ottawa, using a glass tank with a horizontal bed, along with the pressure transducer installed onto a vertical wall, ultra-sonic sensor and a high-speed video-camera. The statistical time-history of dynamic pressure from the miniaturized pressure transducer was compared and validated with another calibrated sensor to ensure accuracy. The normalized dynamic pressure measured from the lowest transducer along with the wave runup height were analyzed to present their correlation during the impact. For detailed insight into the pressure changes around the peak value, the pressure spatial distribution in several small-time windows was presented. The experimental results were also used to inform the preparation the next series of experiments with an inclined beach.

The main objective of the third part of the thesis is to investigate the slope effects on the kinetics of dam-break flows acting on the infrastructure. Three different slopes were built in front of the vertical wall to simulate an inclined beach with different slopes. The free surface water profiles at different instances were obtained from the videos recorded by the high-speed camera. The slope effects on the wave propagation were presented and discussed by comparing

the digitized free water surface profiles. The influence of the beech slope on the runup up along the wall was analysed by processing the time history of the bore height using the ultra-sonic sensor located above the wall's top edge. The wavefront location and its velocity were another kind of elements used to evaluate the slope effects on the kinetics of dam break flow. Numerical simulation using OpenFOAM and DualSPHysis were conducted to reproduce the experimental tests and to provide kinematic data by applying some novel simulation techniques, i.e., cross point capture. The wavefront location and velocity comparison between experiments and numerical simulation of horizontal case was presented in the Appendix, which demonstrated the ability and accuracy of numerical simulations.

The fourth part of this study focuses on investigating the characteristics of the hydrodynamic loading onto the wall when considering the slope effects, in terms of dynamic pressure and the impact force. The peak pressure data from the lowest transducer in the horizontal bed and inclined-beach cases are compared and discussed with the purpose of elucidating the effects of slope on the maximum impact pressure. The time-history of pressure data from the sensors located at the same level, for different tests, were also compared to shed light on the slope effects. The physical tests were reproduced using OpenFOAM and DualSPHysics models to compare the bore-induced dynamic pressure exerted onto the wall. Based on previous numerical simulations (Peng et al., 2021) and calculated results in this study, a simplified formula was proposed to estimate the impact force by integrating the dynamic pressure over the height of the wall. The impact force for the case of the horizontal bed was compared with that prescribed by the ASCE7-22 Chapter 6 tsunami design code (2022) as well

as with the formula of SMBTR (Okada et al., 2005a). The results of this last part of the study will hopefully provide guidance on the estimation of the impact force by tsunami inundation.

1.3 Novelty and contributions of the study

The major novel aspects and contributions of this study are listed below:

1) The key novelty of this research is the investigation of the effect of a sloped beach on the kinematics and hydrodynamic loading of a dam-break wave onto a wall. This type of investigation has not been performed in the past. The design of the three different slopes employed was adjustable in order to ensure the same location of the lowest transducer with respect to the bed in all cases. This design made it feasible to compare the maximum pressure from the lowest transducers and the pressure data from the transducer at the same levels for the different inclined bed cases.
2) For the purpose of comprehensive comparison, the experimental tests results were numerically reproduced using the two open-source models: OpenFOAM and DualSPHysics, based on Eulerian and Lagrangain approaches, respectively. The ability and accuracy of the numerical models to simulate dam-break experiments were presented and discussed. Good agreement between the results of the experimental tests and those of the numerical simulation demonstrated that features of the dam-break waves could be predicted reasonably well by the two numerical models.
3) In the OpenFOAM and DualSPysics simulations, several novel processing techniques were developed to obtain the wave front velocity. For example, a parallel-to-bed line

gauge was set in DualSPHysics to capture the wave front location, then used to calculate the average velocity.

4) A formula was proposed to estimate the horizontal impact force by integrating the dynamic pressure data with the assumption of zero pressure location. The comparison between the force measured results and that obtained using numerical simulation demonstrated the proposed formula can be used to estimate the impact force on walls due to by dam-break waves.

In addition, 3D printing technique was applied to create precise parts for pressure transducer assemble. And, advanced boundary treatment method was selected in DualSPHysics to help reduce instability and obtain better calculation results.

1.4 Scope and limitations of this study

This study was performed using both experimental tests and numerical simulation. Due to the conditions and the equipment used in experimental tests, as well as given the versions and performance of codes running on either a laptop or servers, there are some limitations for this study as follows:

1) The experiments were conducted in a 1.1-meter-long glass tank to investigate the slope effects on the hydrodynamics of dam-break flow propagating on the horizontal dry bed then over several sloped beds. Similar trends would probably be observed for longer flumes or when a wider range of impoundment depths.

2) The pressure transducer and ultra-sonic sensor applied together with the HBM data acquisition system in the experiment recorded the physical parameters at a frequency of 2,400 Hz. Newer, more performant pressure and ultra-sonic sensors, i.e., the

different sensing area, pressure measuring range and sensitivity, and the use of a higher acquisition frequency may lead to certain differences when measuring the parameters investigated.

3) Up-to-date and proper techniques were applied in the numerical simulation by OpenFOAM and DualSPHysics to obtain the most reasonable results. Good agreement was observed between the experiments and numerical simulation, but there were still some small discrepancies. The numbers of grids and particles used in the simulation using OpenFOAM and DualSPHysics, respectively, were reasonably significant but still limited by the available computing equipment. In the future, the existing numerical models could be improved by more advanced numerical schemes, simulation techniques, and the use of more powerful hardware.

1.5 Thesis structure and publications

The thesis structure is organized as follows:

1) Chapter 1: Introduction and Research Needs.
2) Chapter 2: Literature Review. This section presents a review of previous studies focusing on the dam-break waves in terms of analytical solutions, the kinematics and hydrodynamics through experimental tests, as well as numerical model.
3) Chapter 3 is in the form of a journal paper entitled “Evaluation of the Solid Boundary Treatment Methods in SPH”. This paper has been accepted and published by International Journal of Ocean and Coastal Engineering in 2018. A part of this work was also presented in the Water Symposium at Sherbrook University in 2018.

4) Chapter 4 is in the form of a journal paper entitled “Experimental Investigation on the Impact of Dam-break induced Surges on a Vertical Wall”. This paper has been accepted and published by the Journal Fluids, MDPI, in 2022.
5) Chapter 5 is in the form of a conference paper entitled “Experimental Investigation of Slope Effects on the Kinematic Behaviors of Dam-break Flow”. This paper has been accepted and published in the 39th IAHR World Congress, in 2022.
6) Chapter 6 is in the form of a journal paper entitled “Experimental and Numerical Investigation of Beach Slope Effects on the Hydrodynamic Loading of Tsunami-like Surges on a Vertical wall”. This paper has been accepted and published by the Journal of Marine Science and Engineering, MDPI, in 2022.
7) Chapter 7 presents the conclusions of this study as well as the recommendations for future studies.

Chapter 2 Literature Review

This part first presents a brief introduction of the tsunami wave, then summarizes the previous research about the analytical solution of ideal dam-break wave, and dam-break experiments on horizontal beds from the aspects of kinematics and dynamics. The simulations by Volume of Fluid method (VOF) and Smoothed Particle Hydrodynamics method (SPH) codes, OpenFOAM and DualSPHysics, to reproduce dam-break are reviewed to present the numerical research on dam-break wave. The techniques and methods used in the numerical simulation via OpenFOAM and DualSPHysics to obtain results for comparison with the experiments are also presented. The experimental and numerical research covering dam-break in terms of kinetics and dynamics are summarized and evaluated; thus, the research needs of this proposed study are identified.

2.1 Introduction of the tsunami wave

Tsunami waves are a series of extremely long waves caused by the sudden displacement of a large volume of water. This highly destructive natural hazard can happen in the ocean or coastal area due to the eruption of a volcano, submarine earthquake, certain types of weather, and in large lakes due to landslides. Most of the recorded tsunamis were located in the coastal area of the Pacific Ocean and Indian Ocean, and a few occurred in the Atlantic Ocean. The locations of recent and historical tsunami events are shown in Figure 2.1, based on the satellite map from the National Oceanic and Atmospheric Administration (NOAA, https://www.ngdc.noaa.gov/).

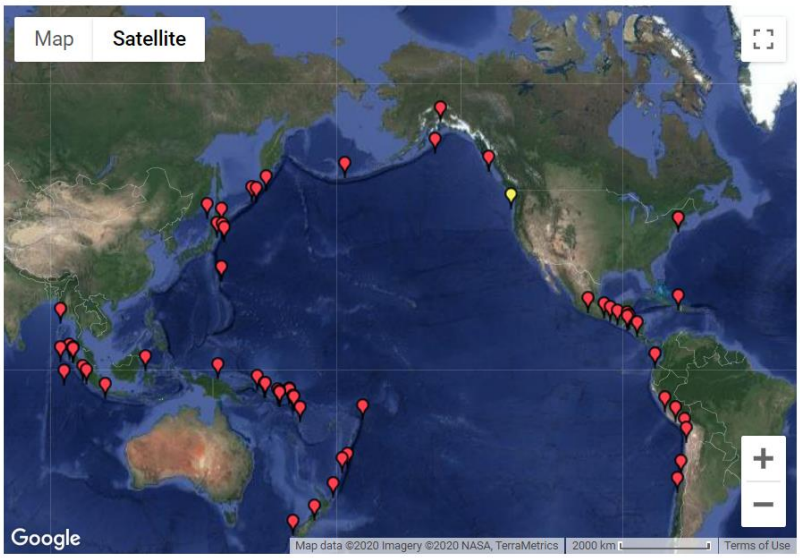

Figure 2.1 Satellite view of the locations of the recent and historical tsunami events, https://nctr.pmel.noaa.gov/database_devel.html, Map data, Copyright 2020 by Imagery, NASA, TerraMetrics.

Once the tsunami is triggered, it will propagate in all directions, except the limited propagation in the landslide case. The propagation velocity of tsunami waves in the deep ocean is related to the depth of the ocean, rather than the distance from the wave source, and can be formulated by the shallow water equation (Satake 1988) in Eq.(2.1). In the deep ocean, the propagation velocity of the tsunami wave could be 700-800 km/h, as fast as a jet plane. Different from the tidal waves, the tsunami waves will travel through the entire water volume, from the ocean bottom to the surface.

$$u = \sqrt{gD} \tag{2.1}$$

where, u is the propagation velocity, g is the gravitational acceleration, D is the depth of the ocean.

The wavelength of tsunami waves in the deep ocean could be hundreds of kilometers, and the wave height is within a small range, around 1 meter. However, when the tsunami wave approaches the shoreline, due to the slope and shallow water effects, the wave will slow down with decreased wave length, but the wave height will increase higher and higher to tens of meters, for example, the maximum tsunami wave height in the 2004 Indian Ocean Tsunami was 30m, and 40.5m in the 2011 Japan Tsunami. Great energy is contained in the high tsunami waves, thus the waves will bring extreme hydrodynamic loading on coastlines and destroy much of the infrastructure, buildings, lives and economies, as in the extensively damaged structures in the 2010 Chile Tsunami shown in Figure 2.2.

Figure 2.2 Experimental and numerical modelling of tsunami loading on structures by Nistor et al., (2011): Tsunami infrastructures damage due to the 2010 Chile earthquake and tsunami

In the past decades, researchers from different countries and regions have conducted various studies to investigate the mechanisms of tsunami waves; for example, the field survey by Nistor et al., (2005), Saatcioglu et al., (2005), Ghobarah et al., (2006), Palermo et al., (2013), and (Mikami et al., 2019), the experimental work by Palermo et al., (2009), Nouri et al., (2010), and Al-Faesly et al., (2012a), the analysis by Yeh et al., (2014), Suppasri et al., (2019), the analytical research by Chanson (2005, 2006a), Ginting et al., (2019). The onshore propagation of the

tsunami wave was found to be similar to the classical dam-break phenomenon. In the application studies about the analytical solution of dam-break wave, Chanson (2005) compared the water depth data from the videos recorded during the 2004 Indian Ocean Tsunami in Banda Aceh with the analytical solution, and obtained good agreement using the dimensionless time-variation plot. Thus, the analogy between the propagation of tsunami-induced bores and dam-break flow was demonstrated, as summarized by Nistor et al., (2011). In the past decades, the physical dam-break test has been widely used to generate the tsunami-like wave to investigate the characteristics and hydrodynamic loading on coastal infrastructure.

2.2 Analytical solution of dam break

The shallow water equations, also called 2-Dimensional Saint-Venant equations (Saint-Venant 1871), are derived from the Navier-Stokes equations, and can be applied to describe the flow in a rectangular channel, flume or tank:

$$\frac{\partial h}{\partial t} + u\frac{\partial h}{\partial x} + h\frac{\partial u}{\partial x} = 0 \tag{2.2}$$

$$\frac{\partial u}{\partial t} + u\frac{\partial u}{\partial x} + g\frac{\partial h}{\partial x} = 0 \tag{2.3}$$

where, h is the water depth, u is the depth-averaged velocity, t is the time from the instantaneous dam removal, x is the horizontal coordinate along the bed, g is gravitational acceleration.

By solving the shallow water equation, the earliest analytical solution of dam break could be seen in the theory presented by Ritter (1892), where the equation was applied to calculate the

movement of frictionless fluid in a dam break. The nondimensional solutions are expressed in equations as below:

$$Y = \left[\frac{1}{3}\left(2 - \frac{X}{T}\right)\right]^2 \tag{2.4}$$

$$V = \frac{2}{3}\left(1 + \frac{X}{T}\right) \tag{2.5}$$

$$Q = \frac{2}{27}\left(1 + \frac{X}{T}\right)\left(2 - \frac{X}{T}\right)^2 \tag{2.6}$$

where, the dimensionless parameters are $X = x / h_0$, $T = (g / h_0)^{1/2} t$, $Y = h / h_0$, $V = u / \left(g h_0\right)^{1/2}$, $Q = q / \left(g h_0^3\right)^{1/2}$, x is the coordinate along the horizontal bed, h_0 is the initial impoundment depth, t is time, g is gravitational acceleration, h and u are the wave height and time-averaged velocity at x, respectively, q is the discharge per unit width.

Ritter's solution showed a parabolic profile for the positive wave surface which could describe the wave propagation well, but is not valid to predict the flow properties in the wave tip region (Chanson 2005), as Ritter's solution showed concave upwards surface in the tip region for ideal fluid. However, the free surface profile in the tip region for the real fluid with resistance is convex upwards, as the difference shown in Figure 2.3. This has been demonstrated in the research by Chanson (2005, 2006a, 2009), Castro-Orgaz et al., (2017a), Deng et al., (2018) and Yang et al., (2018a).

By analysing the wave tip region of dam break flow with dominant flow resistance due to bed roughness and applying the method of characteristics, Chanson (2005, 2006a, 2009)

simplified and modified the solution for dam-break flow on horizontal beds; the sketch for the definition is shown in Figure 2.3.

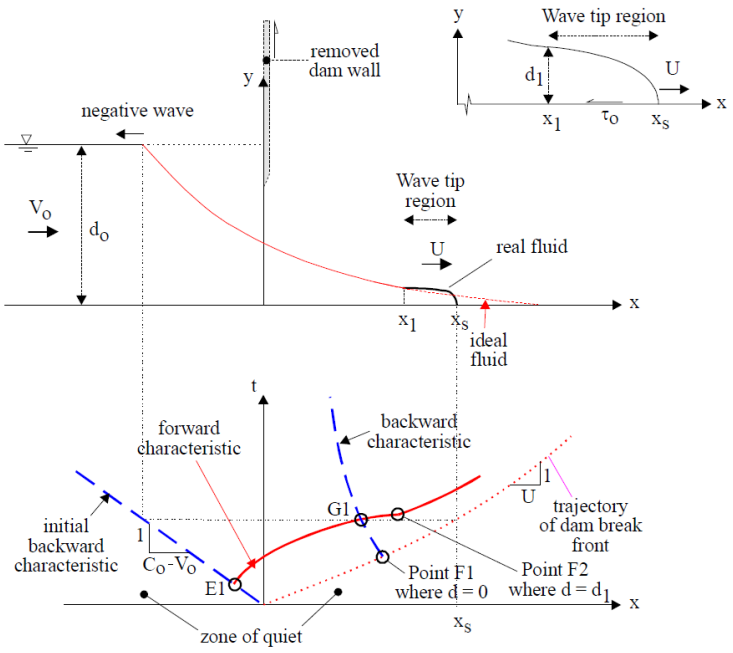

Figure 2.3 Definition sketch of dam break wave in horizontal channel in article '*Analytical solution of dam break wave with flow resistance. Application to tsunami surges*' by Chanson (2005):

In the modified solution, the relation between water depth and wave front velocity can be formulated in equations as below when $-1 \le \frac{x}{t \cdot \sqrt{g h_0}} \le \frac{x_1}{t \cdot \sqrt{g h_0}}$:

$$\frac{h}{h_0} = \frac{1}{9} \cdot \left(2 - \frac{x}{\sqrt{g \cdot h_0}} \right)^2 \tag{2.7}$$

$$\frac{u}{\sqrt{g h_0}} = \frac{2}{3} \cdot \left(1 + \frac{x}{t \cdot \sqrt{g h_0}} \right) \tag{2.8}$$

Then, in the tip region, where $\frac{x_1}{t\cdot\sqrt{gh_0}} \le \frac{x}{t\cdot\sqrt{gh_0}} \le \frac{x_s}{t\cdot\sqrt{gh_0}}$, the relation between the water depth and front celerity are shown in the equations below.

$$\frac{h}{h_0} = \sqrt{\frac{f}{4} * \frac{\mathrm{U}^2}{g * h_0} * \frac{x_s - x}{h_0}} \tag{2.9}$$

$$\mathrm{U}=u \tag{2.10}$$

The relation between other parameters is presented in the following equations:

$$\frac{8}{3}\cdot\frac{1}{f}\cdot\frac{\left(1-\frac{1}{2}\cdot\frac{\mathrm{U}}{\sqrt{gh_0}}\right)^3}{\frac{\mathrm{U}^2}{gh_0}} = t\cdot\sqrt{\frac{g}{h_0}} \tag{2.11}$$

$$\frac{x_1}{t\cdot\sqrt{gh_0}} = \frac{3}{2}\cdot\frac{\mathrm{U}}{\sqrt{gh_0}} - 1 \tag{2.12}$$

$$\frac{x_s}{h_0} = \left(\frac{3}{2}\cdot\frac{\mathrm{U}}{\sqrt{gh_0}} - 1\right)\cdot t\cdot\sqrt{\frac{g}{h_0}} + \frac{4}{f\cdot\frac{\mathrm{U}}{gh_0}}\cdot\left(1-\frac{1}{2}\cdot\frac{\mathrm{U}}{\sqrt{gh_0}}\right)^4 \tag{2.13}$$

In Eq. (2.7) - (2.13), h_0 and h are the initial reservoir depth and the water depth, the same as d_0 and d_1 in Figure 2.3, respectively, x is the coordinate along the horizontal bed, x_1 is the interface location between the main dam-break flow and the tip region, x_s is the coordinate of the wave front, h_0 is the initial impoundment depth, t is time, g is gravitational acceleration, f is the bottom friction coefficient of the wave tip region and is set as 0.015 here, $\mathrm{U} = u$ is the constant wave front celerity. Eq.(2.9) is obtained from the integration of diffusive wave equation and could describe the shape of the wave front profile between x_1 and x_s.

Chanson (2005) applied the analytical solution to compare with the wave depth data witnessed in 2004 Indonesia Tsunami (Western Aceh, Band Aceh). The time-varied water depth at three locations on a street were estimated from images, non-dimensionalized and compared with the analytical surge front. The comparison results presented good agreements between the real flow data and analytical wave front profile. Furthermore, strong effects of bed resistance could were highlighted in the real flow calculation. Thus, Chanson's solution for dam-break could be used to calculate and predict the free surface profile, location and velocity of the wave front. The analytical solution has shown good agreement when compared with the numerical simulation by Yang et al., (2018a), Deng et al., (2018). Hence, Chanson's solution may be used to validate the accuracy of dam-break results both in experiments and numerical simulation for the characteristics study.

2.3 Kinematic research of dam-break wave on horizontal bed

As mentioned in the previous section, dam-break is widely used to generate tsunami-like waves and study the characteristics. Different wave generation mechanisms have been proposed for the physical modeling of dam-break waves by the sudden removal of a volume of water, such as dam-break using swing gate (Nouri et al., 2010; St-Germain et al., 2014) vertical gate (Kamra et al., 2018; Lobovsky et al., 2014) and pneumatic basin (Rossetto et al., 2011; Nistor et al., 2017; Stolle et al., 2019a). In this study, the vertical gate removal method is used for dam-break wave generation. In the dam-break wave experiments, Lauber et al., (1998) proposed the gate opening time criteria, which can be used to check if the ideal dam-break flow can be generated. In dam-break experimental investigation, the kinematic behavior of the flow is one aspect of study, such as the free surface profile, surge height, wave front location and velocity.

2.3.1 Free surface profile study

In the earlier dam break study by Dressler (1952), the resistance effects of the bed roughness was investigated where a difference was found in the wave tip region when compared with Ritter's solution. Later in the experimental study, Dressler (1954) showed that the wave front shape is similar to the theoretical solution where the surface was convex upwards, different from Ritter's solution of ideal fluid. As mentioned in the previous section, now the analytical solution by Chanson (2005, 2006a, 2009) can present the tip region accurately, and showed good performance in calculating and predicting the propagation of dam-break flow as well. The free surface study of dam-break flow on a dry horizontal bed was first analysed by Martin et al., (1952), where the results showed that maximum wave velocity can be scaled by the square root of the reservoir height. Stansby et al., (1998) digitized the free surface images of dam-break flow on horizontal dry and wet beds, where they observed the special jets occurring in the initial stage in wet bed cases. Kleefsman et al., (2005) presented the free surface images in the initial stage and the images of waves impacting the structure from dam-break experiment videos. By image processing of the videos, Hu et al., (2010) obtained the free surface at different times from a series of laboratory experiments on the propagation of dam-break induced in dry bed conditions. By using a high-speed camera in dam-break experiments, Lobovsky et al., (2014) presented the free surface profiles of dam-break flow in different stages from the front, side and top view; the wave front shapes at different times were also captured. The image processing and analysis can also be applied to investigate the inundation on the structures. For example, in the study by St-Germain et al., (2012), the inundation images of dam-break flow on a column at different instances was recorded by camera. Wüthrich et al., (2016) used a high-speed camera to record

the moments of tsunami-like waves impacting and overtopping their cubic house model both in dry bed surges and wet bed bores. Other free surface profile studies of physical dam-break tests were also available in the study by Kamra et al., (2018)**.**

2.3.2 Surge height recording

The detailed surge height history at certain locations during propagation of the dam-break flow can be measured by wave probes and gauges. Thus, the surge height history data can be used for the evaluation of dam-break flow and the design of coastal structures. For example, in earlier dam-break experiment, Zhou et al., (1999) measured the wave height time history at certain down stream locations by using probes and obtained good agreement with the numerical results.

Kleefsman et al., (2005) measured the water height in the reservoir section and before the box located in the tank for dam-break experiment on a horizontal dry bed. In the comparison with numerical results, good global agreement was observed except for some differences when the water returned back. Nouri et al., (2010) obtained the bore heights upstream and downstream by setting two rows of wave gauges in the investigation of tsunami impact on a structure by generating dam break flow on a dry bed. In the study of tsunami-induced hydrodynamic forces on onshore structures, St-Germain et al., (2012) recorded the water surface elevation data with the wave gauges placed at several locations in the flume, where relatively good agreement was observed when compared with the numerical simulation.

2.3.3 Wave front study

Chanson (2005, 2006b) improved the analytical formula for dam-break wave by considering the resistance, which was caused by bed roughness, as indicated by f in Eq.(2.9),

(2.11) and (2.13) in section 2.1. The developed solution showed a convex shape in the wave tip region, which demonstrated better agreement with the previous experiments (Dressler 1952; Whitham 1955). In a numerical study on the characteristics of dam-break wave on a horizontal dry bed, Yang et al., (2018a) reproduced the dam-break experiments of Ozmen-Cagatay et al., (2010) in FLOW-3D, and also presented the analytical free surface by applying the formula of Chanson (2005, 2006b). A comparison of the results revealed that the analytical free surface profiles agreed reasonably well with experiments and numerically simulated results using Flow-3D, all with a convex shape in the wave tip region, which could also be observed in the experimental and numerical study by Nguyen-Thi et al., (2021). In the follow-up research which focused on the evolution of dam-break wave front profile, Yang et al., (2022) conducted both experiments and analytical solutions. In the case study of dam-break wave on horizontal dry bed, the wave front data obtained from the instantaneous snapshots exhibited a significantly shorter propagation distance when compared with the solution by Ritter (1892), which was caused by the bed resistance. The wave front profile agreed perfectly with the analytical solution by Chanson (2005, 2006b), which demonstrated that the bed roughness should be considered to obtain results close to the experiments.

Meanwhile, the wave front celerity was studied to describe the disturbance or change in wave phase. As indicated in the research(Deng et al., 2018; Yang et al., 2022; Wang et al., 2020), the averaged celerity in the wave tip region reached the maximum value at the instant the water column started falling, around $2\sqrt{gh_0}$, where h_0 is the initial impoundment depth. Next the celerity gradually decreased with time due to the bed resistance. The good agreements between experiments (Yang et al., 2022) and analytical solution Chanson (2005, 2006b) demonstrated

that the bed resistance should not be neglected, otherwise the celerity will be overestimated as in the solution by (Ritter 1892). Furthermore, the celerity decreased with the increase of depth ratio in the wet bed case, which meant that the wavefront propagated slower when the downstream water depth increased (Nguyen-Thi et al., 2021).

The location and velocity of the wave front can describe the propagation of dam-break wave more directly, estimate the wave arrival time and provide support regarding evacuation. In the hydrodynamic loading study of tsunami-like waves, Nouri et al., (2010) also calculated the wave-front velocity using the bore height arrival data, which was measured by six wave gauges. The processed non-dimensional coordinates, (X, T) showed good agreement with the numerically calculated wave-front velocity by Leal et al., (2006). In the study about characteristics of dam-break wave, Yang et al., (2018a) presented the time-history data of wave front velocity. From the plot, it can be found that the velocity increased quickly from the beginning to 2.7m/s, then reached a relatively steady stage, while gradually and gently decreasing due to the bed roughness, which dissipated the kinetic energy.

Numerous researchers have demonstrated that the free surface study of dam-break flow by analytical solution (Chanson 2005, 2006b; Wang et al., 2020; Leal et al., 2006; Castro-Orgaz et al., 2017b), experiment (Kamra et al., 2018; Lobovsky et al., 2014) and numerical simulation (St-Germain et al., 2012; Yang et al., 2018a; Yilmaz et al., 2021) can provide kinematic details about the time-varied wave propagation.

2.4 Hydrodynamic loading study of dam-break wave on horizontal bed

2.4.1 Dynamic pressure measurement

In another aspect, the hydrodynamic loadings during the impacting process of dam-break flow on infrastructures, for example, the impacting pressures and forces, are attractive topics for researchers as extreme hydrodynamic loading will cause severe damage to the onshore structures (Nistor et al., 2005; Palermo et al., 2013; Mikami et al., 2019).

By embedding pressure transducers in the vertical wall at the left part of the flume, Zhou et al., (1999) captured the impacting dynamic pressure by dam-break wave, which showed general agreement with the numerical results, but with high-frequency fluctuation before the initial impacting and sinusoidal-like discrepancies in the declined stage. Kleefsman et al., (2005) located one box in the dam-break model tank to simulate the green water flow on the deck of a ship, where several pressure sensors were installed at the front and top surface of the box to measure the dynamic pressure. Good agreement was observed between the experimental data and numerical simulation for the bottom front sensor. The experimental pressure value was larger than the numerical simulation for the upper right sensor. Except for some peak discrepancies in the lower left and right sensors, the experimental dynamic pressure agreed well with the numerical results. In the investigation of tsunami impact on the structure, Nouri et al., (2010) installed a series of pressure sensors on a cylindrical column and obtained the spatial pressure distribution, which clearly showed the pressure change along the height during the short impact. Lobovsky et al., (2014) conducted a series of dam-break experiments to investigate the pressure loads by using miniaturized pressure sensors in the 1:2 scale of the high-cited physical model (Lee et al., 2002) on a horizontal dry bed. The statistical pressure data of sensors 2, 3, 4

from 100 tests at 300mm impoundment depths showed good agreement when compared with the experimental results by Wemmenhove et al., (2010), Kleefsman et al., (2005) and Lee et al. (2002), separately. Recently, Xie et al., (2022) repeated the dam-break experiments of Lobovsky et al., (2014) to evaluate the stochastic characteristics of the impact dynamic pressure. The results revealed that the impact pressure was distributed over a wide range, thus a formula was proposed to describe the stochastic distribution in terms of the impact coefficient. Also, the surge front slope did not significantly influence the impact pressure at the bottom but affected the pressure slightly above the slope.

In the dynamic pressure study in dam-break experiments, the pressure transducers and sensors were installed in the wall or the structure, then under the impact brought by the dam-break flow, the dynamic pressure can be captured by the sensors for analysis. In this study, the impacting dynamic pressure on the fully blocked infrastructure wall is captured and measured by using calibrated pressure transducers.

2.4.2 Impact force study

The impact force on structures caused by tsunami-like wave can reveal the details of this extreme loading and provide design references for the coastal infrastructures. An empirical formula was proposed by Asakura et al., (2000) and Okada et al., (2005b) to provide the quick calculation of impact force on infrastructures by tsunami-like wave, which was presented in Japanese Structural Design Guideline (SMBTR). The maximum pressure was defined as 3 times the hydrostatic pressure, and the surge height on the infrastructure wall was also 3 times the maximum surge height. A linear pressure distribution was assumed on the wall; thus, the maximum impact force was 9 times that of the hydrostatic force, as shown in Eq.(2.14):

$$F_{x,\max} = \frac{1}{2}\rho g(3h_{\max})(3h_{\max}) = 9(\frac{1}{2}\rho g h_{\max}^2) \tag{2.14}$$

where, ρ is the water density, g is the gravitational acceleration, $h_{\max}$ is the maximum wave elevation from the ground while the wave freely developed (Okada et al., 2005b).

The calculation formula for impact force by tsunami-like wave was also available in ASCE - 7/22, based on the research work of Chock (2016), which was applied in the tsunami loads study by Stolle et al., (2018) and Wuthrich et al., (2019a). The maximum impact force was calculated by equation 6.10(4) in chapter 6, as shown below in Eq.(2.15) .

$$F = \frac{1}{2}\rho_s I_{tsu} Cd(h_e u^2) \tag{2.15}$$

where, ρ_s is the water density, I_{tsu} is the importance factor which is 1.25, C_d is the drag coefficient which is 2.0 when the wall is normal to flow, h_e is the inundated height taken as 2/3 of the maximum inundation depth, and u is the maximum velocity of tsunami flow.

In the experimental investigation, the impact forces were recorded by the load cell, force plate and dynamometer, which were installed at the surface and base of the structures, i.e., a column or a cubic model located in the downstream section. Several load cells and dynamometers were installed on the square column's surface and the cylindrical column's bottom to measure the local and global forces caused by the tsunami-like wave(Nouri et al., 2010). The local force study revealed that the force measured by the lower load cell was around 2 times higher than the forces exerted by the upper load cell. Unlike the upper load cell, an abrupt increase was observed in the time history of forces from the lower load cell. Meanwhile, in the global force investigation, it was observed that the initial impact force will not overshoot

the hydrodynamic force in the lower impoundment depth case. However, when the impoundment depth exceeded 1.0 m, a e value equal to the runup force was observed in the surge force, but it was greater than the hydrodynamic force.

A force plate was applied in the experimental research by (Wuthrich et al., 2018b) to investigate the hydrodynamic impact of tsunami-like wave against an impervious free-standing building. The results demonstrated that the horizontal surge and bore forces were proportional to the momentum flux; thus, a developed formula was proposed to estimate the maximum impact force. In a further study, Wuthrich et al., (2018a) installed the force plate at the bottom of pervious buildings to investigate the effects of openings. The impact forces on buildings with different porosity values were successfully recorded by the force plate, which revealed that a linear reduction of the maximum horizontal impact force was generated by the openings. The force plate was also successfully applied in the following studies investigating the effects of building overtopping (Wuthrich et al., 2019b) and bed roughness (Wuthrich et al., 2019a) on the induced load by tsunami-like waves.

2.5 Numerical simulation of dam break

Numerical simulation is widely applied in the Computational Fluid Dynamics (CFD) field to compensate for the disadvantages of experiments which require specific facilities and instruments, and cost considerable amounts of time, energy, and resources. In addition, with the development of theory and coding, the numerical simulation by codes and software could present good results in the hydrodynamic calculation and provide good comparison and validation for the experimental results. There are many CFD software programs for different applications, such as the commercial FLUENT and CFX, which require expensive licenses but do not allow

themselves to be modified much as they feature fixed built-in codes and modules. In this study, two highly technologically competitive and widely used open-source codes are applied for numerical simulation. One is the Eulerian OpenFOAM that contains various solvers, turbulence models and allows code customisation according to the problem; another one is the Lagrangian meshless DualSPHysics which includes GPU acceleration and allows for large deformations in hydrodynamics and shows perfect performance in free surface simulation.

OpenFOAM is an open-source C++ CFD code based on the Finite Volume Method, first developed by Henry Weller in 1989 and was rapidly developed in recent decades due to its advantages of a wide range of applications, friendly syntax, code customisation and so on. DualSPHysics (Crespo et al., 2015a) is based on the Smoothed Particle Hydrodynamics (SPH) model named SPHysics and developed to simulate the free surface flow and complex wave breaking where it may be difficult to apply Eulerian methods.

In this section, the numerical studies of dam break using OpenFOAM and DualSPHysics in the literature will be introduced and reviewed. The techniques used in this study are presented to show how the experiments are reproduced in OpenFOAM and DualSPHysics, and how the results are obtained for comparison.

2.5.1 Numerical simulation of dam-break in OpenFOAM

OpenFOAM as an open-source numerical tool with many solvers and modules available, is widely used in different fields of computational fluid dynamics, and is utilized in hydrodynamic research as well. For numerically reproducing dam-break events and investigating their characteristics, OpenFOAM has been applied often in the existing research work(Sánchez-

Cordero et al., 2017; Nguyen et al., 2020; Larocque et al., 2013; Nguyen-Thi et al., 2021; Zhainakov et al., 2013; Sarjamee et al., 2017; Ferro et al., 2022).

Zhainakov et al., (2013) reproduced the experiment of dam-break wave freely developed on dry horizontal bed (Martin et al., 1952) in OpenFOAM. An acceptable agreement between numerical and experimental results of wave height was obtained despite small discrepancies between the time-history curves. The experiment of dam-break wave impacting on a vertical wall (Zhou et al., 1999) was also simulated for verification. The free surface profiles at different time instances were successfully captured by the solver interFoam. The water column height at two locations obtained by OpenFOAM matched well with the experimental data before the wave breaking and returning. Relatively large differences were observed between the water height curves due to the wave breaking which will affect the measurement. Ferro et al., (2022) developed the interFoam solver by incorporating ghost fluid method for wide application of large CFD conditions. The free surface profiles of dam-break wave were captured by the improved solver with less wave wiggles. With the inherent calculation method modified, the velocity data at the wave probe was calculated and presented, which showed good and closer agreements with the test data(Gomez-Gesteira 2013), except the time difference at the initial impact.

To numerically examine the tsunami-like-induced hydrodynamic loading, Sarjamee et al., (2017) applied OpenFOAM v2.3.0 to reproduce the physical tests by Al-Faesly et al., (2012b). The calculated total base shear force on a square column showed general agreement when compared with the experimental data, but discrepancies were observed in the period, possibly because of the air entrainment and turbulence. On the pressure time-history curve, significant discrepancy was also observed at the initial impact, then general agreement was obtained

between the rest of numerical and experimental results. The dam-break experiments by (Lobovsky et al., 2014) were reproduced in OpenFOAM by Peng et al., (2021) to numerically investigate the impact on coastal structures by this extreme hydrodynamic event. The time-history of numerically calculated dynamic pressure matched well with the experimental results of transducers 1 and 2 at the lower levels. Except for the discrepancies for transducer 3 and underestimated pressure data for transducer 4, the numerical model could accurately predict the impact dynamic pressure.

Ferro et al., (2022) also calculated the impact force on the square column both by interFoam and the developed solver, marineFoam. The comparison demonstrated that both interFoam and marineFoam could calculate the impact dynamic pressure accurately, while closer results were obtained by the marineFoam when compared with the experimental force curve. Furthermore, better performance by the improved solver was observed on the peak force, where the value was overestimated by 5.85%, however, a higher underestimated 15.1% was observed in the results by interFoam.

2.5.2 Simulation techniques used in OpenFOAM

The techniques used in OpenFOAM to capture the free surface profile, wave height and dynamic pressure at certain locations will be introduced in this section.

Free surface profile capture

For the dam break simulation in OpenFOAM, the two-phase interFoam solver is applied, which is based on the volume of fluid (VOF) method. The method was first proposed by Noh et al., (1976) and then applied to solve the dynamics of free boundaries by (Hirt et al., 1981). In the application for free surface tracking and identification in OpenFOAM, a phase fraction, α_{water}, is

adopted to describe the volume in each computational cell, as shown in Eq.(2.16). Other physical properties, such as pressure and velocity, are calculated as weighted averages based on this fraction.

$$\alpha_{water}\begin{cases}1 & \text{for the water phase}\\ 0 & \text{for the air phase}\end{cases} \tag{2.16}$$

After the simulation was done, all the results could be visualized in the third-party software, ParaView. In the results category of *alpha.water*, the value could be set as 0.5, which presents the interphase between the water and air. Thus, the free surface of the dam break flow could be captured, and the data can be exported from the datasheet for plots, as shown in Fig 2. 1.

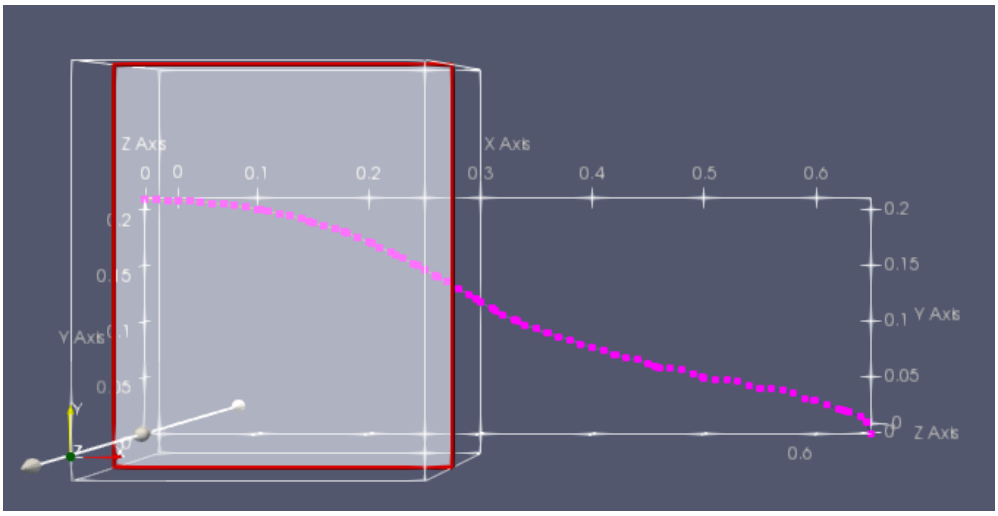

Figure 2.4 Free surface profile at $\alpha_{water} = 0.5$ in OpenFOAM, presented in ParaView 5.6.0

Wave height at certain location

Many tools and function objects are available in OpenFOAM to provide functions for the extraction of calculated data. To obtain the wave height at a certain location, or the height of the free surface at a certain point, the command ***interfaceHeight*** is added in the ***controlDict*** of the simulation case, located in the ***system*** folder in the hierarchical structure of OpenFOAM. In the

processing of ***interfaceHeight*** function object, the vertical distance of the interface above both the location and the lowest boundary will be written to an output file, marked as hL and hB. Next, the values of the wave height at certain points can be extracted from the output file. The detailed commands added and modified are shown below:

```
functions
{
    interfaceHeight1
    {
        type            interfaceHeight;
        libs            ("libfieldFunctionObjects.so");
        alpha           alpha.water;
        locations
                        (
                            (x1 y1 z1)
                            (x2 y2 z2)
                            …
                        )
    }
}
```

Dynamic pressure

Similar to the function objects, there are also a set of post-processing tools for sampling the calculated data. For capturing the dynamic pressure at specific positions on the right wall, the post-processing command ***probe*** is applied, which belongs to the functions of probing data. The command ***probe*** can identify and capture the specified physical parameters in the nearest cells to the locations defined in the probe dictionary. In this study, the coordinates of the certain points are listed in the probe file, then this file will be called by *'#includeFunc probes'* in the ***controlDict*** to be executed, as shown in the command below.

```
functions
```

```
{
    #includeFunc        probes;
}
```

Impact force

To calculate the resultant horizontal impact force on the right wall in OpenFOAM, the library of force was called in the ***controlDict***. The corresponding batch was defined as right wall, as the code showing below.

```
#includeFunc forces;

 forces1

{    type                forces;

     functionObjectLibs     ("libforces.so");

     patches  ( rightwall);

      rhoName rhoInf;

      rhoInf 1000;

}
```

Wave front location and velocity

The visualization of the results from OpenFOAM simulation in ParaView can show the general velocity distribution contour for estimation; however, the exact wave front velocity at different times can not be obtained directly. In this study, a novel post-processing idea is proposed by setting a single straight line 5mm above the bed when the *alpha.water* value is chosen as 0.5. When the wave front crosses this line, the coordinates of the cross point will be recorded. Next, the displacement and average velocity of the wave front can be calculated by extracting the location data by codes.

2.5.3 Numerical simulation of dam break in DualSPHysics

Due to the advantages of Lagrangian, meshfree and particle characteristics, DualSPHysics is widely implemented in hydrodynamic research, especially in the case of wave breaking, large free surface deformation and fluid-structure interaction. DualSPHysics is further developed based on the previous SPH code SPHysics and released by Universidade de Vigo, University of Manchester and other academic institutes.

Before the release of DualSPHysics, some research about dam-break simulation was conducted in the previous version of SPHysics. Gomez-Gesteira et al., (2012a) presented the detailed description of the theory, scheme, and formulation in SPHysics, and showed the performance of this open-source code by using dam-break and wave evolution cases. In the study of efficiency and test cases (Gomez-Gesteira et al., 2012b), SPHysics was demonstrated as an efficient numerical tool in the free surface and fluid-structure interaction study where reasonable agreement could be obtained by this code when compared with the existing experimental work. In the application study of SPHysics, St-Germain et al., (2012) numerically reproduced the experiments of Nouri et al., (2010) covering tsunami-like bores impacting a column, and work by Kleefsman et al., (2005) investigating dam break flow impacting a cubic obstacle using SPHysics, where the Riemann solver was applied to avoid the fluctuations in pressure. In both studies, the free surface elevation time history data and profiles showed that the numerical simulation by SPHysics could obtain well-matched data with little discrepancy, and very close free surface in the fluid-structure interaction process when compared with the experiments. One exception was the wave ‘runup’ height in the case of Nouri et al., (2010), where the numerical result was lower than the experiment at the initial impact on the column; in this case, the

numerical simulation could not reproduce the significant splash of water. In the dynamic pressure field observation, the numerical pressure was in good agreement with the experimental data except that the numerical dynamic pressure of the bottom sensor was much higher than the experiment at the initial impact, around 180%, possibly because of the entrapped air in the bore front during the impact. In the SPH calculation efficiency research by Crespo et al., (2011), the experiment of Kleefsman et al., (2005) was conducted and a similar result was obtained in that the numerical pressure peak of the bottom sensor was 40% over-predicted compared to the experiments at initial impact. By implementing SWE-SPHysics, Gu et al., (2017) studied the particle dam-break flow by testing two benchmarks; one was the EU CADAM project (Morris 2000), and another one was the experiment by Kleefsman et al., (2005). In the free surface elevation time-history data of the two case studies, generally satisfactory agreement was observed between the experimental and numerical results; meanwhile, there were also some minor discrepancies between the data curves due to the vertical acceleration generated during the complex flow-structure interactions.

With developments in the structure and language of coding, more advanced functions, features and GPU calculation acceleration technology, DualSPHysics showed good performance and accuracy in the free surface flow simulation and efficient calculation by implementing the GPU acceleration. Except for the method, scheme and formulations applied in DualSPHysics, Crespo et al., (2015a) also introduced the CPU & GPU implementations, program documentation, and analysed the efficiency and performance by dam-break test on CPU for series calculation and different GPUs for parallel calculation, where the latter can be 24-times faster. The free surface profiles at different instances during the complex interaction between the

flow and the column structure were successfully simulated and presented clearly. In the GPUs calculation of DualSPHysics study, Mokos et al., (2015) applied dam-break flow to an obstacle as the test case, where they found that wave height and dynamic pressure from higher resolution simulation could show better agreement with the experimental results, but bigger differences were observed for P3 and P4 sensor probes on the higher position of the obstacle's front surface. The height and pressure curves were generally matched in trend; however, there were discrepancies in the height curves and many tiny oscillations on the pressure curves.

2.5.4 Simulation techniques used in DualSPHysics

The physical properties in SPH method, such as density, mass and velocity, are calculated via integrating function and particle approximation by using the information from the particles in the support domain, namely the neighbouring particles. The techniques used in DualSPHysics to capture the free surface profile, wave height and dynamic pressure at a certain location are based on this core concept and will be introduced in this section.

Wave height at a certain location

To obtain the wave height at a given location in DualSPHysics, the mass of the particle along the Z direction in the simulation domain is calculated using the mass value of the neighbouring particles, as shown in Eq.(2.17).

$$m_i = \sum_j m_j W_{ij} \tag{2.17}$$

where m_i is mass of the particle located in the Z direction, m_j is the mass of the neighbouring particle, W_{ij} is the kernel function.

Then compare m_i with reference mass $m_{reference}$. If the ratio is 0, it means the particle is located in the air; if the ratio equals 1, it means the particle is submerged; and the particle is located in the interface of the air and water when the ratio equals 0.5, then the wave height at this given location is the z coordinate of the particle, as shown in Figure 2.5.

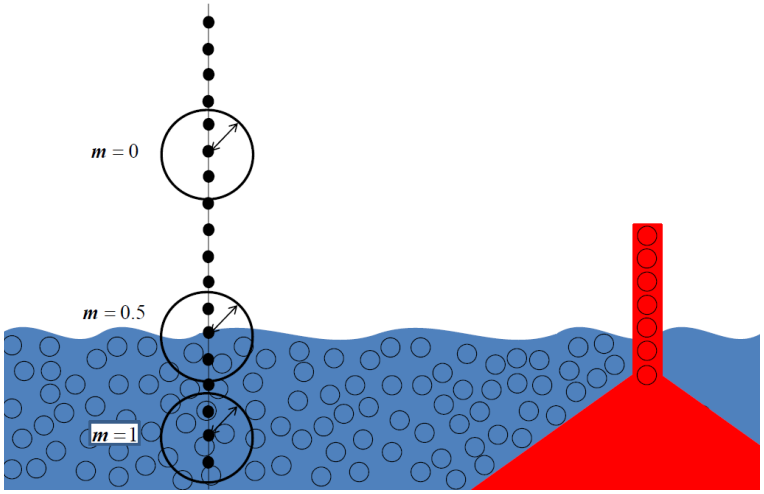

Figure 2.5 DualSPHysics postprocessing calculation v5.0 (2020): how to numerically compute free surface elevation.

Free surface profile

Based on the techniques of detecting wave height at a given location, the free surface profile at different instances can also be obtained. In order to obtain the free surface of dam break flow, a ***slice*** is defined in the central part of the model. All the wave heights of the particles on this slice will be calculated and recorded, then the free surface profile data can be extracted from the points.

Dynamic pressure

Similar to the mass calculation, the dynamic pressure for a specified location is also calculated based on the pressure of the neighbouring particles, as shown in Eq.(2.18).

$$P_i = \frac{\sum_j P_j W_{ij}}{\sum_j W_{ij}} \tag{2.18}$$

where P_i is the pressure needed in the specified location, P_j is the pressure of the neighbouring particles and W_{ij} is the kernel function.

Impact force

In order to calculate the impact force on the boundary wall, the acceleration of the boundary particles will be numerically computed by solving the particle interactions with fluid neibouring particles, as shown in Eq.(2.19).

$$\frac{du_i}{dt} = -\sum_{j=1}^{N} m_j \left(\frac{p_i}{\rho_i^2} + \frac{p_j}{\rho_j^2} + \Pi_{ij}\right)\nabla_i W_{ij} + g \tag{2.19}$$

where, ρ_i, u_i, p_i are the density, velocity and pressure of particle i, respectively, m_j, ρ_j are the mass and density of neighboring particle j, ∇ is the gradient operator, W_{ij} is the kernel function, and Π_{ij} represents the artificial viscosity term.

Furthermore, the resultant impact force on right wall can be obtained by doing summation of forces of the boundary particles, as shown in Eq.(2.20)

$$F = \sum_{i=1}^{N} m_i \frac{du_i}{dt} \tag{2.20}$$

where, N is the number of particles in the computational area, m_i, v_i are the mass and velocity of boundary particle i, respectively.

Wave front velocity

In this study, a straight line 5mm above and parallel to the bed is defined in the geometry and numerical model to detect the wave front. The location of the wave front at different instances will be recorded once the flow approaches the line. Then, the average velocity of the wave front can be calculated and obtained.

2.6 Summary and discussion of the existing work

Based on the literature review, dam-break flow has been adopted as a common strategy used to investigate tsunami-like waves. Dam break flow research with respect to free surface, wave height and dynamic pressure was widely conducted to study the characteristics of tsunami-like waves, which can be seen in the existing literature. However, most of the dam-break research was performed on horizontal beds, while a few studies were found that investigated the slope effects, but in real life situations, there will be an inclined beach along the coastline that will definitely influence the propagation and hydrodynamic loading of any tsunami-like wave affecting the infrastructure. OpenFOAM has proven to be a powerful numerical tool in computational fluid research; however, it has drawbacks when dealing with the problem where dramatic free surface breaking and complex fluid-structure interaction occur. DualSPHysics has shown great potential in the free surface simulation, but a well-known problem is that this code can not predict the impacting dynamic pressure, precisely due to the theoretical limitation.

Limited open literature to date has reported the slope effects on the propagation and hydrodynamics of tsunami-like waves. The research needs of this study investigate the slope effects on the kinetics and dynamics of the tsunami-like wave, including the wave free surface profiles, wave elevation, and hydrodynamic loading on infrastructures experimentally, and numerically by using the dam-break case. The newly released DualSPHysics will be applied in

reproducing the experiment numerically, and its performance, accuracy and stability in the pressure field calculation will also be investigated and verified. OpenFOAM will be implemented to provide comparison data due to its accuracy and stability, and the performance of free surface simulation will be investigated by comparing the experimental and numerical results from DualSPHysics. This study is expected to provide results and evidence into how the slope effects will affect the propagation and dynamics of dam-break flow, thus will present useful references for the design of coastal infrastructure against tsunami-like waves when considering the inclined beach.

Chapter 3 Evaluation of the Solid Boundary Treatment Methods in SPH

Abstract

The smoothed particle hydrodynamics (SPH) method has been proved as a powerful algorithm for fluid mechanics, especially in the simulation of free surface flows with high speeds or drastic impacts. The solid boundary treatment method is important for the accuracy and stability of the numerical results, as the support domain of fluid particles is truncated near the vicinity of the boundary. This paper presents two commonly used methods for simulating a solid boundary in SPH simulations. Emphasis is placed on the description of the methods, definition of the boundary particles' parameters, and discussion of their advantages and shortcomings. The classical dam break simulation is conducted using self-developed code and open-source models such as DualSPHysics and PySPH in order to investigate the effects of the boundary methods. The results show that methods based on dynamic boundary particles can simulate the free water surface well with a good agreement with experimental results. The conclusions can also be used in research for boundary implementation methods for practical ocean and coastal engineering problems with free surface flows.

Keywords: SPH; Solid Boundary Method; Free Surface; Numerical Validation

3.1 Introduction

The smoothed particle hydrodynamics (SPH) method was first proposed to solve astrophysical problems (Gingold et al., 1977; Lucy 1977), and due to its particular advantages of being Lagrangian, meshfree, and adaptive, this algorithm was successfully extended to fluid

mechanics (Monaghan 1994). In SPH, the support domain of fluid particles is truncated by the wall boundary near its vicinity, and loss of support domain will cause small errors in the properties of fluid particles near the boundary. Furthermore, these small errors will accumulate and expand to the whole fluid field. Thus, the solid boundary has been a research concern since the beginning as it plays a critical role in the accuracy and stability. For better application effects, relevant developments should be adopted to handle this shortcoming of boundary treatment methods.

The solid boundary condition is one of the most commonly seen boundary types in fluid mechanics and practical engineering problems, such as in various kinds of tanks, experimental flumes, natural rivers, artificial canals, and so on. To simulate this solid boundary, Monaghan (1994) set a row of fictitious particles in order to provide a repulsive force to prevent fluid particles penetrating the boundary. It is simple but with poor conservation properties as the movement of the particles near the boundary could not be simulated accurately. In numerical tests, some fluid particles will become attached to the left side wall boundary due to the introduced force. This phenomenon will cause inaccurate kernel sum estimates for the density and velocity calculations (Randles et al., 1996). This method was then refined by Monaghan et al., (1999), with development of an interpolation process, minimizing the inter-spacing effect of the boundary particles on the repulsive force of the wall. For better conservation and accuracy, Libersky et al., (1993) introduced so-called ghost particles, and later Randles et al., (1996) made the method more general by assigning the same boundary value of a field variable to the ghost particles. The water surface became smoother as the values of specified ghost particles were interpolated smoothly, and thus the values of the interior particles will be also calculated more

accurately. But the simulation time will increase sharply as the mirrored particles will be newly generated in every time step along with the position change of corresponding fluid particles. Also, due to the relatively weak fence effect, fluid particles will penetrate the boundary when contacting with the solid boundary. To establish the strong boundary and guarantee accuracy, in research by Liu et al., (2001), two types of virtual particle were applied to simulate the wall boundary: Type 1 is similar to the repulsive particles by Monaghan (1994), and Type 2 is similar to the ghost particles by Randles et al., (1996). In their studies, the numerical results showed that this treatment of boundary is very stable and effective. However, small displacements of the fluid particles in the proximity of the boundary corresponds to variations of the intensity of the repulsive force. Thus, oscillation will be introduced into the pressure field of the fluid(Ferrari et al., 2009). To treat the system simplified, in dynamic boundary particles (DBPs) method, position of the boundary particles remain fixed but they share the same equation of state and continuity with the fluid particles. This method is first introduced in the studies of Dalrymple et al., (2001) and further used in interactions between waves and coastal structures (Gomez-Gesteira et al., 2005), and now has been widely used in SPH simulations recently (Gomez-Gesteira et al., 2010). Crespo et al., (2007a) explained this method in detail and analyzed the repulsion mechanism. From the computational point of view, the DBPs is more simplified as no special consideration is necessary for the boundary walls. If the DBPs could not have sufficient particles in the support domain, inaccurate pressure oscillation could be introduced in to the results (Shao et al., 2012). Therefore, a good understanding of boundary treatment methods is essential for SPH research, and in this paper, two of the above-mentioned boundary treatment methods will be described and examined due to their good performance in hydrodynamics.

In this paper, first the basic SPH theory is presented, including the general aspects of the scheme, density, pressure, and XSPH correction, and the governing equations and solution methods are explained. Then the commonly used treatment methods are described in terms of boundary particle position, density, mass, pressure calculation, and velocity definition. Finally, the dam break case is conducted in self-developed code, DualSPHysics, and PySPH for evaluating the selected methods, and the results are compared and discussed. Some concluding remarks complete the study.

3.2 SPH methodology

3.2.1 SPH scheme

The smoothed particle hydrodynamics method is implemented by particle approximation and, is done in two steps: continuous interpolation and discrete approximation. The first one can be written as:

$$f(r_a) = \int_{\Omega} f(r) w(|r_a - r|, h) dr + O(h^2) \tag{3.1}$$

Where, Ω is the fluid domain, and h is the smoothing length which defines the kernel's support size and is equal to the initial particle distance.

The discrete interpolation applies the weighted contributions of the surrounding neighbour particles to make an approximation of the interpolation equation:

$$f(r_a) \approx \sum_{j=1}^{N} v_j f_j(|r_a - r_j|, h) \tag{3.2}$$

In the SPH method, the fluid flow is typically assumed to be governed by Navier-Stocks (N-S) equations, which can be described in Lagrangian formulations:

$$\frac{d\rho}{dt} + \rho\nabla \cdot v = 0 \tag{3.3}$$

$$\frac{dv}{dt} = -\frac{1}{\rho}\nabla p + \frac{\mu}{\rho}\nabla^2 v + g \tag{3.4}$$

where, ρ, v, p, μ represent the density, velocity, pressure, and dynamic viscosity of the fluid respectively, and g is gravity.

In SPH, the fluid field is represented as a collection of particles. By applying SPH kernel approximation and the derivative in Eq.(3.1) and Eq.(3.2), after discretization, Eq.(3.3) and Eq.(3.4) can be reformulated as:

$$\frac{d\rho_i}{dt} = \sum_{j=1}^{N} m_j v_{ij} \cdot \nabla_i W_{ij} \tag{3.5}$$

$$\frac{dv_i}{dt} = -\sum_{j=1}^{N} m_j \left(\frac{p_i}{\rho_i^{\,2}} + \frac{p_j}{\rho_j^{\,2}} + \Pi_{ij}\right)\nabla_i W_{ij} + g \tag{3.6}$$

where, ρ_i, v_i, p_i are the density, velocity and pressure respectively of particle i, m_j, ρ_j are the mass and density of neighbouring particle j, $v_{ij} = v_i - v_j$, W_{ij} is the kernel function where cubic-spline kernel function(Monaghan et al., 1985) is used in this paper, Π_{ij} represents the artificial viscosity term, and N is the total number of neighbouring particles of particle i. In this paper, because of the negligible viscous effect, the physical viscosity effect is ignored, and the Monaghan-type artificial viscosity is added to the momentum equation to help guarantee numerical convergence by eliminating physical oscillation.

Then, the density and velocity can be explicitly calculated by time integration methods, such as the leap-frog, predictor-corrector, and Runge-Kutta methods. In this paper, the predictor-

corrector method(Monaghan 1989) is applied due to its second order accuracy and good stability (Shafieefar et al., 2008). The time step is calculated on a CFL condition. Furthermore, the particles' positions can also be obtained by time integration.

3.2.2 Density and pressure

Attention should be paid to the density term as it plays a fundamental role in the discretized N-S equation. The density term will be further used to calculate the particle' pressure, which is crucial to the velocity calculation in the N-S momentum equation. The pressure is calculated by the equation of state, which can be presented in a weakly compressible form (Monaghan 1994):

$$p = \frac{\rho_0 c^2}{\gamma}[(\frac{\rho}{\rho_0})^{\gamma} - 1] \tag{3.7}$$

where, p is the pressure of the fluid particle, ρ_0 is the reference density and is set as $1000\,kg/m^3$, ρ is the density of the fluid particle, c is the sound speed which is usually chosen as 10 times the maximum velocity of fluid flow, and index γ is used as 7. In some studies, the term $\rho_0 c^2/\gamma$ is referred to as the reference pressure, and can be written as p_0 (Morris et al., 1997) or B (Colagrossi et al., 2003).

As discussed before, pressure is a significant element in SPH but is very sensitive to the density. If there is a small error in the density term, there will be a large deviation in the pressure and velocity fields, and then the whole fluid domain will be influenced by large errors. The treated boundary particles will also introduce numerical errors in density and pressure. The density should be corrected every certain number of time step, so a necessary modification could be adopted to guarantee convergence of the calculations. In this paper, the density of fluid

particles is reinitialized every 50 time steps according to the average density correction formula (Shafieefar et al., 2008):

$$\rho_i = \frac{\sum_j m_j W_{ij}}{\sum_j m_j W_{ij} / \rho_j} \tag{3.8}$$

The average density or density normalisation prevents density deviation and keeps the density of the particles close to the reference density. This operation can help ensure that the surface remains smooth and physically acceptable (Colagrossi et al., 2003).

3.2.3 XSPH correction

The basic SPH theory can handle fluid flow problems well, however oscillation can also appear in the velocity field due to the boundary treatment methods. To prevent particle inter-penetration and to regularize the weakly compressible treatment of fluids, (Monaghan 1989); Monaghan (1992) introduced the XSPH velocity correction Δu_i, which takes the velocities of neighbouring particles into account through a mean velocity evaluated by the particle in support domain. The velocity correction can be expressed as:

$$\frac{dx_i}{dt} = v_i - \varepsilon \sum_j \frac{m_j}{\rho_j} v_{ij} W_{ij} \tag{3.9}$$

where, v_i is the velocity of particle i, m_j, ρ_j represent the mass and density respectively of neighbouring particle j, $v_{ij} = v_i - v_j$, W_{ij} is the kernel function, and ε is a constant in the range of $0 \le \varepsilon \le 1$. Liu et al., (2016) pointed out that the XSPH technique includes the contribution from neighbouring particles, and thus makes a particle move at a velocity close to the average velocity of the neighbouring particles. They suggested that ε be equal to 0.3 in

simulating incompressible flows in most circumstances. Another recommendation was that $\varepsilon = 0.1$ in two-dimensional problems, and $\varepsilon = 0.01$ in three-dimensional problems. The corrected velocity is used in density and position calculation equations which does not appear in the momentum equation(Colagrossi et al., 2003).

3.3 Methods for solid boundary treatment

Generally, methods for treating a solid boundary in SPH theory can be categorized into 5 groups: the repulsive force boundary particle method, virtual particle method, combined repulsive and virtual particle method, dynamic boundary particles method, and boundary integral method. In this paper, the ghost particle method and the dynamic boundary particles method are explained due to their better performance in free water surface simulations.

3.3.1 Ghost particles

Using ghost particles, sometimes referred to as virtual particles or mirror particle(Libersky et al., 1993), is a feasible approach to represent boundaries by generating mirror images of the fluid particles out of the boundaries. When the fluid particles approach the vicinity of the boundary, generally close to the initial particle distance, their mirror particles will be set symmetrically about the boundary. Besides the opposite normal velocity, other properties of the virtual particles, such as density, mass, pressure and tangential velocity, remain the same as the symmetric fluid particles (Colagrossi et al., 2003) described in Eq.(3.10).

$$\begin{cases} \rho_{iG} = \rho_i, \quad x_{iG} = 2x_w - x_i, \quad p_{iG} = p_i \\ v_{niG} = -v_{ni}, \quad v_{tiG} = -v_{ti} \end{cases} \tag{3.10}$$

where, i represents particle, G is donated to the virtual/ghost particle, ρ is the density, x means the particles' positions, x_w is the position of the rigid boundary, and v_n, v_t are the normal velocity and tangential velocity respectively. This topologic relationship is depicted in Figure 3.1. By providing the contrast normal velocity, these mirror particles can prevent fluid particles penetrating the boundary.

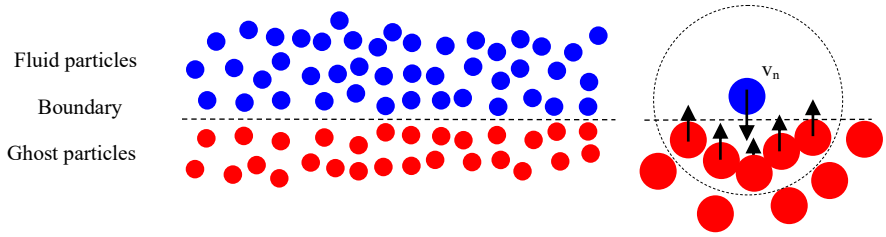

Figure 3.1 Sketch of the fluid particles and their virtual particles

For better simulation results, the time step can be decreased when the fluid particles reach the boundary, or the virtual particles can be placed more intensively to provide a stronger 'fence' effect. It should be noted that in order to provide stronger boundary effect, the critical distance for setting ghost particles between the fluid particles and the boundary should not be expanded too much. The fluid particles will be influenced once the critical distance is enlarged, which will result in physical oscillation in the density term. Furthermore, the pressure, acceleration, and velocity terms will be calculated inaccurately.

3.3.2 Dynamic boundary condition

First presented by Dalrymple et al., (2001) and further used in the interaction between waves and coastal structures (Gomez-Gesteira et al., 2005), dynamic boundary particles are applied to simulate a solid boundary in SPH. This method is now the default boundary treatment method in DualSPHysics (Crespo et al., 2015b) and PySPH (Ramachadran 2016; Ramachandran

et al., 2013). In the study by Crespo et al., (2007a) , this method is explained in detail and analyzed in the repulsion mechanism.

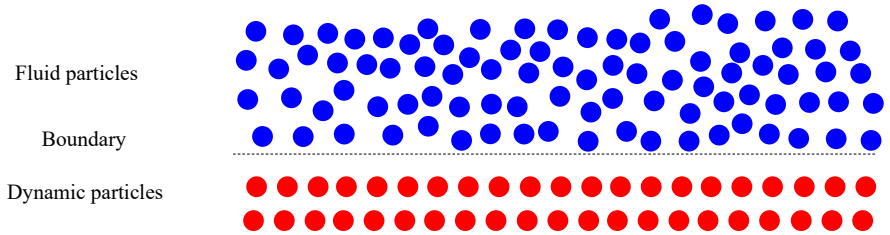

Figure 3.2 Sketch for dynamic particles

Different from other boundary particles mentioned before, these dynamic particles satisfy the same equations of continuity and state as fluid particles, but their velocities are zero and their positions remain unchanged or are externally imposed. Due to this special property, these particles can be calculated simply inside the same loop as fluid particles, which can save considerable computational time. In this method, the same fluid particle equations will be satisfied by the boundary particles. Thus, these dynamic particles will obey the continuity equation (3.5) and the equation of state (3.7), and they are included in the momentum equation of the fluid particles (Gomez-Gesteira et al., 2010). However, Eq.(3.6) and (3.9) are not used for boundary particles.

The density of boundary particles will increase when a fluid particle approaches another one within a distance less than twice that of the smoothing length (h), resulting in pressure increases. In turn, this results in a repulsive force being exerted on the fluid particles due to the pressure term in the momentum equation (Crespo et al., 2015b) which will prevent the fluid particles penetrating the boundary. Dalrymple et al., (2001) pointed out that two rows of stationary particles at all boundaries were sufficient to contain the fluid. This default particle

position setting has been demonstrated to be feasible in other research works (Gomez-Gesteira et al., 2005; Crespo et al., 2007b; Go´mez-Gesteira et al., 2004). The topology relationship is shown in Figure 3.2.

3.4 Numerical experiments

A dam break flow is a classical free surface flow which includes water splash due to the interaction of the water body and solid walls, large deformation of free water surface, and a water tongue and bore area due to the rotation of the runup flow. Smoothed particle hydrodynamics can simulate these complex phenomena well with results similar to the experiments (Colagrossi et al., 2003). In this paper, the 2-dimensional dam break case is conducted to evaluate the ghost particle method in a self-developed Fortran code and the dynamic boundary method in C++ code DualSPHysics and Python code PySPH.

3.4.1 Numerical modelling setting

In the simulated 2D dam break model, a 2m-high, 1m-wide water column is located along the left boundary of a solid tank which has a square shape with 4m length and 4m width. The gravity acceleration is 9.81 m/s^2. At the beginning, the distance between particles is 0.01m, hence there are 20000 particles in the simulation domain. For the conservation of numerical calculation, the time step is set as 0.0001s under the CFL condition. The initial static water column with pressure contour in DualSPHysics is shown in Figure 3.3:

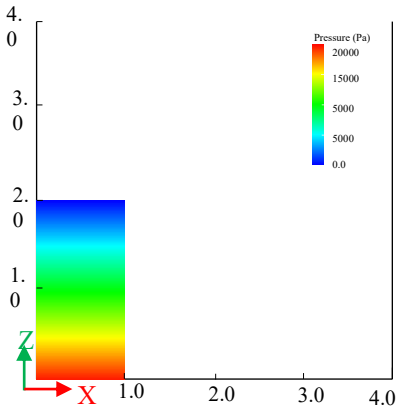

Figure 3.3 Pressure Contour of Dam Break Model

3.5 Results and discussion

Two different boundary methods are evaluated in three programs as mentioned before. All the simulations were done on an Intel (R) Core (TM) i7-7820HQ @2.90GHz, CPU 32GB memory, HD 630, 64-bit laptop. In this section, the particles' behavior near the boundary area will be discussed to evaluate the methods' effect, and the numerical results will be compared to show the performance of these two methods in simulating free surface water flow.

3.5.1 Behaviour of fluid particles near the boundary

In order to check the effects and explore the differences between the boundary treatment methods, two boundary areas are chosen: the bottom side and the right side of the solid tank. By recording some instants, the behaviors of the fluid particles can be obtained.

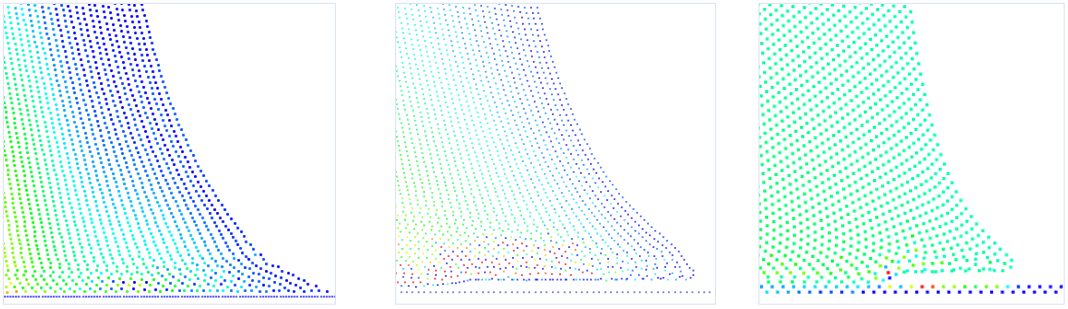

(a) (b) (c)

Figure 3.4 Fluid particles near the bottom at t=0.2s: (a)Ghost particle method; (b) dynamic boundary method in DualSPHysics; (c) dynamic boundary method in PySPH

When the water column starts collapsing, the fluid particles located at the right bottom will form the front wave. At t=0.2s, some fluid particles move over the dry bed, as shown in Figure 3.4. The fluid particles in the ghost method are closer to the bottom boundary, however the fluid particles in the dynamic boundary method is like repulsed by the boundary. Thus, a small gap appears between the fluid particles and the bottom boundary, as shown in Figure 3.4 (b) and (c).

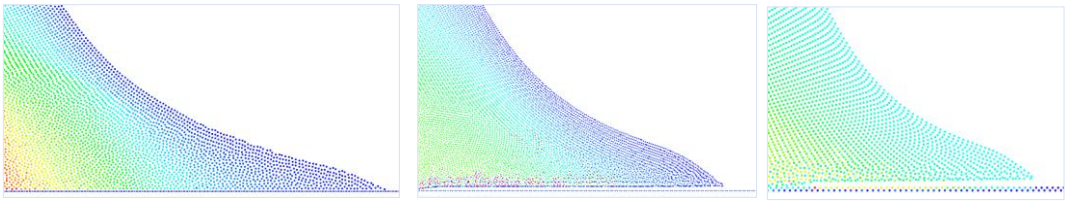

(a) (b) (c)

Figure 3.5 Fluid particles near the bottom at t=0.4s: (a)Ghost particle method; (b) dynamic boundary method in DualSPHysics; (c) dynamic boundary method in PySPH

Then, the front wave continues to move on the dry boundary bed with a lower similar trend: the fluid particles in ghost method move closer to the boundary, while the fluid particles still keep a small gap with the bottom, as shown in Figure 3.5 (a), (b) and (c).

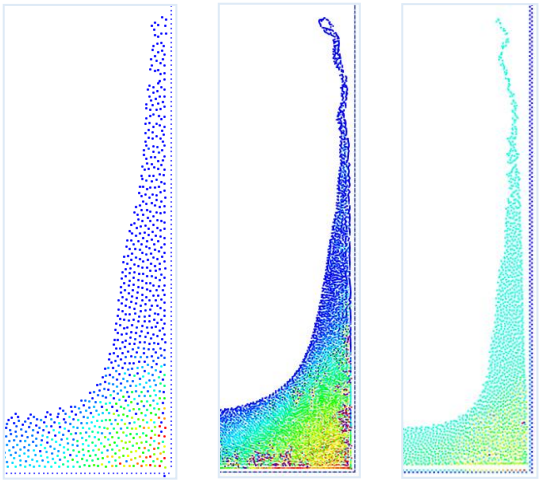

Figure 3.6 Fluid particles near the right boundary at t=0.9s: (a)Ghost particle method; (b) dynamic boundary method in DualSPHysics; (c) dynamic boundary method in PySPH

After the front wave impacts the right solid wall, the fluid flow goes up along the boundary. Later, a vertical jet appears against the vertical wall. Similar to the results in previous time step, there is a small gap between the jet and the boundary wall in the dynamic boundary method, as shown in Figure 3.6 (b) and (c). In the ghost particle method, the jet attaches well to the boundary wall, as shown in Figure 3.6 (a).

The above small gaps between the fluid flow and the boundary in Figure 3.6 are caused by the spurious effect of the DBPs method, because when enforcing the original DBPs on the solid boundary, the presence of the DBPs inside the computational domain can cause anomalously high density gradients near the DBPs (Gomez-Gesteira et al., 2005). As a result, spurious high-frequency pressure oscillation and large unphysical boundary layers will appear in the flow near the solid wall due to the large pressure gradients between the fluid and boundary particles (Ren et al., 2015). In our numerical simulation, this effect is reflected in the small repulsive gap between the fluid particles and the wall boundary. This spurious effect can be

minimized by the improved DBPs method which applied the buffered density correction (Gomez-Gesteira et al., 2005). In the floating object research, Ren et al., (2015) applied this improved skill, successfully eliminated the discontinuous pressure and clearly demonstrated the difference between the original DBPs and the improved DBPs. This improved technique could be adopted in our future research for better performance.

3.5.2 Free water surface profile comparison

Under gravity, the water column begins collapsing, flows along the tank bottom, crashes against the right solid wall, goes up along the vertical boundary, and then flows down and rotates back. At different instants, i.e., t=0.4s, 0.6s, 1.0s and 1.6s, the pressure magnitude contours are dispersed as shown in Figure 3.7.

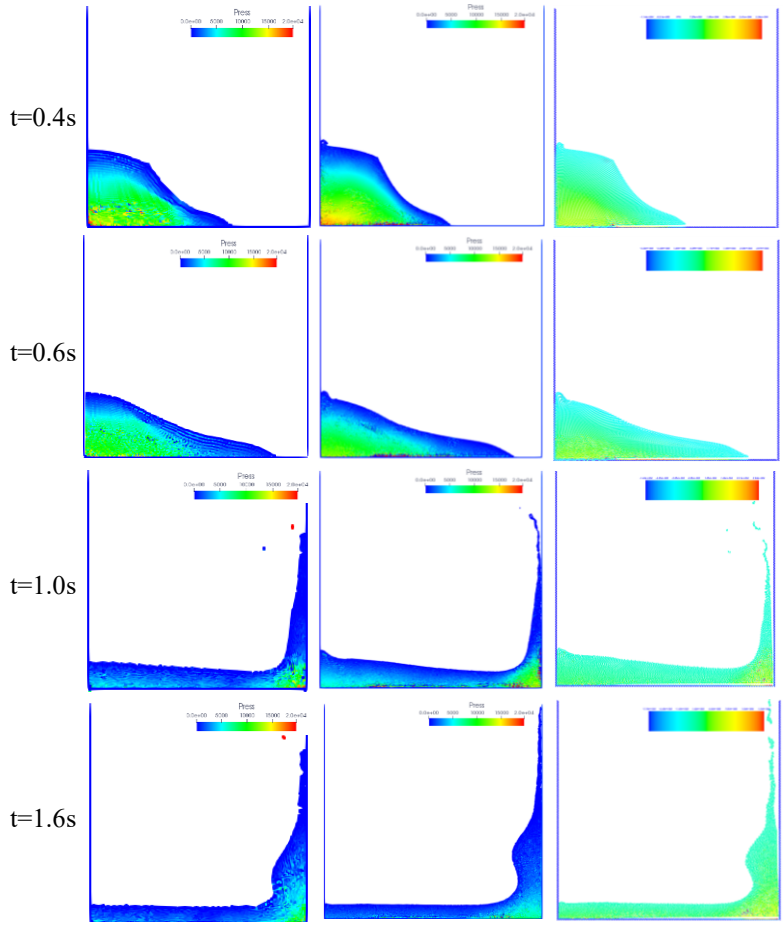

Figure 3.7 Dam break at t=0.4s, 0.6s, 1.0s and 1.6s: (a)ghost particle method in self-developed code; (b) dynamic boundary method in DualSPHysics; (c) dynamic boundary method in PySPH

At t=0.4s, the top water column surface near the left boundary wall in the ghost particle method is smoother than that in the dynamic method. This smooth top water profile agrees well with the phenomenon in the experiments by Lobovsky et al., (2014). A small sharp unsmoothed part is observed both in Figure 3.7 (b) and (c), which shows that there are unphysical oscillation or fluctuation at the beginning in the dynamic method.

Then, the water column continues collapsing, and at t=0.6s, the advance downstream almost covers the tank bottom, and the previous sharp part becomes gentle in DualSPHysics and PySPH. However, tension instability is observed near the gentle corner in PySPH. The water surface in the ghost particle method is still in good shape profile-wise, but in the flowing process, some particles go through the boundary wall in the ghost particle method due to the relatively weak effect of the boundary. This decreases the water particle number and results in some problems.

Due to the support of upcoming water, the water flow will go higher after crashing against the right boundary, as shown in Figure 3.7. At time equals to 1.0s, the disadvantage of the ghost particle method appears, as the water flow could not go to the same height with the results in the dynamic method. This is due to the loss of fluid particles, which leads to errors in the whole simulation field. The water heights in the dynamic method in DualSPHysics and PyPSH are almost the same, except that the right water edge is not very close to the boundary wall in PySPH.

Before the up-flowing water rotates back, at t=1.6s, a water bump appears on the right wall. The water bump in the ghost particle method does not rise that high compared with the ones in the dynamic method. The shape and height in the latter two models are similar and in good agreement with the experiments (Lobovsky et al., 2014).

3.5.3 Plunging breaker and bore propagation

When the water bump falls off and goes back, it will rotate back and form a plunging breaker, which can be easily observed in the experiment. However, this phenomenon did not

appear in ghost particle method as the lower water bump part. In this part, the final stage of the dam break in DualSPHysics and PySPH are discussed, as shown in Figure 3.8.

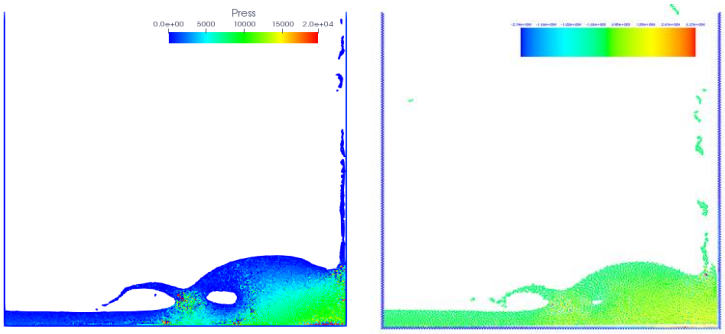

(a) (b)

Figure 3.8 Dam break with dynamic boundary method at t=2.15s: (a) in DualSPHysic; (b) in PySPH.

When the plunging breaker forms, a bore area gradually appears upon the bottom water layer as the back rotated water tongue. The resulting profiles in these two programs are very similar except that the bore area in PySPH is smaller than in DualSPHysics. The simulated 2D dam break side view in DualSPHysics is clearer, as shown in the compared local bore areas in Figure 3.9:

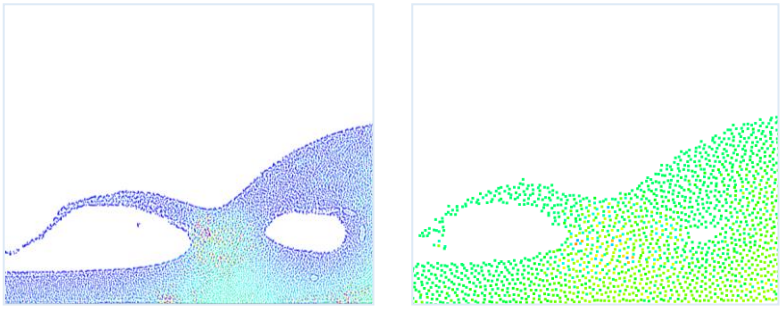

(a) (b)

Figure 3.9 Local bore area at t=2.15s: (a) in DualSPHysics; (b) in PySPH.

At the final stage of dam break in Figure 3.7, and the bore area in Figure 3.8 and Figure 3.9, similar results were obtained, but some small differences were observed between the results in DualSPHysics and PySPH even with the same DBPs method, and parameter setting used in both codes. One possible reason is that same theory is applied in the different codes, bur their program frames, processing methods, and post-processing tools have differences.

3.6 Conclusion

(1) In this paper, two different methods have been presented to simulate a solid boundary in SPH. Both the ghost particle method and the dynamic method can simulate well the free water movement which is demonstrated in the numerical dam break experiment.

(2) Near the boundary area, the ghost particle method can handle the fluid flow well with a closer result to the experiment. However, due to the weak boundary effect and loss of fluid particles, errors will be introduced into the calculations. For the final stage of the dam break, the result is not good when compared to the DBPs method.

(3) Due to the density gradients, there is small gap showing up near the boundary in DBPs method. But, the DBPs method can model the free surface water flow well, especially in the plunging area. The whole simulation shows that the DBPs method is more accurate and stable. And the corresponding buffered density method can be adopted to minimize the spurious effect in our further study.

(4) As an artificial boundary establishing method, some small errors are introduced into the simulation, which results in unsmooth water surface near the left boundary when the water column starts collapsing. This needs to be studied further.

(5) So far, the qualitative comparisons were presented to show the performance of and difference of the boundary treatment method. The quantitative time history data comparison will be conducted in our next research for the purpose of more direct comparison.

Chapter 4 Experimental Investigation on the Impact of Dam-break Induced Surges on a Vertical Wall

Abstract

This paper presents the results of an experimental investigation on the impact of dam-break-induced surges on a vertical wall. The instantaneous surge height and dynamic pressure on a vertical wall were measured for surges with different reservoir depths of H = 200 mm, 250 mm, and 300 mm. The time-histories of horizontal pressure on the wall were measured using the miniaturized pressure transducers, and the surge heights were recorded with an ultrasonic sensor. The relationships between dynamic pressure and surge height on the vertical wall and during the impact were obtained from recorded raw data. The experimental results highlighted detailed processes on the variation of impact pressure during the surge propagation, impact on the wall, runup, falling, and breakup of the turbulent flow. The time-histories of surge height and dynamic pressure were analyzed, and the results were compared with the hydrostatic pressure on the wall to study wave breaking mechanism of tsunami waves on the wall. Dynamic pressures at the impact instant were found to be approximately three times the corresponding static pressure in the bed, in good agreement with previous research Moreover, the maximum surge runup heights on the wall were between 2.1 and 2.3 times the corresponding initial reservoir depths. The vertical distributions of impact pressure were divided into two hydrodynamic regimes. Based on the impact duration, the first regime occurred less than 0.1 s after the impact with highly non-linear pressure distributions, and the second regime showed a semi-hydrostatic pressure

distribution from 0.5 s to 0.7 s. The results presented in this study are suitable for the design of coastal infrastructures and can be used to validate numerical models.

Keywords: dam-break wave; tsunami-like wave; turbulent surge; dynamic pressure; free surface; surge height; runup

4.1 Introduction

Tsunami waves have caused severe damage to coastal infrastructures and buildings and claimed many lives due to extreme hydrodynamic loading. Such events became more frequent and caused significant infrastructure damages in the past few decades, such as the 2010 Chile Tsunami, 2011 Japan Tsunami, 2013 Solomon Islands Tsunami, 2015 Central Chile Tsunami, and the 2018 Indonesia Tsunami. Numerous field surveys and laboratory experiments have been carried out to study the hydrodynamics of tsunami-like waves and to determine the tsunami's loading on coastal structures (Palermo et al., 2013; Mikami et al., 2019; Al-Faesly et al., 2012a; Nistor et al., 2011; Shibayama et al., 2015). Nistor et al., (2009) provided a detailed evaluation of extreme hydrodynamic loading due to the propagation and impact of tsunami waves and recommended a revision of the design of coastal structures. They emphasized the necessity and importance of such extreme hydrodynamic loadings, such as pressure and force, for the adequate design and reconstruction of coastal infrastructures and buildings in tsunami-prone areas.

To reproduce tsunami waves and associated inundation in laboratory conditions, different wave generation mechanisms have been proposed in the literature, such as the sudden removal of a volume of water through vertical pipes (Wuthrich et al., 2019b, 2018c), a dam-break mechanism using swing gates (Nouri et al., 2010; St-Germain et al., 2014; Stolle et al., 2019b),

vertical wall gates (Lobovsky et al., 2014; Häfen et al.,), and a pneumatic basin (Rossetto et al., 2011; Nistor et al., 2017; Stolle et al., 2019a) for the physical modeling of tsunami-like waves. A wave generated by the dam-break mechanism showed similar wavefront shape and propagation characteristics as tsunami-induced inundation propagating overland (Chanson 2006a). Therefore, the dam-break model has been widely used to generate tsunami-like inundation in laboratory experiments and numerical simulations (Nouri et al., 2010; St-Germain et al., 2012; Wuthrich et al., 2019a; Kamra et al., 2018).

Based on shallow water theory, Ritter (1892) initially derived the analytical solution for wave propagation on a frictionless horizontal bed generated by a dam-break mechanism. The bed friction effect was later included in the theoretical study of wave propagation, and the results were verified with experimental observations (Dressler 1952, 1954). This model was demonstrated to be a good approximation and provided a reasonable prediction. By applying the method of characteristics in the treatment of bed resistance, Chanson (2009) simplified and modified the solution for dam-break flow on the horizontal bed, where the free surface in the tip region showed the same convex upwards shape as the physical test. According to the presence of an initial water layer on the bed, dam-break waves are categorized into wet and dry bed conditions. The time-history of the water surface profile of dam-break induced waves on a dry bed showed that the maximum wave velocity was scaled by the square root of the reservoir height (Martin et al., 1952).

Using high-speed imaging, Hu et al., (2010) captured free surface profiles of turbulent surges at wave impacting, runup, breaking, and air entrainment stages. Digitized surface profiles showed a horizontal jet in dry bed and a special mushroom-like jet in wet bed conditions at the

initial stage of propagation. Based on the previous research of unbroken (Hernández-Fontes et al., 2018; Hernández-Fontes et al., 2019) and partially broken waves (Hernández-Fontes et al., 2020a) generated by wet dam-break on a fixed structure, Hernández-Fontes et al., (2020b) developed and investigated this interaction via fully developed broken incident flow. In the experiment, a high-speed camera, water elevation, and force sensors were applied to record the overtopping behaviors, patterns, and loads. Regarding the overtopping pattern, a moving hydraulic jump was observed in the broken wave case, different from the stable undular bore in the unbroken case. As a result, the most violent interaction was observed in the fully developed broken wave case. At $h_0/h_1 = 0.4$, a large plunging wave was observed, which hit the deck end and formed large air cavities, which was similar to the behaviors of dam-break flow on the dry bed. Similar dam-break free surface studies were also reported to investigate the flow kinematics, for flow against an obstacle (Soares-Frazao et al., 2007), over a mobile bed (Soares-Frazao et al., 2012), and against a vertical wall (Kamra et al., 2018; Lobovsky et al., 2014).

Force and pressure transducers were used in the past to measure the time histories of force and dynamic pressure by dam-break induced waves impacting structural walls. The pressure transducers were embedded in the front and top surfaces of a small cubic block to measure the dynamic pressure around the block (Kleefsman et al., 2005). Good agreement was reported between the experimental and numerical results for the bottom front transducers. To investigate the complex interaction processes between hydraulic bores and structural models, Nouri et al., (2010) measured the vertical pressure distributions on the wall of a cylindrical structure by installing a series of pressure transducers onto the frontal face of the cylinder, facing the incoming flow. The results presented the spatial pressure distribution during the short impact,

including the peak value and pressure variation range. A comparison between the experiments and the Smoothed Particle Hydrodynamics (SPH) simulation indicated that the numerical predictions of the initial impact pressure were much higher than the experimental results for just the bottom transducer (i.e., h = 0.05 m). At higher locations (i.e., h = 0.15 m, 0.2 m, and 0.3 m), the numerical predictions agreed well with the experimental results. Furthermore, negative dynamic pressures due to the suction effect were observed in both the experimental and numerical data at h = 0.3 m (St-Germain et al., 2012).

A partially blocked cube was used as a model of a residential house to study the effects of hydrodynamic loadings induced by tsunami-like waves (Wüthrich et al., 2016). The impact loading of dam-break waves under both dry and wet bed conditions and for different impoundment depths was studied. The image analysis during wave propagation and the subsequent impact on the wall indicated that the bores propagating in wet bed conditions generated higher splashes than those propagating over the dry bed. The difference was due to the steeper wavefront generated in wet bed conditions. Similarly, the overtopping mechanism doubled in height onto the structural model (Wuthrich et al., 2019b). The results showed that the overtopping of the shorter structure induced higher downstream water depths, leading to lower horizontal forces due to smaller water depth differences between the upstream and downstream (Wuthrich et al., 2019b).

The structures investigated for the interaction between tsunami-like waves and their walls were either fully blocked or partially blocked by the flume. During the impact of the dam-break wave with a vertical wall, the bore runs to a high level along the vertical wall and then moves backwards. Experimental and numerical studies in the literature showed that fully blocked walls

absorb more impact loading than partially blocked walls (Karunya et al., 2012). Recent experimental studies showed that impact loading on coastal structures could be reduced in structures with large openings. Wuthrich et al., (2018a) designed several cubical structures with different openings (i.e., permeability) to investigate the effects of building openings on hydrodynamic loadings. Due to the presence of openings, lower upstream inundation depths were observed in comparison with the corresponding inundation depths occurring on impervious buildings. Moreover, a linear correlation was found between horizontal hydrodynamic forces and the area of the openings.

A series of dam-break experiments on a dry bed with reservoir depths of H = 300 mm and 600 mm were carried out to investigate the impact of dam-break waves on a vertical wall (Lobovsky et al., 2014; Lee et al., 2002). The miniaturized pressure transducers were installed on the left wall of the tank to capture the time-history of dynamic pressure (Lobovsky et al., 2014). Experiments were repeated 100 times, and the average pressure variations were analyzed. The quantitative and statistical analysis of pressure loads indicated a linear correlation between the impact pressure points at the bottom of the tank. The statistical pressure data above the bottom of the tank showed good agreements with other studies (Kocaman et al., 2012; Liu et al., 2018). Some differences were also observed between experimental results and numerical simulations. The numerical results underestimated the experimental data, and the sudden pressure drop was the result of excessive diffusion and small bubble formation (Kamra et al., 2018).

Extensive experimental and numerical studies were performed in the past to investigate the interaction of tsunami-like waves and walls by analyzing free surface profiles, surge height, and dynamic pressure variations with time. However, less attention has been paid to

investigating the relationship between dynamic pressure and surge height at the location of the vertical wall during the wave impact, runup, falling, and breaking events. Image analysis and dynamic pressure data indicated that during the wave impact, dynamic pressure is relatively steady while the surge height rapidly changes. Therefore, it is hypothesized that during this short but rapidly changing process, the relationship between the dynamic pressure and surge height is not clear. The main objective of this study is to investigate the correlation between dynamic pressure and surge height in time and investigate the vertical distribution of the dynamic pressure on the wall. In this regard, the time-variant behavior of dam-break induced wave propagation on a dry bed and its impact on a vertical wall was studied in detail. Both the time-histories of surge heights and pressure distributions on a vertical wall were measured, and the correlations between water level variations and dynamic pressures were analyzed. The measurements were conducted using an array of pressure transducers installed in the centerline of the vertical wall and on both left and right sides of the centerline to capture the three-dimensional motion of the surge.

The present paper is organized as follows: This section contains an introduction presenting a literature review and the research needs and motivation for the study. A detailed description of the experimental setup and instrumentation is provided in Section 2. Section 3 deals with the repeatability and calibration tests. The time-histories of free surface water levels and dynamic pressures are presented in Section 4. Comparison with previous research and limitation of this study are discussed in Section 5. Finally, the outcomes of the present experimental study are concluded in Section 6.

4.2 Experimental setup

A series of laboratory experiments were conducted in the Water Resource Engineering Laboratory of the University of Ottawa, Canada, to investigate the vertical distribution of water level and dynamic pressure on a vertical wall. Experiments were conducted in a rectangular, horizontal, glass-walled tank of 1.2 m long, 0.44 m wide, and 0.5 m high, as shown in Figure 4.1.

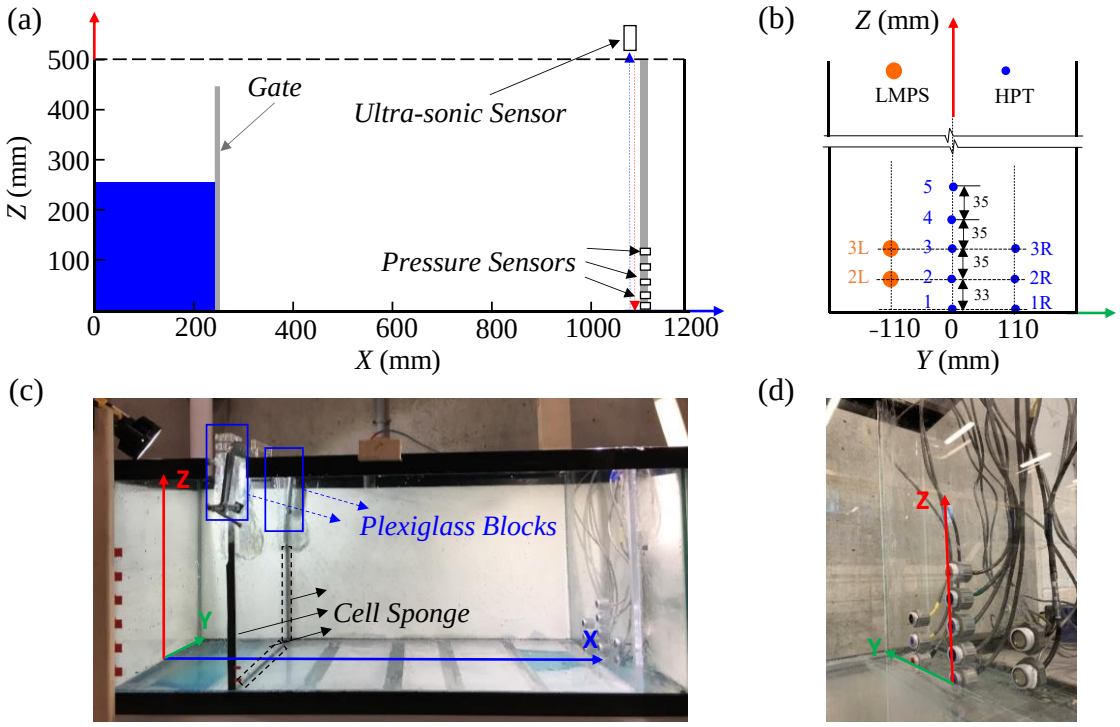

Figure 4.1 Experimental setup and the adopted coordinates system: (a) schematic of the experimental setup in initial condition; (b) side view schematic of the experimental tank and the positioning of TE connectivity LM−series Pressure Transducers (LMPT) and Honeywell Pressure Transducers (HPT); (c) side-view image of the experimental tank; d) pressure transducers' location.

4.2.1 Tank apparatus

A rail-guided vertical gate system was added 250 mm downstream of the tank wall; through rapid opening, this gate was used to generate dam-break waves (Figure 4.1 a, c). Dam-break waves were generated by the rapid lifting of the vertical gate using three different impoundment water depths of H = 200 mm, 250 mm, and 300 mm. To prevent leakage, a thin layer of black cell sponge was fitted around the gate frame along the tank walls to reduce the gap between the gate and the flume walls. In order to generate a perfect dam-break wave, the maximum gate opening time, t, was measured and compared with the threshold normalized opening time of $t(g/H)^{1/2} < 2^{1/2}$ as suggested by Lauber et al., (1998), where g is the acceleration due to gravity and H is the impoundment depth in the reservoir behind the gate. This required gate opening time, t, had to be less than 0.2 s, 0.23 s, and 0.25 s for H = 200 mm, 250 mm, and 300 mm, respectively. The actual opening times were verified using high-speed imaging for the tests with H = 200 mm, 250 mm, and 300 mm, and they were 0.11 s, 0.117 s, and 0.13 s, respectively. Thus, the measured gate opening times satisfied the opening criteria by Lauber et al., (1998).

In total, 60 tests (including test repetitions) were conducted, among which 40 tests with an impoundment depth H = 300 mm were performed to test the repeatability and to validate the accuracy of pressure transducers. The tests with impoundment depths of H = 200 mm and 250 mm were repeated 10 times to obtain an accurate time-average water depth and dynamic pressure. Videos were recorded using GoPro cameras (Hero 5, GoPro Inc., San Mateo, CA, USA) with a resolution of 1080 × 1080 pixels. The videos were recorded in a linear mode to

avoid any image distortion, and they were converted to images with a frequency of 60 frames per second. All the experimental tests presented in this study are shown in Table 4.1.

Table 4.1 Experimental tests and surge properties

Test No.	*H*(mm)	Number of Repetitions
1	200	10
2	250	10
3	300	40

4.2.2 Pressure transducers

A Plexiglas wall was installed 1.1 m downstream of the tank to mount the pressure transducers in the wall (see Figure 4.1 b, d). Two different types of pressure transducers (HPT, TBFLPNS001BGUCV, Honeywell Sensing and Productivity Solutions, Charlotte, NC, USA) and ASC-calibrated pressure transducers (LMPT, LM31-00000F-005PG, TE Connectivity-Measurement Specialties, Hampton, VA, USA) were employed to measure the time-histories of the dynamic pressure on the vertical wall. The Honeywell (HPT) pressure transducer had a diameter of 4 mm, showed stable and accurate measurement in the calibration in static water, and was used to capture the vertical distributions of dynamic pressure in the centerline of the vertical wall (Figure 4.2 a).

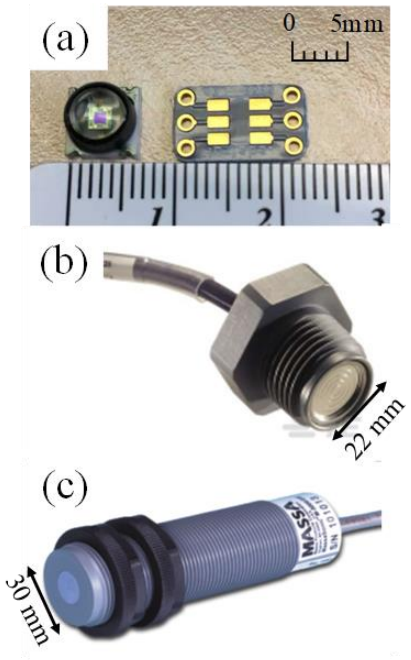

Figure 4.2 Instrumentation used for pressure and wave height measurements: (a) Honeywell Pressure Transducer (HPT); (b) TH connectivity LM-series Pressure Sensor (LMPS); c) MASSA M-5000/220 Ultra-sonic sensor (MUSS).

To provide support for the tiny transducer, make it easily mountable, and keep the sensing surface flush with the right wall, precise parts developed using 3D printing technology and screwed carp were used to assemble the transducer. Five HPT transducers were installed on the centerline of the wall in which the first transducer was located at the bed, while the other pressure transducers were located at 35 mm, 70 mm, 105 mm, and 140 mm above the bed. Three pressure transducers were also installed at the middle distance between the right wall and the wall centerline. These pressure transducers were installed at the same height as the first three transducers at the wall centerline, and they were employed to capture the three-dimensional motion of the wavefront (see Figure 4.1 b, d).

To evaluate the three-dimensional variations of surge waves and their impact on the wall and to validate the accuracy and reliability of pressure measurements, two ASC-calibrated LM pressure transducers with a sensing diameter of 22 mm were installed in the middle distance between the left wall and the wall centerline (see Figure 4.2 b). The accuracy of the LM pressure transducer was examined by measuring hydrostatic pressures of known water depths. Accurate measurements were obtained with less than 0.5% error. The dynamic performance of the LM pressure transducers was also examined to test the effect of the pressure sensing area on the accuracy of pressure measurement. The left LM and right Honeywell pressure transducers were installed at the same levels, and they were symmetrical about the central line of the wall (see Figure 4.1 b).

4.2.3 Ultrasonic wave sensor

The time-history of surge height close to the vertical wall was measured by an ultrasonic sensor (M-5000/220, MASSA, Hingham, MA, USA) which was placed above the tank next to the right wall at X = 1085mm. The MASSA depth sensor is able to record water level with a frequency of 2400 Hz and has the capability of non-contact distance measurement over a nominal target range of 100 mm to 1000 mm with a measurement resolution of 0.25 mm. The depth sensor was installed facing down, at the top of the experimental tank and close to the vertical wall (see Figure 4.1 a). The horizontal location of the depth sensor was adjusted to accurately capture the time-history of the surge height.

4.2.4 Data acquisition system

Two data acquisition (DAQ) boards (8-channels, HBM QuantumX MX 840B, Marlborough, MA, USA) and (16-channels, HBM QuantumX MX 1601B, Marlborough, MA,

USA) were employed for acquiring depth and pressure data. Both data acquisition systems have universal amplifiers with the capability of converting analog signals to 24-bit digital data with a sampling frequency of 2400 Hz. The maximum sampling frequency (i.e., f = 2400 Hz) was used to capture depth and pressure data. Data acquisition boards were integrated and synchronized using fire wires (1-KAB272-2, HBM, Marlborough, MA, USA) and then connected to the Cisco hub by Ethernet cables. A signal visualizer software (Catman-Easy, HBM, Marlborough, MA, USA) was used for sensor configuration, signal acquisition, data visualization, data analysis, and data storage during the measurements. The Honeywell Pressure Transducers (HPTs) were connected to DAQs, and they were calibrated by measuring the static pressure of a known water depth.

4.3 Pressure data analysis

As mentioned, the experiment using the impoundment depth of H = 300 mm was repeated 40 times, and the time-history pressure data was captured with a sampling frequency of 2400 Hz, at which stable and detailed pressure data can be obtained, although lower than the frequency of 10 kHz by Kim et al., (2015). The results were used to calculate the time-history of average horizontal dynamic pressure, P_x, and determine pressure fluctuations at the wall face at different elevations. Figure 4.3 shows the variations of the normalized horizontal dynamic pressure with normalized time. The horizontal dynamic pressure, P_x, was normalized by the static pressure at the initial condition, ρgH, where ρ is the density of water and time was normalized by the characteristic time scale, $T = (H/g)^{1/2}$.

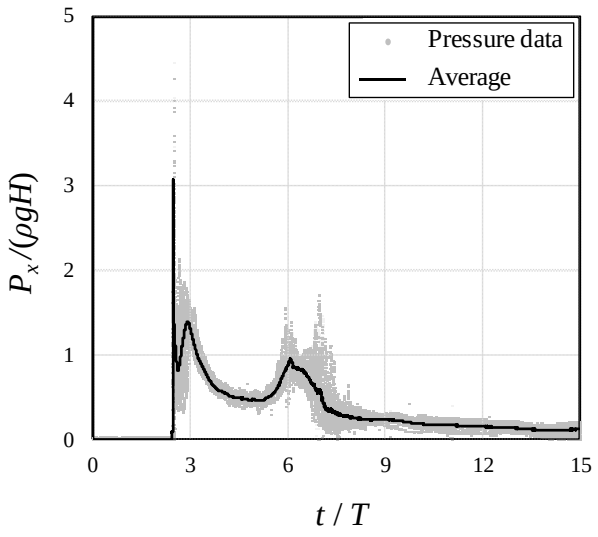

Figure 4.3 Time-history of the normalized pressure measured by Transducer 1. The gray area shows the cloud of data for 40 repetitions, and the solid curve represents the average pressure.

As shown in Figure 4.3, the first peak in time-history of normalized pressure had a value of $P_x/(\rho gH)$ = 3.18, and it occurred at approximately t/T = 2.3. After the first peak and at the initial impact, the normalized pressure decreased to $P_x/(\rho gH)$ = 0.8 and then increased to 1.4 at t/T = 3.0. After the pressure spike, the normalized dynamic pressure followed a U-shaped trend and reached $P_x/(\rho gH)$ = 1.0. The second pressure peak occurred at approximately t/T = 6.0.

A similar trend in the time-history of the dynamic pressure at the bed was reported in the experimental study of Kamra et al., (2018). The first peak in their study was 16.7% lower than the present study since the bottom transducers were positioned 3 mm to 4 mm above the tank bed. In addition, the magnitude of the first non-dimensional pressure peak, $P_x/(\rho gH)$, was 3.18, which was similar to the observations of Lobovsky et al., (2014), with a value ranging between 2.8 and 3.2. Despite the size variations between Lobovsky et al., (2014) and Kamra et al., (2018) and the present study, non-dimensional dynamic pressures were found to be approximately three

times the initial static pressure in the reservoir. A similar relationship between dynamic and static pressures was also recommended by the SMBTR tsunami-design guideline as an estimate of the maximum hydrodynamic force due to tsunami loading (Okada et al., 2005c). A comparison of the normalized dynamic pressure with the literature indicated that the selected pressure transducers and data acquisition units accurately captured the pressure field.

The time-histories of dynamic pressure at different locations on the wall were measured with pressure transducers on the centerline, left, and right sides of the centerline 110 mm apart (see Figure 4.1 b, d). The recorded pressure data were further employed to investigate the three-dimensional motion and asymmetry in the surge front impact with a vertical wall (see Figure 4.4). It was indicated that pressure signals could be quite different when applying different transducers (Kim et al., 2015). Thus, the dynamic pressure data, induced by a 300 mm dam-break surge on the vertical wall, was validated by comparing the pressure data from different transducers at the same level. As shown in Figure 4.4, the centerline pressure transducers were labeled with a number, and the left and right-side transducers were also labeled with L and R, respectively.

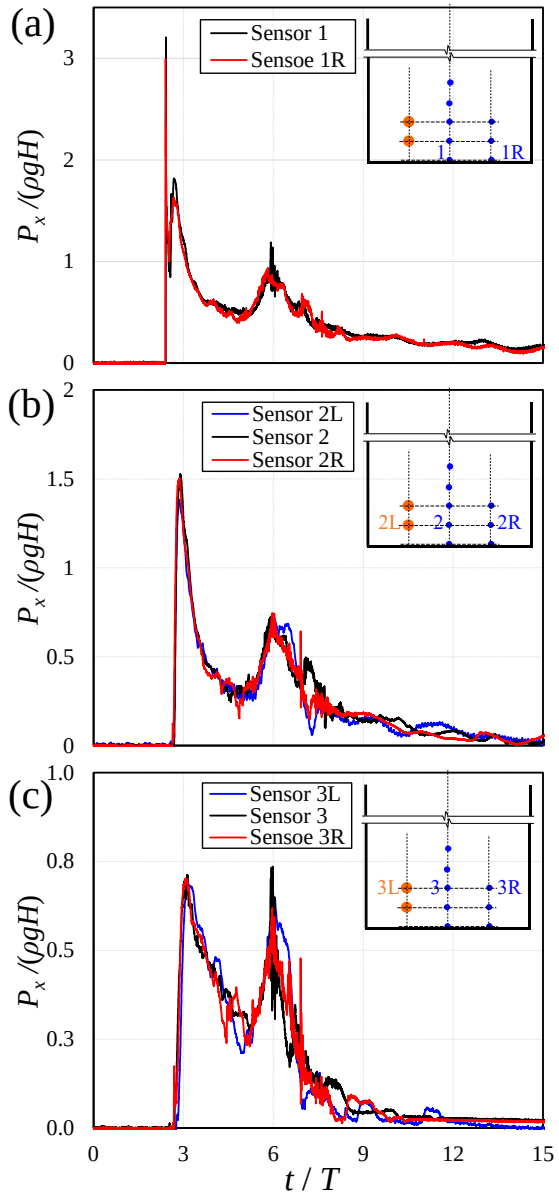

Figure 4.4 Time-history of non-dimensional horizontal pressure at different levels from the flume bed: (a) z = 2 mm, transducer 1 and 1R; (b) z = 35 mm, transducer 2, 2L, and 2R; (c) z = 70 mm, transducer 3, 3L, and 3R.

Figure 4.4a show the variations of normalized horizontal pressure with non-dimensional time in the centerline and right side of the wall and close to the bed (i.e., transducers 1 and 1R). The time histories of dynamic pressure due to the impact of the surge generated by the

impoundment depth of H = 300 mm with a vertical wall were recorded. The horizontal pressure data were normalized with the initial static pressure of the impounding reservoir (ρgH), and the time was normalized with the characteristic time scale (i.e., $T = (H/g)^{1/2}$). The high similarity between the recorded pressure data from Transducers 1 and 1R indicated that the surge wave was two-dimensional at the bed location. The impact pressure at the centerline of the wall (transducer 1) was 7.8% higher than the first pressure peak recorded by the transducer 1R. The difference between the impact pressure at transducers 1 and 1R may be due to the side walls resistance effect, which slightly delayed the wave near the right wall, resulting in a lower impact pressure at the transducer 1R. Figure 4.4b show the time-history of dynamic pressure at z = 35 mm above the bed. As it can be seen, the time histories of dynamic pressures were identical for transducers placed at the same level, and the pressure data were similar in the centerline, on the left and right sides of the vertical wall. The pressure data indicated that both types of pressure transducers were able to capture the time-history of dynamic pressure accurately. In other words, the accuracy of micro pressure transducers was compared and validated with the larger LMPT. At this transducer level, the peak dynamic pressure was 1.5 times the initial static pressure at the reservoir. The second peak in the time-history of dynamic pressure occurred at $t/T \approx 6$, and it was 70% of the initial static pressure at the reservoir.

Figure 4.4c shows the variations of dynamic pressure with time at elevation z = 70 mm above the flume bed on the left, right, and centerline of the vertical wall. The peak pressures due to the surge impact were virtually identical for transducers located at the same elevation on the wall and 70% of the initial static pressure at the reservoir. The second peak in time-history of dynamic pressure had the same value as the first peak, around 0.7, and occurred at $t/T \approx 6$. The

difference between the second pressure peak in the sides and centerline of the vertical wall was -8.6%. As shown in Figure 4.4, the bottom transducers captured the highest pressure, which indicated the similarity between the recorded pressures in the sides and centerline. The small pressure differences at the bottom may be due to pressure fluctuations because of non-linear and non-uniform wave propagation along the right wall. Similar symmetry in the time-history of dynamic pressure at the bed was observed in tests with H = 200 mm and 250 mm as well.

The reliability and accuracy of the HP transducers were verified in the pressure comparison study. As a result, the miniaturized HPTs were employed for the dynamic pressure measurement.

4.4 Results and discussion

In this section, the experimental results of free surface profiles and dynamic pressure of dam-break wave were presented and discussed. All the data are available in the supplementary material.

4.4.1 Free surface profiles

Free surface profiles of a dam-break-induced surge at different propagation instants can provide valuable information on the motion and kinematics of surge impact on a vertical wall. To differentiate the water from other components and better visualization, blue dye was used for coloring, similar to the research by Hernández et al., (2018). Figure 4.5 shows the variations of free surface profiles with time for a surge with an impoundment depth of H = 250 mm.

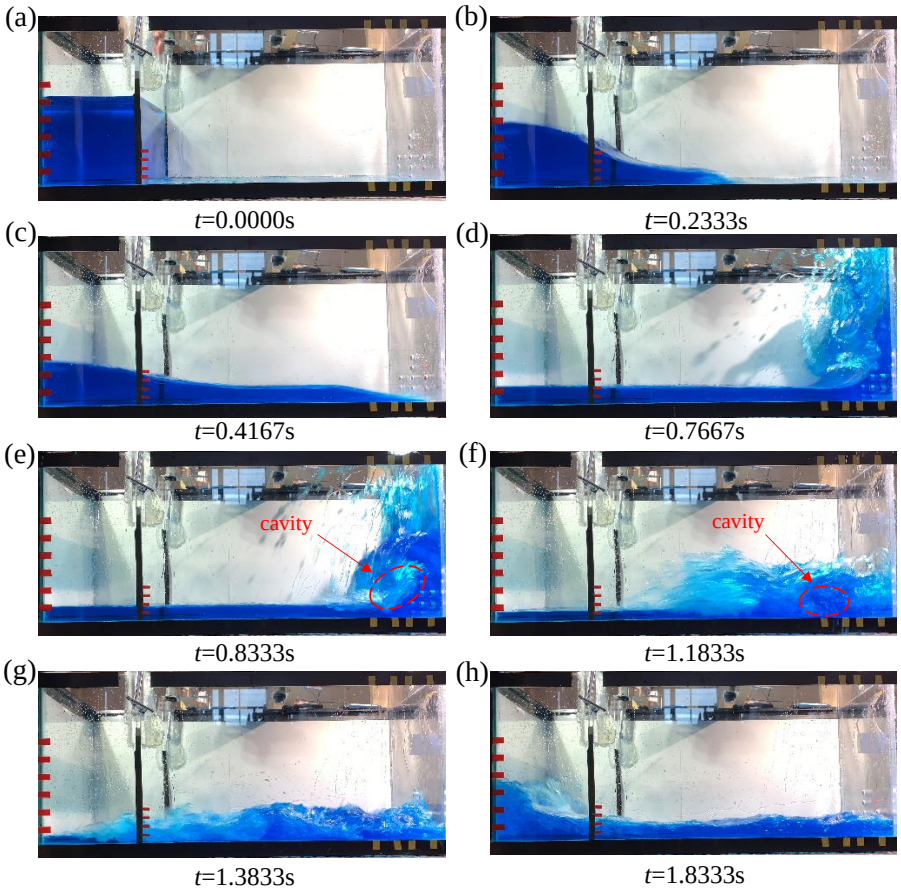

Figure 4.5 Time series of raw images of the turbulent bore front propagation, impact on a vertical wall, and return wave for a bore generated from an impoundment depth of H = 250 mm: (a) t/T = 0; (b) t/T = 1.4614; (c) t/T = 1.7769; (d) t/T = 3.2694; (e) t/T = 3.5534; (f) t/T = 5.0458; (g) t/T = 5.8987; (h) t/T = 7.8176.

The interaction of a dam-break-induced surge with a wall can be studied through different stages of impact, runup, falling, and breaking. The wave-wall interaction stages are shown in Figure 4.5. Figure 4.5a show the initial condition, as water is stored in the reservoir, while Figure 4.5c show the surge impact on the wall at t = 0.4167 s.

After the impact, the water level close to the wall increased until all kinetic energy of the surge was converted to potential energy, and the wave reached the highest level of approximately

two times that of the impoundment depth (see Figure 4.5d). The splashing of the surge front is correlated with the tank width, and splashing does not normally occur in relatively narrow tanks. No surge front splash was reported in the study of Lobovsky et al., (2014), who used a tank width of w = 150 mm and Kamra et al., (2018), who used a tank width of w = 200 mm. The splashed-up water returned to the tank and formed a water tongue (see Figure 4.5d). The water tongue rolled and formed a breaking wave or plunging breaker (see Figure 4.5e), and then a cavity volume formed between the frontal part and the delayed backwater (see arrow pointed Figure 4.5e, f). Afterwards, the surge impacted the bed and propagated backwards towards the reservoir and hit the left wall (see Figure 4.5g, h). The wave then runup, rolled water, and cavity formation was also observed in the experimental studies of Hu et al., (2010) and Kamra et al., (2018), as well as in the numerical study of Liu et al., (2018).

The Froude number (ratio of gravitational and inertial force) of the wavefront was around 1.4 when the dam-break wave approached the right wall; however, a breaking wave was not observed when Fr exceeded the critical value of 1.0 (Kocaman et al., 2020), as shown in Figure 4.5c. Meanwhile, the maximum Weber number (ratio of inertial force and surface tension) in the experiment could reach around 5.0×10^4 when the wave impacted the right wall and during the interaction. Therefore, the gravitational force became dominant in the propagation of the dam-break wave. Next, it can be observed in Figure 4.5d-g that the turbulent flow developed in the dam-break wave, with a Reynolds number (ratio of viscosity and inertial force) around 1.2×10^6 exceeding the value of 1.0×10^6, which is typically associated with tsunami wave inundation (Stolle et al., 2019a).

4.4.2 Time-history of the water surface elevation

The time-histories of the water surface near the vertical wall and for different impoundment depths are shown in Figure 4.6. The measured water surface level at the wall varied from zero, then increased dramatically, reached the peak within a fraction of a second, and then decreased during the rolling-back stage.

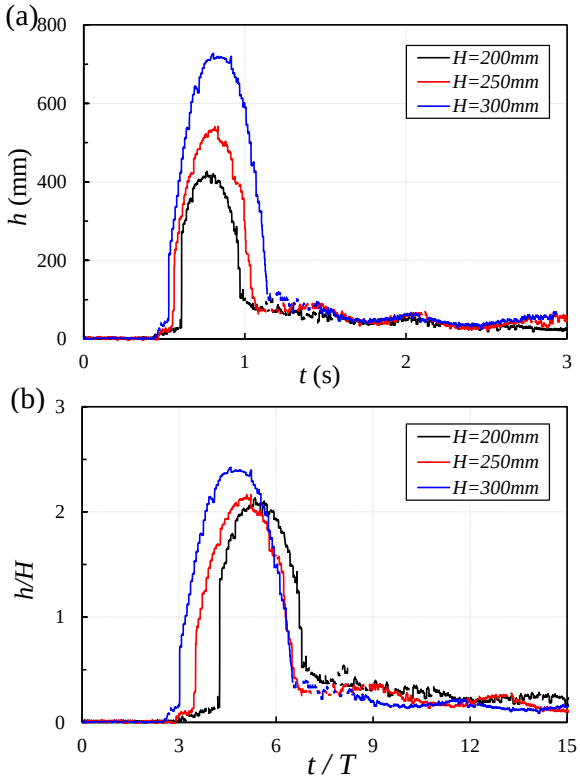

Figure 4.6 Time-history of the surge runup height near the vertical wall for different impoundment depths: (a) variations of the surge height with time; (b) variations of the normalized runup height with the non-dimensional time.

Figure 4.6a show that the peak surge height increased with increasing impoundment depth, H, and the arrival time of the wavefront decreased as the impoundment depth increased. In addition, it took more time for the waves generated by higher impoundment depth to reduce the

agitation. As a result, the rise and draw-down cycles are prolonged in waves with higher impoundment depths. Figure 4.6b show the correlation of normalized surge height with time. The surge height was normalized by the impoundment depth, H, and the time was normalized with the characteristics time scale, T. Higher impoundment depth generated higher momentum of flows, and the peak surge height increased non-linearly with the impoundment depth. The normalized peak surge heights were 2.03, 2.09, and 2.35 times the corresponding impoundment depths for H = 200 mm, 250 mm, and 300 mm, respectively. The duration between the wave runup and tongue collapse back onto the bed was labeled as τ in this study. The duration of the wave runup for H = 200 mm, 250 mm, and 300 mm was 0.60 s, 0.68 s, and 0.8 s, respectively.

4.4.3 Dynamic pressure

Figure 4.7 show the time-histories of dynamic pressure from five micro pressure transducers and for three different impoundment depths, with H = 200 mm, 250 mm, and 300 mm in Figure 4.7a, b, and c, respectively. The pressure transducers were installed in the centerline of a vertical wall and at five different heights from the bed upward. At the initial impact, the pressure data of the transducer closest to the bed immediately reached the first peak and rapidly decreased afterwards for all three cases. However, a small but sudden pressure spike after the peak around 0.41s was observed for the surge generated by the higher impoundment depths, H = 250 mm and H = 300 mm, as shown in Figure 4.7b, c. Such pressure spikes were also found in the experimental observations of Nouri et al., (2010) and Kamra et al., (2018). The peak dynamic pressure at the bed level transducer occurred due to the surge front impact onto the wall. Immediately after the first impact, the surge front was diverted vertically along the wall, and the horizontal pressure decreased. At this instant, the inertia of the remaining volume of

water moving toward the wall generated a pressure wave, which resulted in a spike following the peak pressure. The current observations indicated that the magnitude of the spike was correlated with the volume of water and thus impoundment depth. As shown in Figure 4.7c, the magnitude of the pressure spike was slightly higher than 5 kPa for H = 300 mm whereas for H = 250 mm, the pressure spike was around 3 kPa.

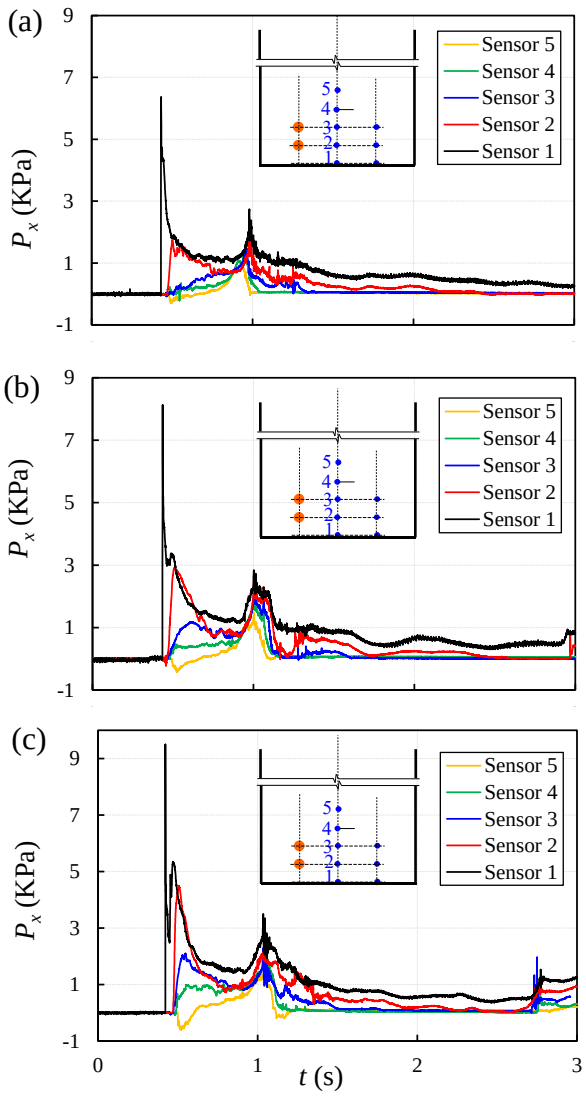

Figure 4.7 Time-history of the horizontal dynamic pressure at different elevations along the vertical wall: (a) H = 200 mm; (b) H = 250 mm; (c) H = 300 mm.

The transducer closest to the flume bed recorded the highest dynamic pressure compared to the other transducers located at higher elevations on the wall. After the first pressure peak, the dynamic pressures of transducers 1 and 2 dropped and reached a plateau between 0.6 s and 0.8 s in all the three cases and also for transducer 3 in H = 250 mm and 300 mm cases. The second pressure peak increasing dynamic pressure was observed at transducers 4 and 5 from the initial impact until the second peak, which occurred during the downward and falling phase of the water tongue. This reduced the impact effects on the still advancing water surge, which continued to advance towards the wall. Negative pressure signals were recorded by the top transducer 5 at the initial interaction with runup wave. The formation of negative pressures was due to the suction effects generated the vertical motion of wave runup. The magnitude of the negative pressure increased with increasing impoundment depth. Afterwards, the wave broke and propagation slowed down; thus, dynamic pressure reached the quasi-steady state.

To investigate the relationship between dynamic pressure and initial hydrostatic pressure, pressure data were normalized with the initial static pressure, and the results were plotted using a non-dimensionalized time. Figure 4.8 show the experimental results in the form of normalized pressure and time for different reservoir depths of H = 200 m, 250 mm, and 300 mm. Transducer 1 experienced the largest pressure with values of 3.01, 3.12, and 3.18 times larger than the initial hydrostatic pressure for H = 200 mm, 250 mm, and 300 mm, respectively. The non-dimensional dynamic pressures in other transducers and for all impoundment depths were approximately below 1.5. After the second pressure peak, transducers 1 and 2 had only shown non-zero pressure, while the non-dimensional pressure in other transducers was close to zero. This indicated that all transducers, except transducers 1 and 2, were exposed to the atmosphere. The

non-dimensional pressure data from transducer 1 showed that the dynamic pressures were equivalent to the initial static pressure at the reservoir, and they occurred at t/T = 6, which is consistent with observations of Lobovsky et al., (2014). The pressure recorded by transducer 1 was steady after the second wave with a value between 0.51 and 0.52 of the initial static pressure, and they occurred at the non-dimensional time, t/T, between 4.3 and 5.3.

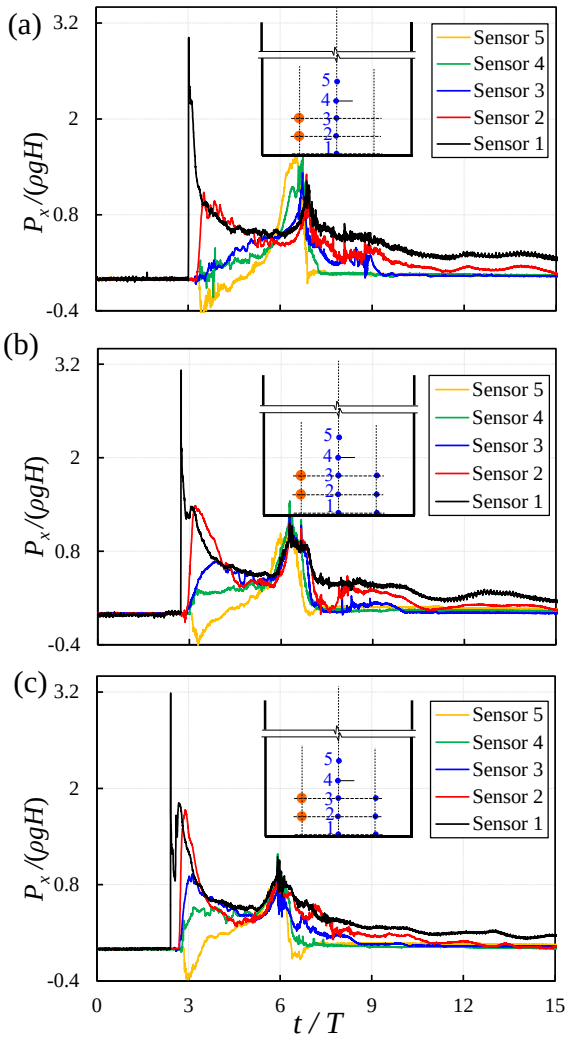

Figure 4.8 Normalized horizontal dynamic pressure with non-dimensionalized time: (a) H = 200 mm; (b) H = 250 mm; (c) H = 300 mm.

Previous experimental observations on hydrodynamic loading due to tsunami waves indicated that the maximum impact force occurred at initial impact (Nouri et al., 2010; St-Germain et al., 2014). Once the wavefront passes the structure, the tsunami-induced dynamic loading decreases rapidly despite the continuous propagation of the wave. Figure 4.9 shows the correlation of the normalized dynamic pressure in the horizontal direction and surge height with time for three different impoundment depths of H = 200 mm, 250 mm, and 300 mm.

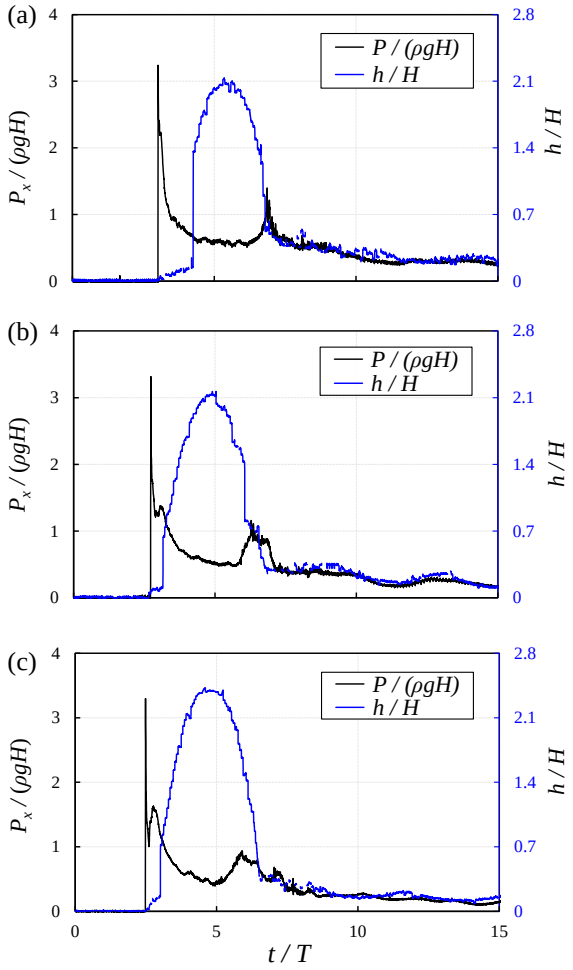

Figure 4.9 Non-dimensional time−history of the horizontal dynamic pressure and surge height for different impoundment depths: (a) H = 200 m; (b) H = 250 mm; (c) H = 300mm.

The dynamic pressure instantly reached its peak value due to surge front impact, while the surge height only reached its peak afterwards. The surge runup and, over time, increasingly, the dynamic energy converted into potential energy, an observation confirmed by the reduction in flow velocity as it ran up the wall. The peak surge height reached its maximum once the pressure approached its minimum at $t/T \approx 5$ (see Figure 4.9), as at this moment, the flow kinetic energy was fully converted into potential energy. When the surge height decreased from the peak, dynamic pressure increased within a small range from its minimum value and the second pressure peak occurred around $t/T = 6$, with corresponding side surge view images shown in Figure 4.5e, f.

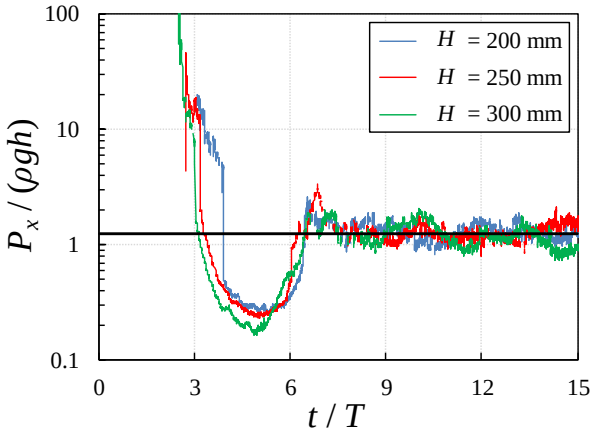

Figure 4.10 Non-dimensionalized time-history of the ratio of dynamic pressure to instantaneous wave hydrostatic pressure for different impoundment depths. Pressure data from transducer 1.

Figure 10 shows the three different impoundment depths cases and the time-variable ratio of hydrodynamic pressure from transducer 1 to the instantaneous hydrostatic pressure caused by the inundation on it. For a better representation of the variation of the hydrodynamic to the hydrostatic pressure ratio, the vertical axis is logarithmic. The pressure data reached their peak values, and surge heights were nearly zero at the beginning of the tests. Therefore, the ratio of

the dynamic to static pressure became infinitely large, and, as a result, the ratio data at the beginning of the tests were truncated for better data visualization.

The dynamic pressure was dominant at the time of impact, and it reached the equilibrium level for $3 \leq t/T \leq 4$. It is noteworthy to mention that the ratio of dynamic to static pressure reached its minimum value at $t/T = 5$, and it was almost independent of impoundment depth. The minimum dynamic to static pressures ratio was between 0.15 ρgh and 0.3 ρgh. The dam-break waves reached their equilibrium at $t/T = 6.5$, from which the pressure in transducer 1 recorded static pressure, i.e., the second peak in the time-history of pressure data became comparable with the hydrostatic pressure (i.e., $P_x/(\rho gH) \approx 1$). The downward acceleration of flow along the wall generated a suction force which led to the pressure drop in the horizontal direction.

4.4.4 Vertical distribution of dynamic pressure along the wall

The vertical distribution of dynamic pressure along the wall can provide valuable information when structures are impacted by tsunami-induced hydrodynamic loadings. The information assists engineers in properly designing critical coastal infrastructure. The impact time was divided into two segments to study the vertical distribution of dynamic pressure along the wall. The time, t_m, was selected as a time when the surge first hit the vertical wall. The first segment shows the variation of the dynamic pressure between the initial impact time (i.e., $t_m = 0$ s) and 0.1 s after the impact. The second pressure peak occurred between $t_m = 0.5$ s and 0.7 s after the initial impact (see Figure 4.7). Figure 4.11 shows the vertical distribution of dynamic pressure for two segments of time and different impoundment depths.

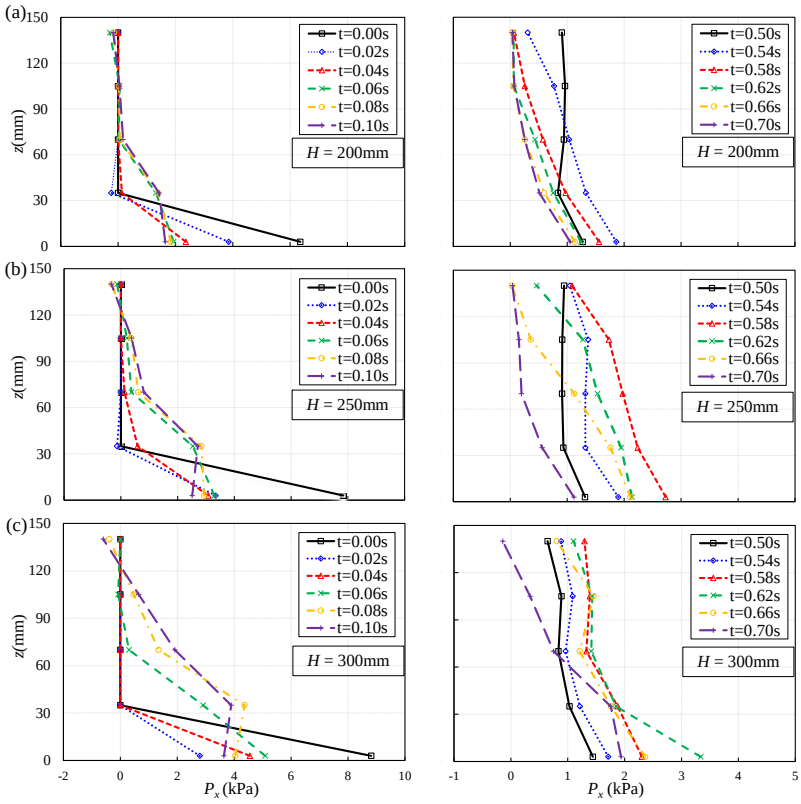

Figure 4.11 Vertical distributions of the dynamic pressure on the wall around the initial impact and the second pressure peak for different impoundment depths: (a) H = 200 m; (b) H = 250 mm; (c) H = 300 mm. The t_m = 0.00 s indicates the initial impact of the bore front with the vertical wall.

At H = 200 mm impoundment depth, the largest dynamic pressure that occurred in the first peak was observed close to the bottom of the tank (i.e., at transducer 1 shown in Figure 4.1a). From t_m = 0.00 s to t_m = 0.04 s, the peak pressure was at the bottom of the tank, and the bottom pressure values decreased with time. At t_m = 0.06 s, the higher-level transducers recorded positive pressure values while transducers 3, 4, and 5 recorded zero pressure. Negative pressure values were recorded slightly after the initial impact, and their value increased with increasing impoundment depth. For H = 200 mm, the values of pressure at the bed decreased with time;

however, for H = 250 mm, dynamic pressure values at the bed level decreased first and then increased at t_m = 0.06 s. The difference between the bottom dynamic pressures was due to the spike dynamic pressure value described in Figure 4.4. The negative pressure in transducer 5 occurred at t_m = 0.08 s and t_m = 0.10 s and for higher impoundment depths. These negative pressures occurred due to the suction effect that was developed by the wave runup. Meanwhile, the pressure values at the bottom of the tank (i.e., transducer 1) dropped to around 25%, 30%, and 40% of the initial impacting pressure for H = 200 mm, 250 mm, and 300 mm, respectively.

The right column in Figure 4.11 show the vertical distribution of dynamic pressure in the second time segment (0.5 s $\leq t_m \leq$ 0.7 s). During the second time segment, a relatively uniform pressure distribution was recorded at t_m = 0.5 s. Over time, the pressure distribution was changed to one similar to hydrostatic pressure distribution. As can be seen in the right column of Figure 4.11, the second peak pressure occurred when the maximum dynamic pressure distribution was recorded. The time to reach the peak pressure, tm, was delayed by 0.04 s when impoundment depth increased to t_m = 0.54 s, 0.58 s, and 0.62 s for H = 200 mm, 250 mm, and 300 mm, respectively. A comparison between the first and second segments indicated that the pressure distributions changed less abruptly during the second time segment than the initial impact time. The spatial distribution of pressure increased before the peak pressure occurred, and it decreased after the peak pressure. For example, for a test with H = 250 mm and before the peak pressure (i.e., t_m = 0.58 s), the pressure increased from tm = 0.50 s (i.e., black line) to t_m = 0.54 s (i.e., blue line) and then the pressure decreased after the peak.

4.5 Discussion

The present experimental study demonstrated the variation between kinematic behaviors and dynamic pressure of dam-break flow impacting a vertical wall. The free surface profiles were found to be consistent with previous studies (Kamra et al., 2018; Hu et al., 2010), and the ratio of maximum surge height to initial impoundment depth fitted well in a reasonable range, around 2.1–2.3, when compared with the experimental study (Kamra et al., 2018) and numerical simulation (Liu et al., 2018). Compared to the time-history of the dynamic pressures presented by Lobovsky et al. (2014), it should be pointed out that the spike observed after the first peak pressure was observed in transducer 1. This was also exhibited in the experiments by Nouri et al. (Nouri et al., 2010) and Kamra et al. (Kamra et al., 2018). A hypothesis was put forward that this phenomenon was caused by the pressure wave generated by the surge front during impacting. The analysis approach applied in the experimental study could be applied to investigate the loading on nearshore infrastructure.

This study provided new insight into the relationship between surge waves and the exerted dynamic pressure by dam-break flows. The authors acknowledge some limitations in their experimental study conducted in a laboratory tank with relatively small dimensions. Scale effects should be considered based on the prototype of coastal infrastructures for the design of practical engineering, which requires further research.

4.6 Conclusion

In this experimental study, the dynamic behavior of dam-break-induced surge interactions with a vertical wall was investigated by means of pressure transducers, ultrasonic water level transducers, and video-camera images. Our conclusions are summarized as follows:

- Detailed analysis of time-history of the water surface profiles revealed four stages of surge motion during impact with a vertical wall. The four stages of wave–wall impact were (1) impact, (2) runup, (3) fallback, and (4) breaking. The recorded time-histories of the surge depth indicated that the runup depth and impact duration increased when the impoundment depth increased.
- Peak horizontal dynamic pressures were extracted from time-history for different water elevations to study the pressure distribution of the surge during the impact. It was found that the horizontal dynamic pressure at the bed was three times higher than the initial hydrostatic pressure at the reservoir location. Negative pressures generated by the suction effect generated during the fast runup were observed all the way up at the highest transducer level (i.e., z = 140mm).
- The time lag between the horizontal dynamic pressure and surge height showed an inverse relationship between dynamic pressure and surge height curves during the impact. It was found that the horizontal dynamic pressure reached its maximum value when the wave runup height was at its minimum level. After the surge started falling off the wall and breaking at its base, on the bed, the magnitude of the dynamic pressure was close to that of the hydrostatic pressure. Additionally, a detailed analysis of the dynamic to static pressure ratio at transducer 1 showed that the normalized pressure was independent of impoundment depth.

Notation

The following symbols are used in this paper:

g = gravitational acceleration, m/s^2;
h = wave height along the right wall, m;
H = initial impoundment depth, m;
t = time, s;
t_m = time since the initial impact, s;
T = characteristic time scale, s;
P_x = dynamic pressure on the transducers, kPa;
u = wave front velocity, m/s;
w = tank width, m;
X = horizontal direction;
Y = transverse direction;
Z = vertical direction, perpendicular to the XY plane;
z = elevation, mm;

Chapter 5 Experimental Investigation of Beach Slope Effects on the Kinematic Behaviors of Dam Break Flow

Abstract

Over the past decades, dam break flows generated by the sudden release of a prescribed volume of water have been adopted as a practical way to simulate and investigate tsunami-like, overland flowing bores. Extensive experimental and numerical modeling research related to dam break waves have been conducted for the case of propagation over horizontal beds. However, natural and artificial beaches exhibit slopes which significantly influence the kinematic behavior of propagating tsunami inundation. The objective of this study was to experimentally investigate the effects of the beach slope on dam break waves in terms of kinematic behavior during their propagation, interactions with and runup onto the structural wall. The physical tests were conducted in the Water Resource Engineering Laboratory at the University of Ottawa, Canada, using a rectangular tank with an impoundment depth of 250 mm. To simulate the inclined beds, 4 different slopes of 0, 5, 10 and 15 degrees were designed and installed at the bottom of the tank, against the downstream vertical wall. Ultra-sonic sensor placed in the vicinity of the impacted wall was used to record the time history of the bore runup on the wall. The free surface profiles at different instants were processed from video recorded using a high-speed camera. The wave front spatial advancement was obtained from the raw images extracted from the recorded bore propagation video. An analysis of the free bore surface showed that its shape only changed as it propagated over the slope. Lower runup heights of the bores on the wall were observed for the sloped cases, with maximum heights being 15 mm, 48 mm and 71 mm lower than those

propagating over the horizontal bed, corresponding to the 5-, 10- and 15-degree slope cases. The wave front spatial advancement and velocity magnitude showed a decelerating effect of the slope on propagation of the bores. The arrival time and impact of the wave front on the downstream right wall was delayed by 0.15 s between adjacent cases from 0 to 15 degrees. The results of this study will be of assistance in the design of coastal infrastructure for inundation protection in tsunami prone areas.

Keywords: tsunami-like hydraulic bores, dam break flow, bed slopes, experimental investigation, kinematic behaviors

5.1 Introduction

As extreme natural disasters, tsunamis have caused severe damage to coastal communities in the past decade (Nistor et al., 2011), i.e., the 2004 Indian tsunami, 2010 Chile Tsunami, 2018 Indonesia Tsunami and, recently, the 2022 Tonga Tsunami. In these events, the affected areas were flooded by tremendous amount of seawater, which led, among others, to the failure of coastal infrastructures. An insight study regarding the kinematics of tsunamis can help provide instruction on emergency evacuation and inundation design of coastal infrastructures. Thus, the kinematic behaviors of tsunami-like waves, including wave propagation over the bed and inundation on structures is very important and further research is urgently needed.

Based on the analytical solution of the dam-break wave proposed by Ritter (1892) and method of characteristics, Chanson (2005, 2006b) developed the calculation formula by considering the resistance of the wave tip region on a horizontal dry bed. The free surface profile with developed wave tip region using a modified solution (Chanson 2009) demonstrated better

agreement with previous experiments (Dressler 1952; Whitham 1955). A numerical study by Yang et al., (2018a) revealed that the analytical free surface by Chanson (2005, 2006b) agreed reasonably well with experiments (Ozmen-Cagatay et al., 2010) and numerically simulated results by Flow-3D, except for a slight deviation in the upstream edge area. Numerous researchers have demonstrated that the free surface study of dam-break flow by analytical solution (Chanson 2005, 2006b; Wang et al., 2020; Leal et al., 2006; Castro-Orgaz et al., 2017b), experiment (Kamra et al., 2018; Lobovsky et al., 2014) and numerical simulation (St-Germain et al., 2012; Yang et al., 2018a; Yilmaz et al., 2021) can provide kinematic details about the time-varied wave propagation.

The propagation of a dam-break wave develops very rapidly at the initial stage due to its dynamic property of transition and non-uniformity under gravity (Hsu et al., 2014). In addition to the wave tip celerity obtained by analytical solution (Chanson 2005; Deng et al., 2018; Chanson 2006b; Leal et al., 2006) to describe the disturbance or change in wave phase, the velocity field of wave front was more direct and effective in assessing the propagation of dam break flow, but little research focused on this. In the analytical solution by Ritter (1892), the maximum value of averaged wave front velocity was found as $2\sqrt{gh_0}$ (Lauber et al., 1998), where h_0 is the initial impoundment depth. Yang et al., (2018b) numerically simulated the characteristics of dam-break flow using *Flow-3D* and presented the time history data of wave front velocity in the dry bed case with 250 mm impoundment depth. As indicated by the time-history of wave front velocity, with the impounded water column falling down, the velocity continued increasing as potential energy was quickly converted to kinetic energy. After reaching a maximum value of 2.7 m/s and remaining relatively stable between 0.3 s and 0.6 s, the velocity gradually decreased due to its

conversion into potential energy and the bed resistance. The maximum wave front velocity in this study was approximately $1.72\sqrt{gh_0}$, smaller than the value of $2\sqrt{gh_0}$ proposed by Ritter (1892).

In summary, numerous studies have been conducted to investigate the kinematics of dam break flow regarding the free surface profile and wave front celerity; however, few have investigated the wave propagation velocity. Meanwhile, it can be noticed that most of the dam-break related research was conducted on a horizontal bed. However, slopes are prevalent in coastal regions and play an important role in the kinematic behaviors of tsunami-like waves. Few studies were found that investigated the slope effects on the kinematics of dam-break waves, i.e., how the free surface and wave propagation will change when taking the slope into consideration.

The primary objective of this study was to investigate slope effects on the kinematics of dam-break flow experimentally, with respect to the wave free surface profile, wave runup height, wave front location and its little-studied velocity. Specifically, the experimental apparatus was designed with several different slopes to reveal the differences between various sloped cases. To the authors' knowledge, this is the first study to investigate the slope effects on the kinematics of dam-break waves, especially on the wave front velocity.

5.2 Experimental setup

A series of physical tests were performed in the Water Resource Engineering Laboratory of the University of Ottawa in Canada. A 1.2 m long, 0.44 m wide and 0.5 m high glass tank with a plexiglass sheet installed at X = 1.1 m perpendicular to the bed, serving as both the downstream right wall and a vertical-release gate system at X = 0.25 m, was applied to impound

water and generate the dam break flow. In the experimental apparatus, 3 removable plexiglass sheets were designed and installed to act as the 5-degree, 10-degree and 15-degree slopes, and a camera were used for video recording, as shown in Figure 1. To record the wave runup along the right wall, an ultra-sonic sensor (M-5000/220, MASSA, Hingham, USA) was installed in the middle line of the tank, overhead and next to the right wall at X=1090 mm, as shown in Figure 1. This sensor incorporates state-of-the art ultrasonic technology that ensured precision non-contact distance measurement over a nominal target range of 100 mm – 1000 mm (4”- 40”). A high-speed GoPro camera (Hero 5, GoPro Inc., San Mateo, USA) was located in the center front of the tank to record the dynamic history of wave propagation.

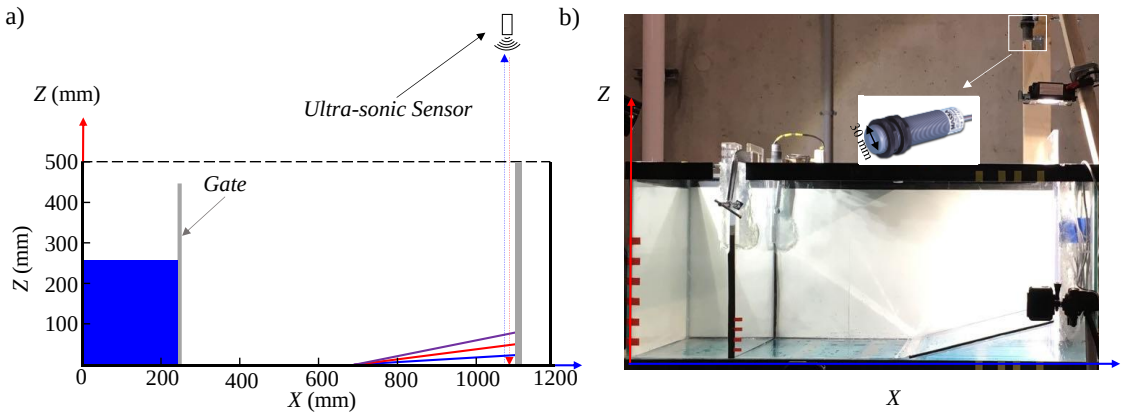

Figure 5.1 Experimental apparatus setup and coordinates system: (a) schematic of the experimental setting, (b) front view of the experimental setting for 15-degree case and the location of installed MASSA ultra-sonic sensor (MUSS)

The dam break experiments were conducted with upstream impoundment depth H_0 = 250 mm and 4 different downstream slopes, 0- (horizontal bed), 5-, 10- and 15-degree. The test matrix is shown in Table 5.1:

Table 5.1 Dam-break tests

Slope	Impoundment Depth	Device
0°	250 mm	1 GoPro 1 MUSS
5°		
10°		
15°		

5.3 Experimental post-processing methodology

As introduced in the previous section, dynamics of the wave propagation of dam break flow was recorded by a GoPro camera at a rate of 60 fpm. Thus, the free surface profiles at different time instances can be extracted from the video for kinematic characteristics analysis. When the propagated wave arrived at the right wall and started running up, the distance change, $D_{t,}$ between the sonic sensor and water surface was recorded. Moreover, the wave runup height history was calculated by subtracting the distance D_t from the initial distance D_0. To obtain the desired physical characteristics with respect to the slope effects investigation, some novel postprocessing methods were used in this study, with a focus on the wave front location and its velocity.

- The raw images of free surfaces were imported into Engauge Digitizer (Mitchell et al., 2021), where the origin and axis were defined as illustrated in Figure 5.1(a). After setting set points on the free surface curves, the graphs were converted to digital data points and exported as text file. By plotting altogether the data points at the same time instance from different cases, the differences between water surface profiles can be visually presented and analyzed.

- To obtain wave front location, a scale was set along the tank's x-axis and the authors tracked the raw images of free surface profiles at each frame before the wave hit the right wall. By tracking the wave front advancement on the scale, it location of t was obtained with an accuracy of 0.2 cm. Furthermore, the wave front location distance between each frame was calculated and divided by the time interval of 1/60 s to obtain the average wave front velocity.

5.4 Results

The slope effects on the kinematics of dam break waves are presented and discussed in this section, in the following order: the free surface profiles, wave runup height on the right wall, the location and velocity of wave front. For all the cases in this paper, the time origin t=0 was set at the moment when the gate started opening. Thus, the impounded water column collapsed at t=0.0s.

5.4.1 Free surface profile

The raw images of free surface profiles at different time instances from all 4 cases are presented in Figure 5.2 to show the slope effect on the kinematics of dam break wave, including the stages of wave propagation on horizontal and inclined bed, runup on the right wall, falling down, overturning and breaking.

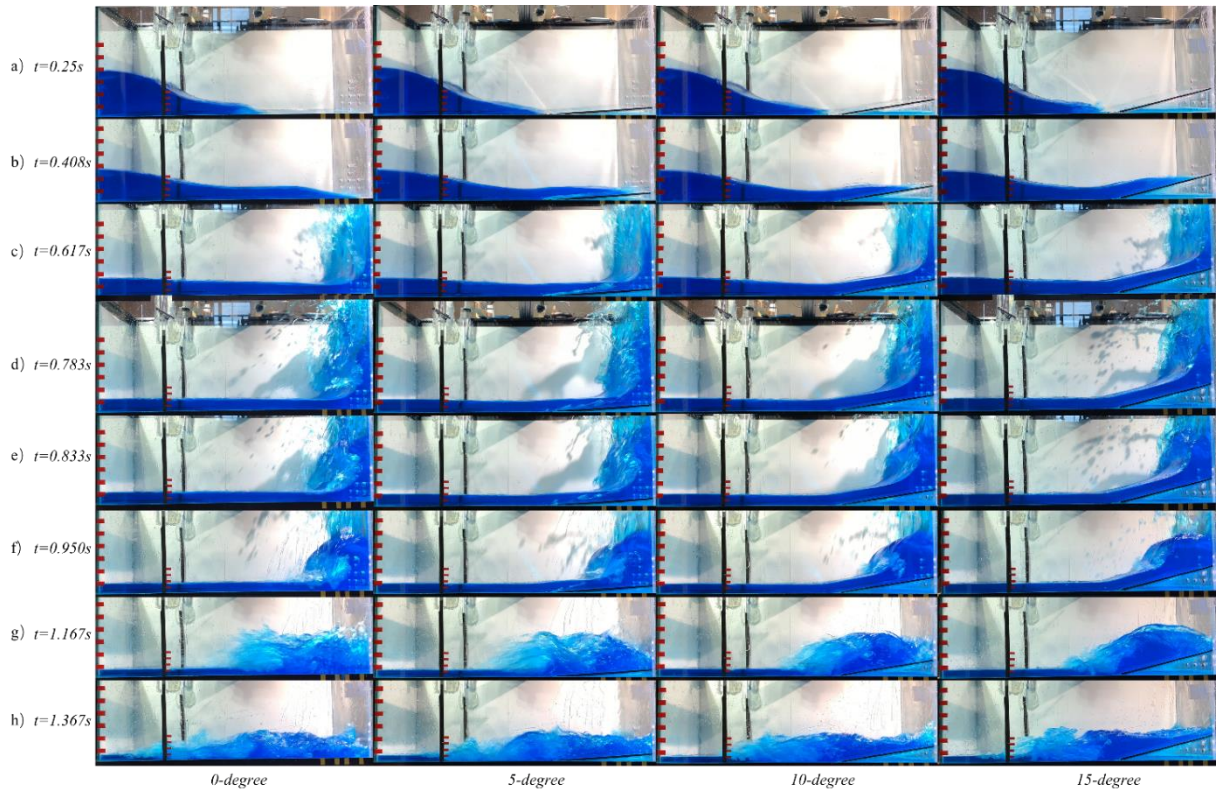

Figure 5.2 Raw images of free surface profiles at t = 0.25 s, 0.408 s, 0.617 s, 0.783 s, 0.833 s, 0.950 s, 1.167 s, 1.367 s from horizontal, 5 -, 10 - and 15 - degree cases.

For a quantitative comparison, the water surface profiles before wave breaking were digitized using the Engauge Digitizer and plotted together as shown in Figure 5.3.

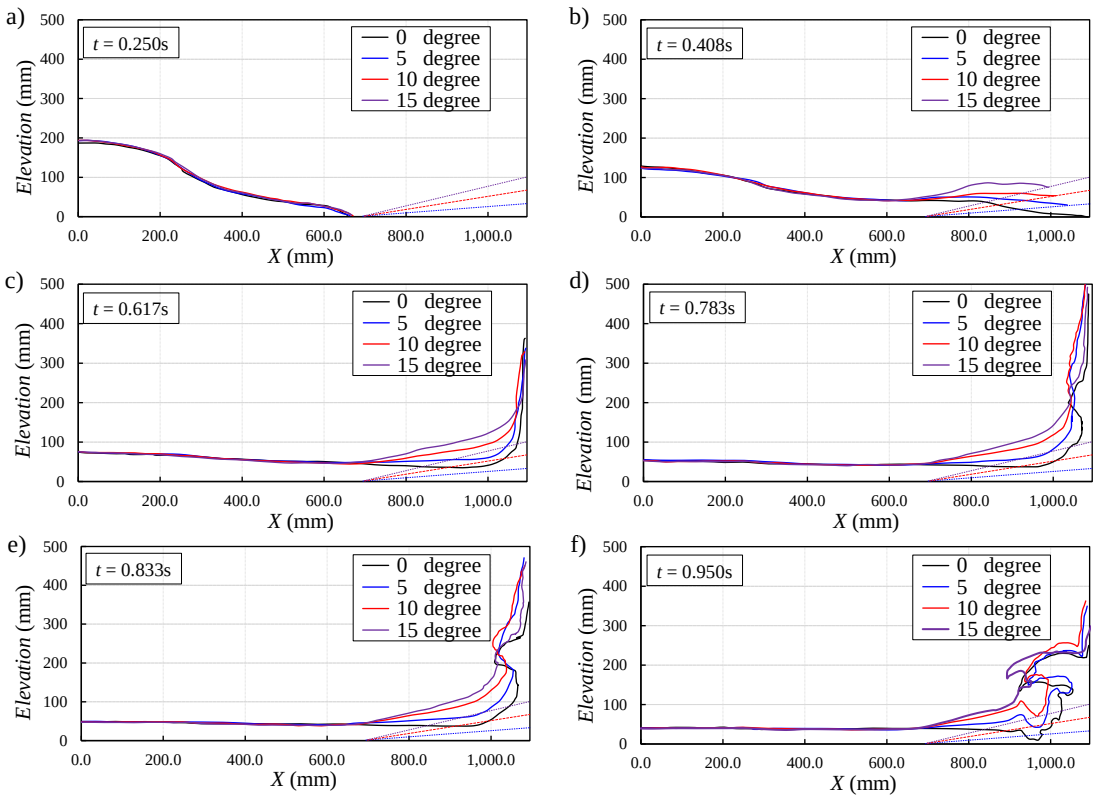

Figure 5.3 Comparison of digitized free surface profiles at t = 0.250 s, 0.408 s, 0.617 s, 0.783 s, 0.833 s, 0.950 s

The waves propagated in same pace and kept identical shapes before arriving on the slope at X = 0.7 m, as shown in Figure 5.2 (a) and Figure 5.3 (a) at t = 0.250 s. In the subsequent time instances, it can be observed that the slope slowed down the wave propagation, i.e., at t = 0.405 s in the horizontal case, the wave front arrived against the right wall then initial impacting occurred. However, there was still a short but visible space between the wavefront and the right wall in the inclined cases, as shown in Figure 5.2 (b) and Figure 5.3 (b). During the propagation over the slope, flow depth was similar in magnitude in all cases, as shown in Figure 5.2 (c) (d) (e), but water depth increased as the slope increased, which can be observed in the corresponding Figure 5.3 (c) (d) (e). When slope increased, runup velocity slowed, which resulted in a thicker

and larger water body below h = 200 mm, as shown in Figure 5.2 (d) (e) and Figure 5.3 (d)(e). The runup wave above h = 200 mm also became thicker with slope increasing in the 5 - and 10 - degree cases. However, a thinner runup wave was observed in 15-degree case, which is between the 5 - degree and horizontal case, as shown in Figure 5.3 (d)(e). A reasonable explanation was made that the slope deceleration effects became more significant for the case of the 15-degree, which lead to much less runup wave. Figure 5.2 (c) and Figure 5.3 (c) illustrated that the runup height was difficult to be compared visually because the wave top became extremely thin and splashed, similar with the splash-up phenomenon described in experimental work by Shen et al., (2020). The entire wave runup height was recorded successfully by the ultrasonic wave gauge sensor, which was introduced and discussed in the following section.

Meanwhile, the wave turned back earlier and curlier in the horizontal case when compared with the inclined cases, which indicated that the slope reduced the velocity of the rotating wave. During the period from the wave arriving on the slope to breaking, it was observed that the wave shape remained the same on the horizontal bed before the slope, which started from X = 70 cm, as shown in Figure 5.3 (c) (d) (e). In the follow-up stage, the rotating return wave hit the water's surface and started breaking, accompanied by a bounced splashing wave in the horizontal case and 5-degree case. However, the rotating back wave propagated diagonally down to the bed for the larger as show in Figure 5.2 (g)(h). The last raw image of wave breaking revealed that the rotating-back wave propagated faster in the horizontal case. As shown in Figure 5.2 (h), the wave front reached the left (reservoir) wall in the horizontal case at t = 1.367 s, while a lagging distance of approximately 15 cm was observed in the inclined cases.

5.4.2 Wave runup height

When the wave impacted the right wall and continued its runup, the top layer became very thin and splashed at highly along the wall. Thus, the wave profile became difficult to visually compare or digitally sketch, as shown in Figure 5.2 (c) (d) and Figure 5.3 (c)(d). The time history of wave runup height on the right wall was then successfully recorded by ultra-sonic transducer, together with the non-dimensional ratio to the initial impoundment depth h_0 illustrated in Figure 5.4. In all cases, the wave height instantly increased upon initial impacting, then recached a maximum value at approximately 0.85 s, which was 523.09 mm, 508.3 mm, 475.06 mm and 451.17 mm for the horizontal, 5 -, 10 - and 15 - degree cases, respectively, with a respective ratio of 2.09, 2.03, 1.90 and 1.80 to the initial impoundment depth, h0. As shown in Figure 5.4, the runup wave started running up the right wall slightly later, but overturned earlier for the sloped cases when compared with the horizontal case. The slower wave runup and shorter adherence to the right wall observed in the case of the slopes revealed that slope may help reduce wave overtopping on coastal revetments, for instance.

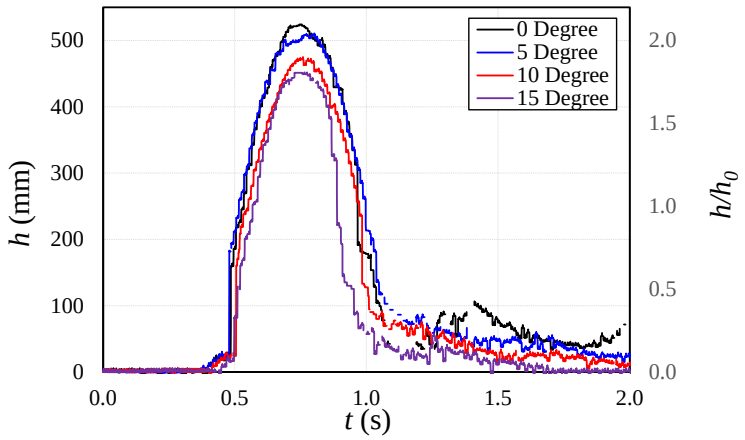

Figure 5.4 Wave runup height on the downstream right wall

After wave overturning and falling back down at approximately 0.85 s, the flow propagated away from the slope and right wall in the inclined cases, as Figure 5.2 (g) (h) shows. In the period from 1.1 s to 2.0 s, the wave height on the right wall decreased with an increase in the slope increasing, i.e., approaching zero since t = 1.6 s in the 15 - degree slope, as shown in Figure 5.4 in purple line. It was observed that the amount of water remaining on the slope continued to decrease after the wave fell back onto the advancing flow. In other words, the slope can reduce the inundation extent and depth in coastal after the first tsunami attack. Moreover, there was a small secondary peak around 1.4 s on the time history wave height in the horizontal case, as the black curve shows in Figure 5.4, which meant that the flow impacted on the bed and splashed.

5.4.3 Wave front location and velocity

Due to the deceleration effects of the slope, the dam break wave propagated more slowly on the sloped bed section when compared with the horizontal case, as visually observed in Figure 5.2 (b) and Figure 5.3 (b). The averaged wave front location from the extracted images was digitally processed and presented in Figure 5.5.

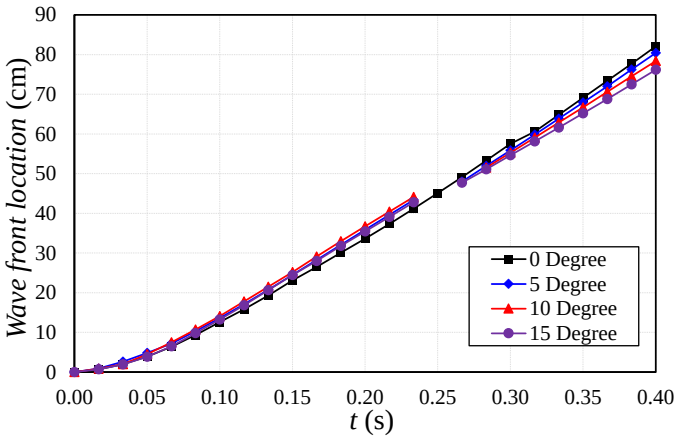

Figure 5.5 Time history of the wave front location

It can be observed that, the wave from all the four cases propagated at same distance during the period from t = 0.0s to arriving at the slope toe at t = 0.25 s, as the highly matched wave front location curves before 0.25 s shows in Figure 5.5. During 0.24 s to 0.26 s, several data points were lost in the inclined case as splashing occurred when the wavefront began hitting and running up the slope, which resulted in uncertainty in confirming the location of the wave front. After this short unsteady moment, the wave propagated stably along the slope, and the wave front location could be clearly identified and measured. As illustrated in Figure 5.6, the wave front location after t = 0.26 s clearly demonstrated that the slope decelerated the wave propagation.

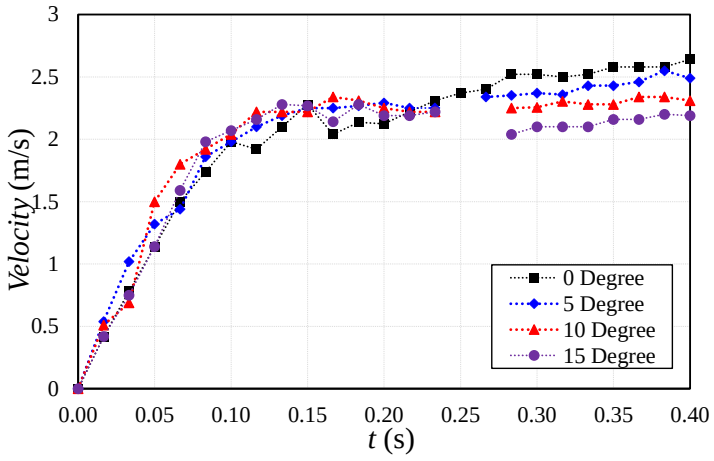

Figure 5.6 Time history of the average wave front velocity

The deceleration effect became stronger when the slope increased, as indicated by the tiny but steady differences between the curves of horizontal and sloped cases. The tests in this paper were conducted in a relatively short tank, so differences in wave front location caused by the presence of the slope would be more obvious if one would use a longer tank.

Based on the wave front location data, the averaged velocity was differentially calculated and presented in Figure 5.6. Consistent with the wave front location curves in Figure 5.5, the averaged velocities from the horizontal, 5 -, 10 - and 15 - degree slopes were close to each other prior to them arriving at the slope toe at time instant of approximately t = 0.25 s. Despite several missing data points due to the uncertainty of the wave front location caused by wave splashing, relatively stable average velocity was observed when the waves were propagating over the slope bed section during 0.3 s to 0.4 s, with averaged values of 2.57 m/s, 2.45 m/s, 2.32 m/s and 2.17 m/s in the horizontal, 5 -, 10 - and 15 - degree cases, respectively. The deceleration effect of slope on wave propagation was clearly reflected in the velocity data in the inclined cases: 4.7%, 9.7%, and 15.6% lower than the value in horizontal case with increasing order of slope. The velocity differences could be more obvious and larger had the slope been longer. In other words, a steeper beach slope would slow down the propagation velocity of tsunami inundation wave over the coastal area.

5.5 Discussion

The experiments presented in this study were intended to investigate slope effects on the kinematics of dam-break waves. The results revealed that slope affects the wave propagation shape, runup height on the impinged structure, the movement of the wave front location and velocity. Compared with the free surface study in previous experimental research (Lobovsky et al., 2014; Ozmen-Cagatay et al., 2010) to investigate the characteristics of tsunami-like waves, this study also revealed the influence of different slopes on wave propagation, on the characteristics of free surface profile, wave runup height, wave rotation and breaking.

The wave front location and velocity field components were obtained by digitally processing raw images recorded by the camera. The maximum wave front velocity in the horizontal case was 2.57 m/s, close to the numerically simulated result of Yang et al., (2018b), which was 2.7 m/s. The maximum wave front velocity in this paper and the research by Yang et al., (2018b) were both smaller than the analytical solution by (Ritter 1892), $1.64\sqrt{gh_0}$ and $1.72\sqrt{gh_0}$ when compared with $2\sqrt{gh_0}$. A reasonable explanation may be that the bed resistance was not considered in the analytical solution by Ritter (1892), and thus his formular returns a higher velocity. In the case of the sloped beach, the maximum averaged velocities were $1.56\sqrt{gh_0}$, $1.48\sqrt{gh_0}$, $1.39\sqrt{gh_0}$, for slopes of 5, 10 and 15 degrees, respectively. It should be noted that the ratios of the maximum averaged velocity to $\sqrt{gh_0}$ in the sloped beach cases were not constant as the values were highly related to the length of the horizontal bed section.

However, there were some limitations in the present study. Raw images were extracted from a recorded video of only 60 fps, which was not sufficient enough to collect the full image of flow changes. Some details of the dramatic wave development and breaking were difficult to capture; this could be improved by using a higher frequency high-speed camera. In this study, experiments were set up in a relatively short tank to investigate the slope effects. The slope effects were analyzed both qualitatively regarding free surface profile and quantitatively in terms of digitized water surface, wave runup height, location and velocity of wave front. The differences between each case revealed that the kinematic behaviors of the flow will change with varied slopes. For being able to propose practical advice and guidance with respect to flow

kinematics of the dam break waves, considering different bed lengths, the ratio of horizontal and sloped beds, bed roughness would be useful.

5.6 Conclusion

In this study, slope effects on the propagation of dam break waves were experimentally investigated by installing several inclined beds in a glass tank. The kinematic characteristics of dam break flow, including free surface profiles, wave runup height, the location and velocity of wave front were studied and compared. The conclusions were summarized as follows:

- The free surface profiles study demonstrated that during the dam break wave propagation until breaking, the wave shape remained the same over the horizontal bed section, and only changed as the wave propagated over different beach slopes.
- Higher wave runup height and longer runup along the right wall were observed in the horizontal case compared to the bore propagating over the inclined cases. In the stages of the wave overturn and fall down onto the incoming flow, slope caused the wave to plunge downward toward the bed; additionally, lower splashing height of the breaking wave was observed in the sloped cases.
- The study also revealed that slope decelerated the wave propagation in terms of the wave front location and velocity.

5.7 Appendix: Numerical simulation of the kinematics of dam-break wave

In this section, parts of the experiments in the above sections were reproduced via numerical models using OpenFOAM and DualSPHysics for comparison, with 4 mm mesh grids

and 2 million particles, respectively. The comparison results of free surface profiles from the 15 - degree case, and wave front velocity from the horizontal case, were presented and discussed.

5.7.1 Free surface profile

The 15 - degree case was selected for the free surface profile study, due to the deepest slope which caused complex wave development. The experimental free surface profiles at different time instances, and the numerical results using OpenFOAM and DualSPHysics were compared and presented in Figure 5.7.

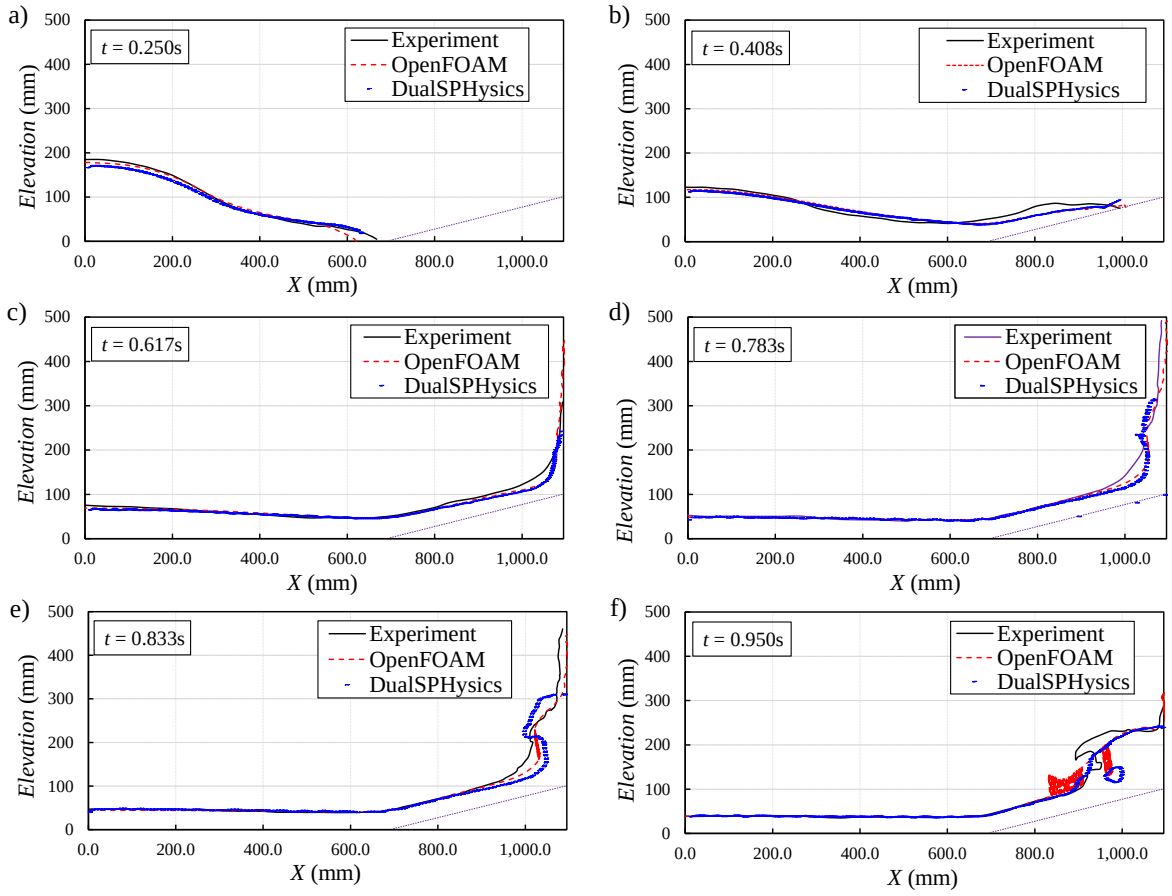

Figure 5.7 Free surface profiles from experiments, OpenFOAM and DualSPHysics

At the earlier wave propagation stage, the wave front location in the experiment was located slightly further than the results by OpenFOAM and DaulSPHysics, as shown in Figure 5.7. When the wave approached close to the right wall at t = 0.408 s, perfect agreement was observed between the free surface profiles from the experiment and the numerical results, except the slightly convex curve in the wave tip region. During the wave runup stage, the free surface profiles matched well over the horizontal bed and the slope until X = 1000 mm, as exhibited in Figure 5.7 (c) and (d). Discrepancies were observed in the free surface profiles close to the right wall, where the numerical results in OpenFOAM were closer to the experiments, as well as in the flowing wave falling stage in Figure 5.7 (e). However, the rotating back wave shape was clearer in the results by DualSPHysics at t = 0.833 s. In the last free surface profile where the wave started breaking, the results of OpenFOAM and DualSPHysics overlapped well, and the 'cavity' was clearly captured only by DualSPHysics. Meanwhile, the wave started breaking in OpenFOAM, as the small group of red curves in Figure 5.7 (f) shows.

Overall, OpenFOAM and DualSPHysics can accurately simulate the propagation of dam-break wave, as indicated by the good agreement in Figure 5.7. The discrepancies were generally located in the wave front area, and the region close to the right wall, especially after the wave impacted on the right wall and the following stages.

5.7.2 Wave front location and velocity

The numerical wave front velocity was calculated in OpenFOAM and DualSPHysics based on the simulation techniques in section 2.5. A comparison of the wave front velocities in the horizontal case from the experiment and numerical simulation by OpenFOAM and DualSPHysics was presented in Figure 5.8.

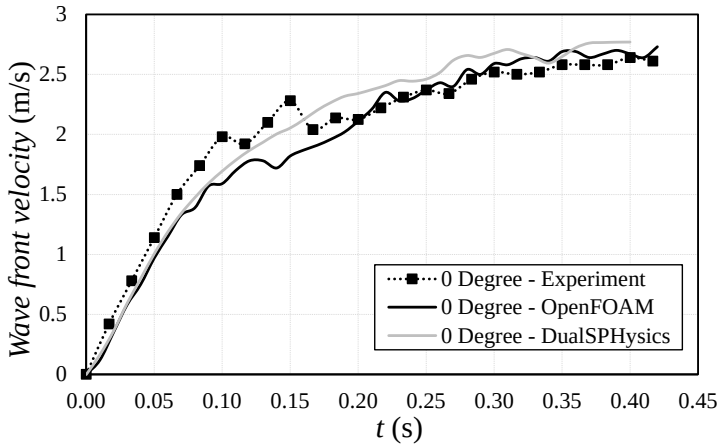

Figure 5.8 Comparison of wave front velocity values from the experiment, OpenFOAM and DualSPHysics

It was observed that the wave propagated faster in the experiment at the earlier stage until t = 0.15 s. Then the wave simulated by DualSPHysics developed faster until impacting on the right wall around t = 0.40 s. The velocities from the experiment and OpenFOAM matched better from t = 0.20s to t = 0.40s. In the relatively steady stage from t = 0.3 s, the averaged wave front velocity from the experiment was 2.57 m/s, close to the velocity of 2.65 m/s by OpenFOAM, lower than the velocity by DualSPHysics, which was 2.71 m/s.

The good agreement in the wave front velocity comparison revealed that both OpenFOAM and DualSPHysics can predict the wave propagation well. The differences between the experimental results and numerical simulation may be caused by the experimental measurement and numerical simulation techniques, which could be investigated and improved to provide better results in the future.

Chapter 6 Experimental and Numerical Investigation of Beach Slope Effects on the Hydrodynamic Loading of Tsunami-like Surges on a Vertical Wall

Abstract

Over the past decades, Over the past decades, hydraulic surge generated by dam-break waves has been used to simulate the effects of tsunamis on coastal infrastructure. This study investigates the slope effects on hydrodynamic loading of dam-break waves on structure when propagating over four different inclined beds (0−, 5−, 10−, 15−degree) by experiment and numerical simulation using OpenFOAM and DualSPHysics. Except for small discrepancies in the pressure time-history, numerical results obtained with both OpenFOAM and DualSPHysics agreed closely with the experimental dynamic pressures. The results revealed that the hydrodynamic pressure decreased after an initial impact peak from the lowest transducers in the 5−, 10−, and 15−degree cases when compared with the horizontal case. However, the dynamic pressure of transducers at same corresponding level increased with an increase in the slope. The integrated experimental hydrodynamic forces were similar to the numerical results for the 0− and 5−degree cases, while they were higher for the 10− and 15−degree cases due to insufficient pressure data. By investigating the relation between the force decrease and slopes, a non−dimensional reduction factor was proposed from the linear fitness for slope effects estimation. This experimental and numerical study can provide novel insight on the hydrodynamic force calculation of tsunami-like surges on coastal infrastructures when considering beach slope.

Keywords: Tsunami, hydraulic surge, beach slope, hydrodynamic loading, pressure transducer, OpenFOAM, DualSPHysics

6.1 Introduction

Since Lauber et al., (1998) summarized and concluded the experimental criteria for generating ideal dam break waves, the latter have been widely used to investigate the mechanism of tsunami overland inundation, which, over the past decades have caused significant disasters in coastal areas around the world. Extensive research on dam break wave propagation over horizontal beds and the subsequent hydrodynamic impact on structures has been performed by several researcher (Nouri et al., 2010; St-Germain et al., 2012; Lobovsky et al., 2014; Kleefsman et al., 2005; Zhou et al., 1999; Wuthrich et al., 2018b; Hu et al., 2010; Lee et al., 2002; Lu et al., 2018).

One of the major aspects to be investigated and which is related to the hydrodynamics of dam break waves is the dynamic pressure during the impact of these waves and structures located in their path. In the highly cited experimental research by Lee et al., (2002), the time-history data of hydrodynamic loading of a dam break wave propagating over a horizontal bed and its impact on a tank wall was recorded by several wall mounted pressure transducers. Reasonable agreement was observed between the experimental pressure and numerical results, despite some discrepancies around the peak value. This experimental apparatus was scaled up and reconducted by Lobovsky et al., (2014) to provide detailed insights in the form of a statistical analysis with the application of miniaturized pressure transducers. Except for a good agreement between the time-history of the experimental and numerical pressures (Lee et al., 2002), there were discrepancies that may be introduced by the use of larger-diameter pressure

transducers. Overall agreement was observed in the comparison with experimental research by Kleefsman et al., (2005) and Wemmenhove et al., (2010). In the study by Nouri et al., (2010), the time variation and the vertical distribution of dynamic pressure from a dam break wave onto a cylindrical structure was presented and analyzed. Spatial distribution of the time history of the hydrodynamic pressure was shown to be significantly different from the triangular hydrostatic distribution. Spatial distribution of dynamic pressure can provide detailed insights into the characteristics of dam break flow for important time instances (Shen et al., 2020; Kihara et al., 2015).Experimental test demonstrated that pressure transducers were capable of recording the time variation of the dynamic pressure on structures caused by dam break waves.

Compared with the investigation of dynamic pressure fields, the experimental estimation of the force study is a more direct way of evaluating the hydrodynamic loading of dam break waves and has the potential to provide design guidance for coastal infrastructures. With the installation of a 6 degrees of freedom dynamometer at the bottom of a cylindrical column, Nouri et al., (2010) obtained the time history of the total force exerted on a circular and square structure due to the surge generated by the reservoir with impoundment depths of 0.5 mm, 0.75 m, 0.85 m and 1.0 m. The experimental study demonstrated that surge force overshot the hydrodynamic force when the impoundment depth increased; this was attributed to the steeper slope and fast moving surge front. Wuthrich et al., (2018b) conducted a series of experiments to study the hydrodynamic impact of tsunami-like waves against impervious free-standing buildings by installing a force plate at the bottom of the partially channel-blocking cubic model. Unlike the previously observed gradually decreasing force, after the initial peak value at initial impact of a slender structure, a relatively quasi-steady period (fluctuating around 150 N) was observed

during the impact stage from 5 s - 35 s for the case of the dry bed. In the research on the spatiotemporal characteristics of dam break -induced loading on a vertical wall by Shen et al., (2020), the interaction process was described as having 3 stages: the initial impact stage from impact to the highest wave run-up; the reflected stage until the wave fell back and rotated; followed finally by the second impact stage. The study revealed that the surge force mainly came from the bottom impact zone during initial impact stage and second impact stage, whereas it was contributed to by both the bottom impact zone and upper outer zone during the reflected stage. Recently, Farvizi et al., (2021) placed a load cell in the bottom of a pier to quantify the tsunami-induced force on a deck girder section bridge. The force comparison for the 0-degree bed case indicated that the impact horizontal force acting on the pier was mainly caused by the hydrodynamic loading, and to a lesser extent, by the hydrostatic one.

Besides the experimental measurement approach, empirical formulas have been proposed to directly estimate the impact force of tsunami waves on coastal infrastructure. In the widely used Japanese Structural Design Guideline (SMBTR) (Okada et al., 2005c) which is based on the research by Asakura et al., (2000) and Okada et al., (2005b), the maximum pressure was set as three times the hydrostatic pressure and also three times the maximum wave height linearly distributed on the front face of the wall, as indicated in Figure 6.1.

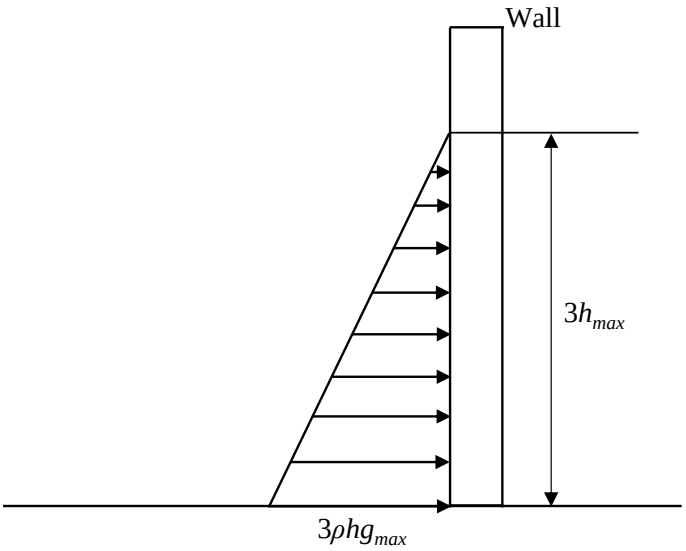

Figure 6.1 Tsunami force calculation method in SMBTR.

Thus, the unit horizontal impact force (N/m) was nine times that of the hydrostatic force, a provision which was also adopted by *City and County of Honolulu building code (CCH)* 2000), as described in Eq. (6.1):

$$F_{x,\max} = \frac{1}{2}\rho g(3h_{\max})(3h_{\max}) = 9(\frac{1}{2}\rho g h_{\max}^2) \tag{6.1}$$

where, ρ is the water density, g is the gravitational acceleration, $h_{\max}$ is the maximum wave height. In the research by Okada et al., (2005b), $h_{\max}$ was defined as the maximum wave elevation measured from the ground up while the wave freely developed. As the dam break wave was completely stopped by the vertical wall in this study, $h_{\max}$ was defined as the maximum wave height while the wave started impacting on the right wall, i.e., the wave height at the left wall, approximately 0.13 m in horizontal case.

The calculation of hydrodynamic load by tsunamis on structures was also presented in ACSE - 7, Chapter 6. The provisions of this standard were applied in the tsunami loads studies

by Stolle et al., (2018) and Wuthrich et al., (2019a). In this study, equation 6.10(4) from the latest version of ASCE - 7 (ASCE 2022) was adopted for the unit hydrodynamic loading calculation, as shown in Eq.(6.2):

$$F = \frac{1}{2}\rho_s I_{tsu} C_d (h_e u^2) \tag{6.2}$$

where, ρ_s is the water density, I_{tsu} is the importance factor which is 1.25, C_d is the drag coefficient which is 2.0 when the wall is normal to flow, h_e is the inundation depth taken as 2/3 of the maximum inundation depth which is 0.07 m, and u is the maximum velocity of tsunamic flow in the steady propagation stage before impacting the right wall, which is around 2.9 m/s, calculated by the analysis method in the study of Liu et al., (2022a).

To obtain detailed values of the time-history of the hydrodynamic force, numerical modelling was used to elucidate the interaction between infrastructure and tsunami-like inundation. The open-source software OpenFOAM has been widely and successfully applied to solve fluid dynamics problems due to its customised solvers and various models (Sánchez-Cordero et al., 2017; Xie et al., 2019; Nguyen et al., 2020; Larocque et al., 2013; Evtushok et al., 2021). By applying OpenFOAM, Sánchez-Cordero et al., (2017) numerically reproduced the physical test of a dam break wave impacting an obstacle (Kleefsman et al., 2005). The qualitative analysis showed that numerical results highly matched with the experimental dynamic pressure of certain points on the frontal face, except for tiny temporal variations. Peng et al., (2021) performed numerical simulations to investigate the impact of dam break induced flooding on a structure by reproducing the physical test of (Lobovsky et al., 2014) in OpenFOAM. The comparison study between the numerical results and experimental data showed that numerical

models can reasonably predict the experimental dynamic pressure exerted onto a structure caused by dam-break flow. Furthermore, this study revealed that the dynamic pressure approached zero at a level equal to the initial impoundment depth on the structure wall, which can provide evidence for the pressure distribution study.

The Smoothed Particle Hydrodynamics (SPH) Method has been increasingly used to deal with large deformations of free surface flows and the complex interactions between waves and structures (Gomez-Gesteira et al., 2012a; Ming et al., 2018). This is mainly due to its benefits, which include being meshfree, and adaptive (Lind et al., 2020). The experiment dealing with the dam break flow impacting a column (Nouri et al., 2010) was reproduced using SPHysics by St-Germain et al., (2012) who numerically investigated the hydrodynamic loadings of tsunami-induced waves on onshore structures. Except for a very high simulated peak pressure at the lowest transducer calculated using SPHysics and which was attributed to trapped air, the numerically obtained dynamic pressures by SPHysics matched well the experimental results for the 1.15 m impoundment depth case. Good agreement was also observed for the force comparison from the initial impact to the high wave runup on the column around 4.0 s (St-Germain et al., 2012; 2014). Then, due to the wave breaking and induced strong turbulence and air entrainment, the oscillations observed on the experimental force time-history increased with the impoundment depth. In the most recently released DualSPHysics (Crespo et al., 2015a), the dynamic pressure can be calculated more accurately and stably (English et al., 2021) due to the advantage of a new boundary treatment method (English et al., 2019) built in to avoid the oscillation on the pressure field.

By reviewing the existing research and literature, it was found that most of the dam break research focuses on the hydraulic surge propagating over horizontal beds and the subsequent impact on structures. However, beaches along the coastlines are usually sloped in a range of 1:100 to 1:10-degrees or sometimes more. Therefore, in such situations the hydrodynamic loading of dam break flow will change and it should be investigated. In addition, to record the hydrodynamic pressure, the pressure transducers were mostly installed up to a limited height, i.e., below the level of the initial impoundment depth *H*. However, the wave runup can rise up to two times the height of *H*. The distribution of dynamic pressure at higher elevation on the wall is hence of significant research interest. Additionally, in most cases, dynamometers and force load cells were installed at the bottom of structures to measure the impact loading; however, this can be difficult to be applied to the built large-scale structures for monitoring work. Furthermore, the recorded impact force on isolated structural elements (such as columns) exhibited a peak value at the instant of the initial impact which then further decreased gradually, and, later on, exhibited a relatively quasi-steady hydrodynamic forces was observed. However, less attention was paid to the trend of impact force on fully flow blocking structures during the complex wave-structure interaction. Additionally, there is lack of non-dimensional study about the hydrodynamic loading for dam-break research.

This study aimed to investigate slope effects on the hydrodynamic loading caused by tsunami-like dam break flows on vertical walls in terms of the measured dynamic pressure and impact, total force. Numerical models were developed using OpenFOAM and DualSPHysics model. They were used to reproduce the experiments and provide a comparison with experimental data. In addition, this study offers a new perspective on the spatial distribution of

impact pressure generated by dam break flows by also investigating the elevation of the maximum runup where the pressure became nil. The force integration method the presentation of the non−dimensional reduction factor can provide a simple approach for quantifying the impact force by using the information provided from the pressure transducers with consideration of the slope effects.

The paper is organized as follows: the Introduction section is followed by the experimental apparatus design and settings. Section 3 focuses on the posting−processing methodology of experimental data and the numerical simulation used to reproduce the physical tests. The results are then analyzed and discussed in Section 4 in terms of dynamic pressure and integrated hydrodynamic force. The discussion is presented in Section 5. Finally, conclusions are presented in Section 6.

6.2 Experimental settings

To physically investigate the effects of slope on the hydrodynamic loading of a tsunami-like bore acting on a wall, dam break experiments with an impoundment depth H = 300 mm were conducted at the Water Resources Engineering Laboratory at the University of Ottawa, Canada. The experimental facilities, included a 1.2 m long, 0.44 m wide, 0.5 m high glass tank with gate release system, pressure transducers and data acquisition system Liu et al., (2022b) to investigate the dynamics of dam-break surges on a horizontal bed, as shown in Figure 6.2.

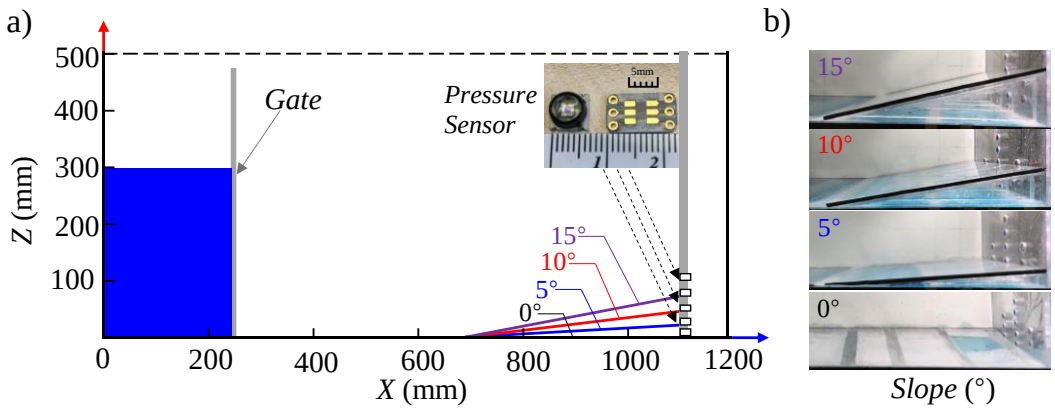

Figure 6.2 Experimental setup: (a) apparatus system with side wall equipped with Honeywell Pressure Transducers (HPTs); (b) locations of HPTs and the 4 bed slopes employed: 0 - degree, 5 - degree, 10 - degree, 15 - degree.

Honeywell Pressure Transducers (HPT, TBFLPNS001BGUCV, Honeywell Sensing and Productivity Solutions, Charlotte, USA) were mounted along the vertical centre line of the right wall, which were at altitudes of 3 mm, 35 mm, 70 mm, 105 mm and 140 mm, numbered as transducers 1 to 5. To model the inclined beach, 4 different slopes with 0 - degree (horizontal bed), 5 - degree, 10 - degree, 15 - degree, were built and installed starting at X = 0.7 m and leaning against the right wall at X = 1.1 m, as shown in Figure 6.2 (a) and (b). The top of the slope was designed to be located just below the lowest transducer in each case for peak impact pressure investigation and comparison, e.g., transducer 3 is the lowest transducer in the 10 - degree case. The number of transducers in each case and experimental matrix are listed in Table 6.1.

Table 6.1 Experimental Matrix

Case	Impoundment Depth	Measurement Devices
0-degree	300mm	5 HPTs
5-degree		4 HPTs
10-degree		3 HPTs
15-degree		2 HPTs

6.3 Experimental and numerical techniques

6.3.1 Experimental post-processing

The time-history of the dynamic pressure was measured by the HPTs to compare and investigate the slope effects. The vertical pressure spatial distribution was also integrated to calculate the impact force. In the numerical investigation by Peng et al., (2021), the impact of dam-break induced flooding on the structure and the results of dynamic pressure on the wall demonstrated that the pressure values decreased to zero around the height of the initial impoundment depth. In addition, by setting virtual pressure probes above the top transducer 5 in the numerical simulation of this study, similar results were obtained; as soon as the runup wave reached an elevation above the initial impoundment depth, it became very thin and splashed instead of acting on the right wall when the runup was. Thus, a linear interpolation method was proposed to calculate the impact force, based on the assumption that dynamic pressure decreased to 0 when the runup reached the same elevation on the right wall as that of the initial impoundment depth h_0, as shown in Figure 6.3.

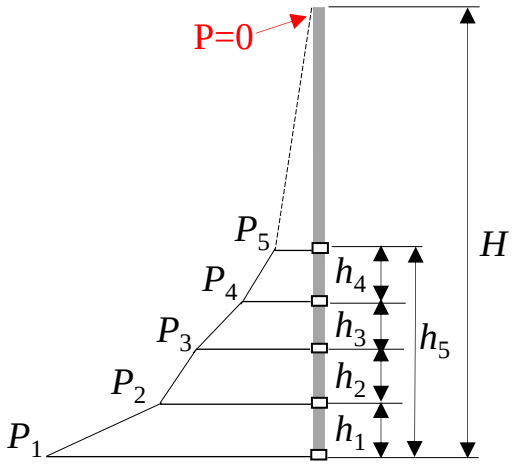

Figure 6.3 Schematic of the linear dynamic pressure distribution on the right wall with the assumption that P = 0 at the elevation equal to that of initial impoundment depth H, $h_1 = h_2 = h_3 = h_4 = 35$ mm, $H = 300$ mm.

The resultant unit force (N/m) was calculated using the formula below:

$$F = \sum_{i=n}^{4}\left[\frac{1}{2}\times(P_i + P_{i+1})\times 0.035m\right] + \frac{1}{2}\times P_5 \times (H - h_5) \tag{6.3}$$

where, P_i is the pressure of transducer i, $n = 1, 2, 3, 4$ for the 0 -, 5 -, 10 - and 15 - degree beach slope cases separately, H is the initial impoundment depth equal to 300 mm, and h_5 is the height of transducer 5 located at 140 mm above the origin of the system of coordinates.

6.3.2 Numerical modelling using OpenFOAM and DualSPHysics

To reproduce the physical tests results and to provide a comparison with them, one three-dimensional numerical model both based on open-source VOF based codes - OpenFOAM and SPH based package - DualSPHysics were developed and modified, respectively. For both numerical models, the computational domain was configured to have the same dimensions as the experimental apparatus. The rigid tank walls and bottom were set as no-slip boundary condition,

while the top boundary was set open with constant atmospheric pressure. Virtual pressure probes were coded in the numerical model at the corresponding locations with the pressure transducers in the physical tests.

In OpenFOAM simulation, the two-equation $k-\omega$ *SST* (Shear Stress Transport) turbulence model (Menter 1994) were applied as this model combines the advantages of the $k-\varepsilon$ turbulence model in free flow and the $k-\omega$ turbulence model in the boundary layer. Thus, this combined turbulence model was successfully used in a wide range of applications (Lopez-Jimenez et al., 2015; Romanova et al., 2022), especially in the study of multi-phase flow (Nguyen et al., 2020). The governing equations for turbulence kinematic energy k and specific turbulence dissipation ω are shown in Eq.(6.4) and (6.5).

$$\frac{\partial \rho k}{\partial t}+\frac{\partial \rho u_j k}{\partial x_j}=P_k-\beta^* \rho k\omega+\frac{\partial}{\partial x_j}\left[\left(\mu+\sigma_k \mu_t\right)\frac{\partial k}{\partial x_j}\right] \tag{6.4}$$

$$\frac{\partial \rho \omega}{\partial t}+\frac{\partial (\rho u_j \omega)}{\partial x_j}=\frac{\gamma}{\nu_t}-\beta \rho \omega^2+\frac{\partial}{\partial x_j}\left[(\mu+\sigma_\omega \mu_t)\frac{\partial \omega}{\partial x_j}\right]+2(1-F_1)\frac{\rho \sigma_{\omega 2}}{\omega}\frac{\partial k}{\partial x_j}\frac{\partial \omega}{\partial x_j} \tag{6.5}$$

where, the default empirical model coefficients $\left(\sigma_k, \sigma_\omega, \gamma, \beta\right)$ are represented by constants ϕ, which can be calculated from the constants ϕ_1 and ϕ_2, as shown in Eq.(6.6):

$$\phi=F_1\phi_1+(1-F_1)\phi_2 \tag{6.6}$$

where, F_1 is the blending function, thus the coefficients $\left(\sigma_k, \sigma_\omega, \gamma, \beta\right)$ adopted in the numerical model are given in two sets according to ϕ_1 and ϕ_2, as indicated in Eq.(6.7):

$$\sigma_{k1} = 0.85, \sigma_{\omega 1} = 0.5, \gamma_1 = \beta_1 / \beta^* - \sigma_{\omega 1}\kappa^2 / \sqrt{\beta^*}, \beta_1 = 0.075$$
$$\sigma_{k2} = 1.0, \sigma_{\omega 2} = 0.856, \gamma_2 = \beta_1 / \beta^* - \sigma_{\omega 2}\kappa^2 / \sqrt{\beta^*}, \beta_2 = 0.0828 \quad (6.7)$$
$$\beta^* = 0.09, \kappa = 0.41$$

In post-processing the results of the numerical model, numerical *pressure probes* were located at the same corresponding position of physical HPTs to capture the calculated dynamic pressure. The horizontal component of dynamic pressure thus could be extracted from the pressure field, which is calculated by Eq.(6.8).

$$p_t = p_{ref} + p + 0.5\rho|u|^2 \quad (6.8)$$

where, p_t is the total pressure, p_{ref} is the reference pressure, p is the static pressure, ρ is the water density, and u is the flow velocity.

The *force* library was used in the simulation and called to calculate the resultant force acting on the defined patch (i.e., the tank right vertical wall), as indicated in Eq.(6.9). In the post-processing stage, the horizontal impact force component on the right wall was obtained from the calculated results.

$$F = \sum_i \rho_i \overrightarrow{S_{f,i}}(p_i - p_{ref}) \quad (6.9)$$

where, i represents the number of the cells in the computation area, ρ is water density, $\vec{S}$ is the face area vector, p is the pressure and p_{ref} is the reference pressure.

In SPH method, the fluid domain is represented by a collection of individual particles and can thus be discretized (Monaghan 1994). With the application of discrete interpolation and kernel approximation, the governing Navier-Stokes equations are reformulated as shown in Eq.(6.10) and (6.11).

$$\frac{d\rho_i}{dt} = \sum_{j=1}^{N} m_j u_j \bullet \nabla_i W_{ij} \tag{6.10}$$

$$\frac{du_i}{dt} = -\sum_{j=1}^{N} m_j \left(\frac{p_i}{\rho_i^2} + \frac{p_j}{\rho_j^2} + \Pi_{ij}\right) \nabla_i W_{ij} + g \tag{6.11}$$

where, ρ_i, u_i, p_i are the density, velocity and pressure of particle i, respectively, m_j, ρ_j are the mass and density of neighbouring particle j, ∇ is the gradient operator, W_{ij} is the kernel function, and Π_{ij} represents the artificial viscosity term.

In DualSPHysics numerical model , for a given location, the pressure can be computed by using the pressure values at the neighbouring fluid particles, as shown in Eq.(6.12).

$$P_i = \frac{\sum_j P_j W_{ij}}{\sum_j W_{ij}} \tag{6.12}$$

where, P_i is the pressure at a given location, P_j is the pressure of neighbouring particles, and W_{ij} is the kernel function.

For boundary particles, acceleration can be numerically computed by solving the particle interactions with the neighbouring fluid particles, as shown in Eq.(6.13).

$$\frac{dv_i}{dt} = -\sum_j m_j \left(\frac{P_j}{\rho_j^2} + \frac{P_i}{\rho_i^2} + \Pi_{ij}\right) \nabla_i W_{ij} + g \tag{6.13}$$

where, v_i , P_i , ρ_i are the velocity, pressure and density of boundary particle i , respectively, m_j , P_j , ρ_j are the mass, pressure, density of the neighbouring particle j , respectively, W_{ij} is the kernel function, and g is gravitational acceleration.

Furthermore, by calculating the summation of forces on boundary particles, the resultant force acting on the boundary wall can be obtained, as shown in Eq.(6.14).

$$F = \sum_{i=1}^{N} m_i \frac{dv_i}{dt} \tag{6.14}$$

where, N is the number of particles in the computational area, m_i, v_i are the mass and velocity of boundary particle i, respectively.

A sensitivity and convergence study was conducted both in OpenFOAM and DualSPHysics, with different meshes and particle numbers employed in the calculation domain, separately. The sensitivity and convergence analysis results for the pressure calculated at transducer 1 are shown in Figure 6.4.

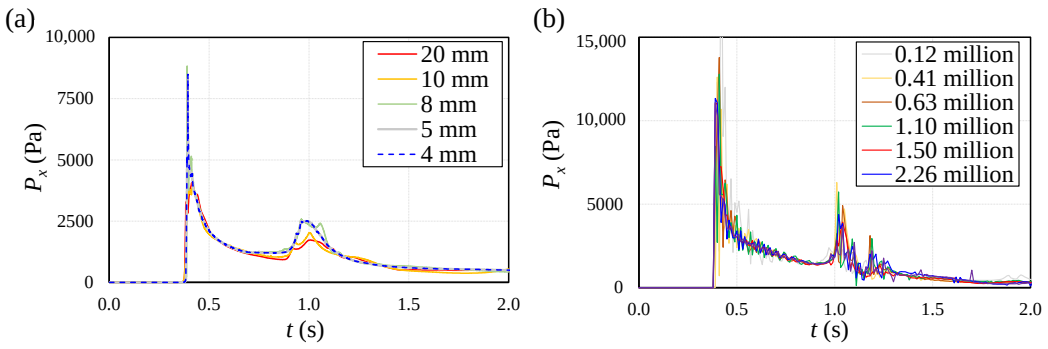

Figure 6.4 Numerical sensitivity study of the dynamic pressure for transducer 1 in: (a) OpenFOAM model (b) DualSPHysics model

In OpenFOAM simulations, different mesh grids of 20 mm, 10 mm, 8 mm, 5 mm and 4 mm were generated for the computational domain in all directions to investigate the convergence seperately. As indicated in Figure 6.4 (a), the first peak pressure tended to be steady and the pressure curves coincided more closely when the mesh size decreased from 20 mm to 4 mm. The

pressure data from models of 5 mm and 4 mm mesh grids were remarkably similar which indicated that convergent results were achieved. Thus, the mesh grid of 4 mm was adopted for the OpenFOAM simulation.

A high first peak pressure and following relatively larger oscillations were observed on the pressure time-history in DualSPHysics simulations with lower particle number, i.e., 0.12 million and 0.41 million, as shown in Figure 6.4 (b). With the particle number increasing, the first and second peak pressures got stabilized and the time-history curve became smoother with reduced tiny oscillations. A statistical analysis of the pressure values at first and second peak from Figure 6.4 (b) revealed that the peak values kept steady and approached convergence with a particle number over 1.50 million. Therefore, a particle number of approximately 2.2 million was applied to all the simulations in DualSPHysics.

6.4 Results

6.4.1 Dynamic pressure on horizontal bed

In the experimental study of dam break induced bore propagating over a horizontal bed (Liu et al., 2022b), the time-history of the impact dynamic pressure from the miniaturized transducers 1 - 5 were measured and these are presented in Figure 6.5. At initial impact, the pressure quickly reached a first peak value for all transducers except the slightly negative value recorded by transducer 5 due to suction effects caused by the fallback of the tip of the runup wave. After decreasing to a plateau period, a second peak pressure was observed due to the impact of the fallback wave. Afterwards, the time-history of pressure data gradually decreased to zero except for the approximate hydrostatic pressure recorded by transducer 1.

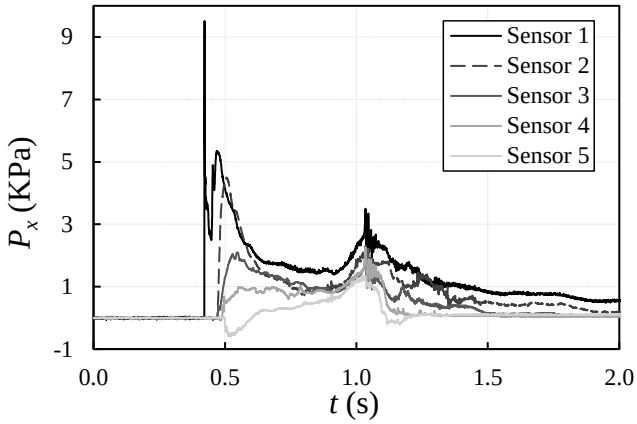

Figure 6.5 Time-history of the dynamic pressure of dam break flow on the tank wall by Liu et al., (2022b), bore generated by the 30 cm impoundment depth propagating on horizontal dry bed; transducers 1 to 5 located at elevations of 3 mm, 35 mm, 70 mm, 105 mm and 140 mm, respectively.

6.4.2 Pressure comparison of experiment and numerical simulation

In this study, the dam-break waves propagating over a horizontal bed was reproduced by two models, OpenFOAM and DualSPHysics, to numerically calculate the dynamic pressure at the corresponding transducer 1 - 5 locations, with the comparison presented in Figure 6.6. Good agreement was observed except for some slight discrepancies.

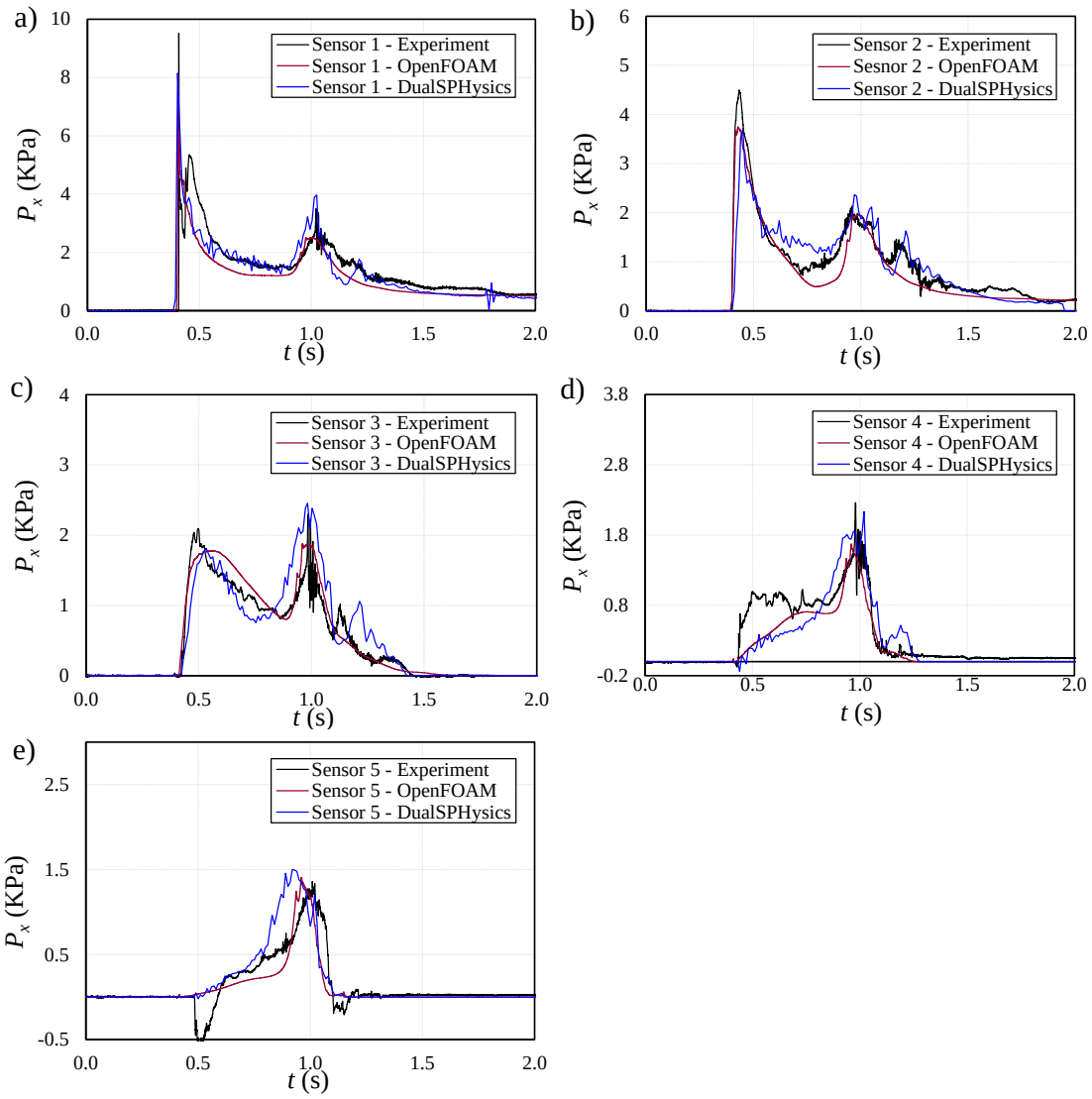

Figure 6.6 Time-history of the dynamic pressure - comparison of experimental data and numerical results obtained using the OpenFOAM and DualSPHysics models

The numerically calculated initial peak pressures at transducers 1 and 2 simulated by both the OpenFOAM and DualSPHysics models had approximately the same magnitude, i.e., approximately 1.26 kPa and 0.70 kPa, lower than the experimental value, respectively, as shown in Figure 6.6 (a), (b). Except for the pressure spike after the first peak for transducer 1 and the median pressure value during the plateau period between 0.6 s - 0.9 s for transducer 2, the

dynamic pressures recorded by transducers 1 and 2 fit well with the results computed by OpenFOAM and DualSPHysics. For transducer 3, in Figure 6.6 (c), it can be observed that the experimental dynamic pressure was closer to the experimental results obtained by OpenFOAM. The dynamic pressure calculated by DualSPHysics was 1.06 kPa lower at the first peak than the experiment and fluctuated in the range of 0.9 kPa during the plateau period between 0.7 s and 0.9 s. Meanwhile, the pressure duration around the second peak in DualSPHysics was approximately 0.15 s wider than the experiment and OpenFOAM. The experimental dynamic pressure of transducer 4 increased relatively sharply from the initial impact and then further fluctuated at approximately 0.8 kPa from 0.5 s - 0.8 s, which was not observed in the results of OpenFOAM and DualSPHysics. For transducer 4, both OpenFOAM and DualSPHysics demonstrated better agreement with experimental data. After 0.9 s, the time-history of the experimental and numerical pressures of transducer 4 matched well except the fluctuation observed in the pressure simulated by DualSPHysics. Neither OpenFOAM nor DualSPHysics exhibited the negative experimental pressure values at transducer 5. The dynamic pressure calculated by DualSPHysics matched well with the experimental data before 0.8 s; further, both the OpenFOAM and DualSPHysics models generated results closer to the experimental ones for the period from 0.9 s onwards, as exhibited in Figure 6.6 (e).

The duration of pressure crest around the second peak from experiment and numerical simulations matched perfectly for lower placed transducers 1 and 2. However, for transducers 3, 4, and 5, longer duration was observed for the time-histories of the pressure curves by DualSPHysics. OpenFOAM however demonstrated perfect match with experimental results in term of peak duration for the three top transducers (3, 4 and 5).

By comparing and evaluating the experimental dynamic pressure and numerical simulation results, it can be summarized that, except for some small discrepancies, both the OpenFOAM and DualSPHysics models can satisfactorily reproduce the impact of a dam break wave on a wall.

6.4.3 Dynamic pressure in lowest transducers

The dam-break experiments were conducted with different bed slopes, showing good repeatability in spite of data noises due to measurement errors which were filtered adequately, i.e., for the instantaneous and sudden small spike on the pressure time-history. During the impact between the right wall and dam-break induced bores, the lowest placed transducer will experience the most violent impacts. Figure 6.7 exhibits the time-history of dynamic pressure from the lowest placed transducers 1 which is located at the bottom in the 0 - degree case; transducers 2, 3, and 4 became the lowest placed ones for the 5 -, 10 -, and 15 - degree cases, respectively, as in the schematic showing the experimental apparatus in Figure 6.2.

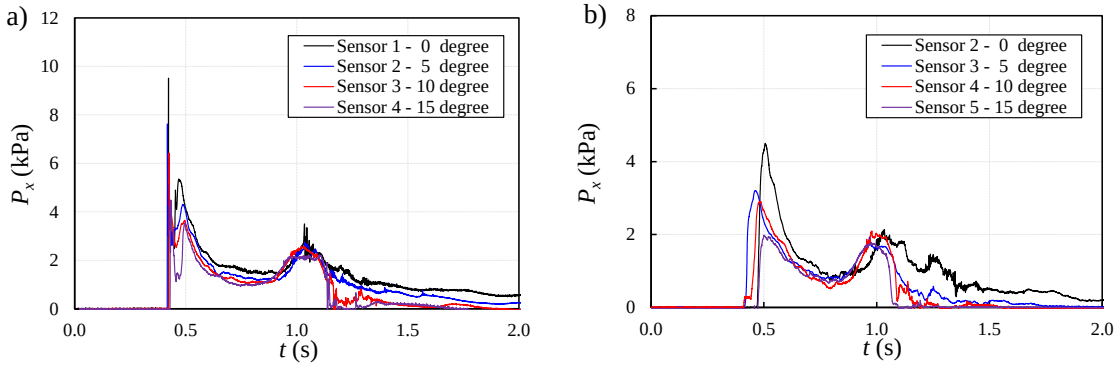

Figure 6.7 Time-history of the dynamic pressure recorded by the: (a) first transducer, (b) second transducer when counted from the bed in each slope case

Due to the slope effects, it can be observed that peak pressure at the initial impact from lowest transducers decreased when the slope increased, with peak value of 9.36 kPa, 7.62 kPa, 6.15 kPa, and 4.48 kPa in the horizontal, 5 -, 10 - and 15 - degree cases separately. For the inclined slopes, the initial impact time on the wall was slower than recorded the horizontal case and was delayed by 0.01 s, 0.017 s and 0.025 s in sequence. The pressure difference in the second spike after the first peak also decreased due to the slope effect, and dropped from 6.74 kPa in the horizontal bed case to 4.93 kPa, 3.623 kPa and 3.24 kPa in the 5 -, 10 -, and 15 - degree cases, respectively. During the relatively steady plateau period between 0.6 s - 0.9 s, the dynamic pressure from the horizontal bed case was slightly higher than that recorded for the inclined cases. However, for the second peak recorded around 1.05 s, when the runup wave was falling back onto the slope, the dynamic pressures for all slope cases were within a small range from each other, except for a few higher values in the horizontal case, with a difference around 0.6 kPa. After the second peak, the dynamic pressure gradually approached the value of the hydrostatic pressure of 0.43 kPa for the horizontal case and further decreased to a lesser value of 0.23 kPa for the 5 - degree slope. Meanwhile, the pressure value finally decreased to zero for the 10- and 15-degree slopes as no water remained on these two slopes.

The time-history of the dynamic pressure from the second lowest transducers, i.e., transducers 2, 3, 4 and 5 in the 0 -, 5 -, 10 -, and 15 - degree cases, respectively, are shown in Figure 6.7 (b). The pressure value reached its maximum at the initial impact, with 4.41 kPa in the horizontal bed case, 3.32 kPa, 2.79 kPa, and 1.98 kPa in the 5 -, 10 - and 15 - degree bed slope cases, in sequence. Although the slope deaccelerated the wave propagation, the arrival time of the first peak pressure at the second lowest transducer in the 5 - and 10 - degree case was 0.05 s

and 0.02 s shorter than that measured in horizontal bed case, respectively. The initial impact occurred at a similar time as the 15 - degree case, that is, around 0.5 s. Similar to the lowest transducers, the pressure values at the second peak were close to each other, varying in a small range from 1.93 kPa to 2.03 kPa. After the second peak, the pressure time-history of the horizontal bed case decreased gradually from 1.04 s to 1.45 s, then varied for some time around the hydrostatic pressure. However, the pressure for the cases of the inclined beds dropped quickly after the second peak, then approached zero until 2.0 s.

6.4.4 Dynamic pressure of transducers located at the same level

Due to the bed elevation, dynamic pressure from the transducers located at the same level with respect to the horizontal bed resulted in discrepancies both the horizontal and inclined cases, as shown in Figure 6.8.

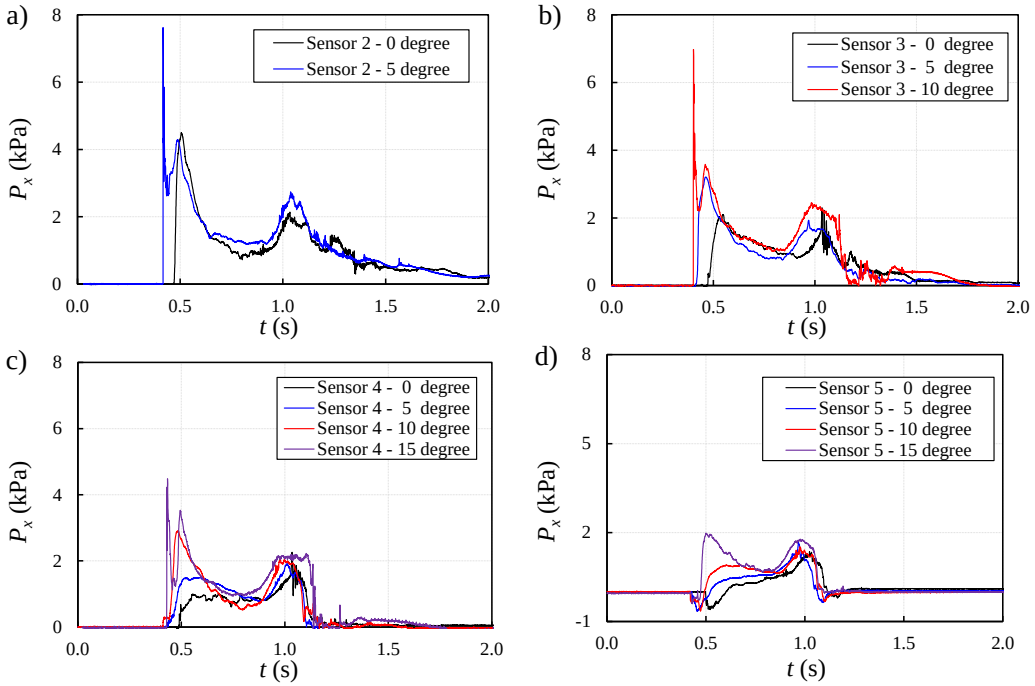

Figure 6.8 Time history of dynamic pressure from transducers located at the same level: (a) transducer 2 in 0- and 5-degree cases; (b) transducer 3 in 0 -, 5 - and 10 - degree cases; (c)

transducer 4 in 0 -, 5 -, 10 - and 15 - degree cases; (d) transducer 5 in 0 -, 5 -, 10 - and 15 - degree cases.

To begin with, the transducer lowest to the slope exhibited a higher pressure than in other cases, i.e., transducer 3 in the 10 - degree case exhibited higher pressure values than the corresponding transducer in the 0 - and 5 - degree cases, as indicated in Figure 6.8 (b). Furthermore, the initial impact on the transducer located at the same level occurred earlier in the steeper case, which demonstrated that the steeper slope could lead to a faster wave arrival at a certain location. For instance, the initial impact on transducer 3 in the 10 - degree case was 0.02 s and 0.06 s ahead of the impact time in the 5 - and 0 - degree cases, respectively, as demonstrated in Figure 6.8 (b). Due to a greater volume of water accumulating onto the slope instead of running up higher, the duration of pressure peak around the second peak was longer in the steeper slope case, i.e., the pressure peaks which occurred around 1.05 s in the 15-degree case was wider than the peaks for the 10 -, 5 - degree and horizontal bed cases.

Negative pressure was registered by the top transducer 5 around 0.5 s in all cases, as illustrated in Figure 6.8 (d). It should be noticed that the maximum amplitude of negative pressure in the 5- and 10-degree cases were larger than the one observed for the horizontal case, -0.65 kPa and -0.62 kPa, respectively, when compared with 0.59 kPa, while a smaller negative pressure peak was observed in the15-degree slope: -0.39 kPa. A reasonable explanation could be given that the wave propagated faster along the location of transducer 5 in the steeper bed slopes, which resulted in stronger suction effects that that observed in the 5 - and 10 - degree slopes.

6.4.5 Comparison of impact force by experiments and numerical simulation

The estimated experimental impact forces were obtained by integrating the time history of the dynamic pressure for the 0 -, 5 -, 10 - and 15 - degree cases. The experimental force time-histories are presented in Figure 6.9, where they are compared with the results numerically calculated by OpenFOAM and DualSPHysics. Overall, the OpenFOAM better reproduced the force in horizontal case, whereas DualSPHysics returned better force time-history results for the sloped beds.

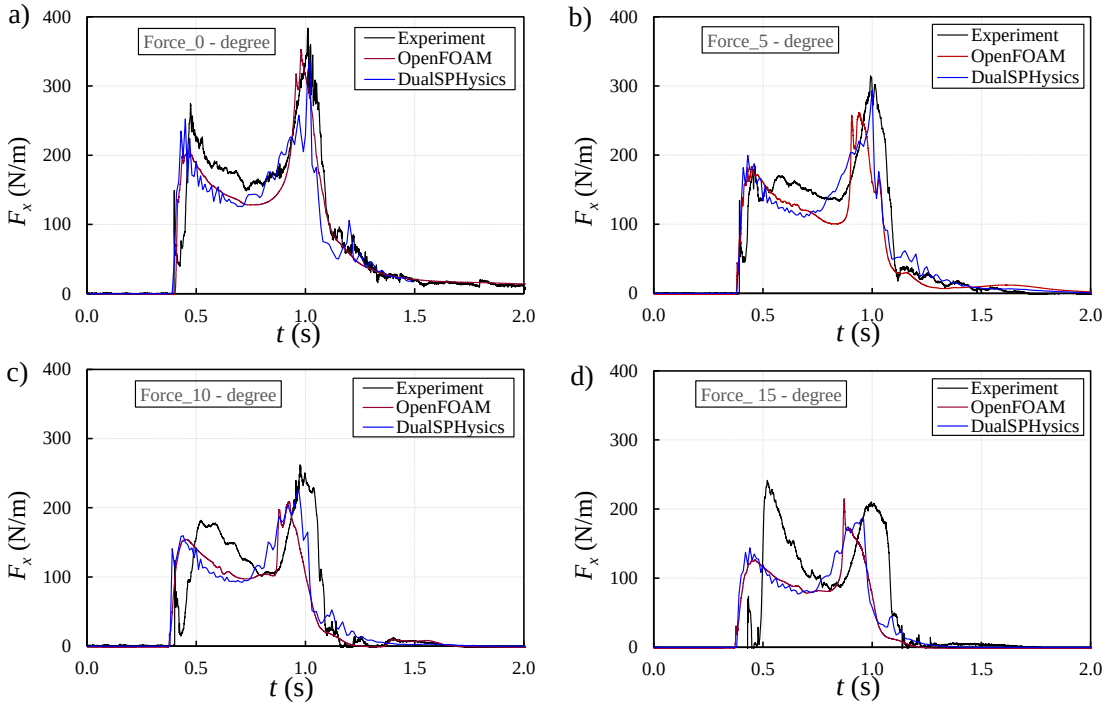

Figure 6.9 Comparison of the time-history of the impact force on the right wall from experiment and numerical simulations using the OpenFOAM and DualSPHysics models: (a) 0 - degree; (b) 5 - degree case; (c) 10 - degree case; (d) 15 - degree slopes

In the horizontal bed case, the dynamic pressure of all five transducers were used in the calculation of the force. Good agreement was observed between the integrated experimental

force and the numerically simulated forces, as shown in Figure 6.9 (a). Due to the pressure spike after initial impact, the overall integrated force in the horizontal bed case was lower than the numerical simulation results for the segment around 0.4 s - 0.5 s, and then increased and was 30 N/m higher than results of both OpenFOAM and DualSPHysics models from 0.5 s to 0.7 s. Next, good agreement was observed between the experimental data and numerical simulation before the second peak until the surge fell during 0.7 s to 1.2 s.

From the initial impact until the second force peak in the inclined cases, a similar trend can be observed on the time history of the hydrodynamic force obtained from the experimental tests and numerical simulations, but with discrepancies due to insufficient experimental pressure data involved in the calculation, as shown in Figure 6.9 (b), (c) and (d). In the force calculation from experiments, higher values were obtained after the initial impact in the 5-degree slope - around 25 N/m larger than the numerical results. As the slope increased, the first force peak in the 10 - and 15 - degree cases became sharp and much higher than the numerical simulation, i.e., 50 N/m and 120N/m higher, respectively. Afterwards, the force decreased and reached a short plateau period around 0.8 s, with approximate values of 145 N/m, 100 N/m and 84 N/m in the 5 -, 10 - and 15 - degree cases separately.

The force comparison presented in Figure 6.9 revealed that the maximum experimental impact force generated by the dam break wave occurred during the second peak around 1.0 s when the surge fell back along the wall (Liu et al., 2022b) instead of at the initial impact, with maximum values of 383.7 N/m, 314.5 N/m, 262.23 N/m in the 0 -, 5 -, and 10 - degree slope, respectively.

To summarize, both OpenFOAM and DualSPHysics models could predict the impact force of a dam break wave with reasonable accuracy in terms of the time history data and particularly of its maximum values which is crucial from a practical point of view.

6.4.6 Comparison of experimental impact force

The time-history of the resultant impact forces obtained by integrating experimental dynamic pressures for all cases are presented together in Figure 6.10.

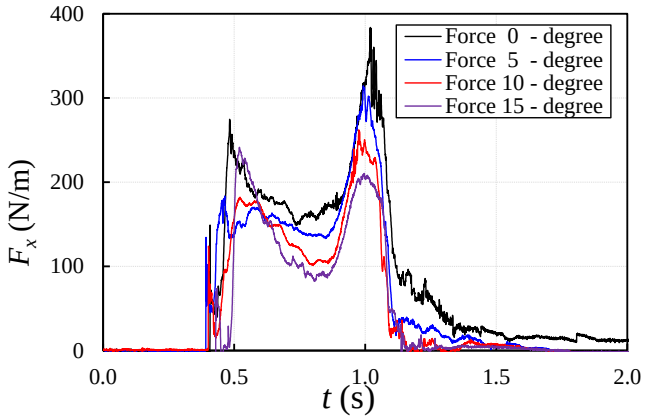

Figure 6.10 Time-history of the impact force obtained from the integration of the experimental dynamic pressure

Overall, the magnitude of the impact force decreased in steeper slope cases, except the overestimated first peak force around 0.5 s for the 15 - degree slope. Considering the numerical simulated force as 150 N/m at the first peak for the 15-degree slope, the maximum impact force at the first peak was 91.38 N/m, 104.4 N/m and 130.82 N/m lower than the horizontal case for the 5 -, 10 - and 15 - degree slopes, respectively. The maximum impact force of the dam break wave occurring around 1.0 s decreased by 18.04%, 31.66% and 45.19% in the 5 -, 10 - and 15 - degree cases, respectively, when compared with the value of 383.73 N/m for the horizontal bed case. There was also a decrease in the force for the sloped beach cases during the plateau period

between the first and second peak, which dropped by an average of 20 N/m, 50 N/m and 65 N/m from the 5 - to 15 - degree cases when compared with the horizontal bed case.

In addition to the numerical comparison, the integrated force in the horizontal bed case was also compared with the forces calculated using the provisions of SMBTR (Okada et al., 2005c) and ASCE - 7/22 (ASCE 2022) to evaluate the applicability of the simplified estimation method, as indicated in Figure 6.11.

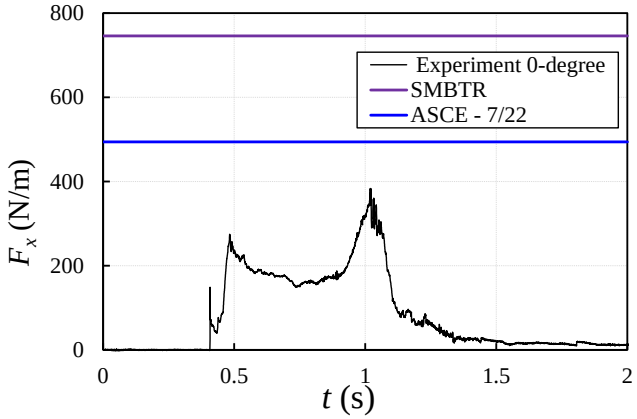

Figure 6.11 Force Comparison between experimental time-history of the force and the value calculated using the provisions of ASCE - 7/22 and SMBTR

The maximum impact force calculated according to SMBTR and ASCE - 7/22 were 746 N/m and 494 N/m, which are 94.4% and 28.7% higher than the integrated force, respectively. It can be observed that the tsunami loads based on formulas from both SMBTR and ASCE - 7/22 were more conservative when compared with the experimentally obtained force.

6.4.7 Force reduction factor

To investigate the relation between force, decrease and bed slope, the decrease ratio in Section 4.6 was defined as a dimensionless reduction factor η, together with the tangent values of bed slope presented in Figure 6.12.

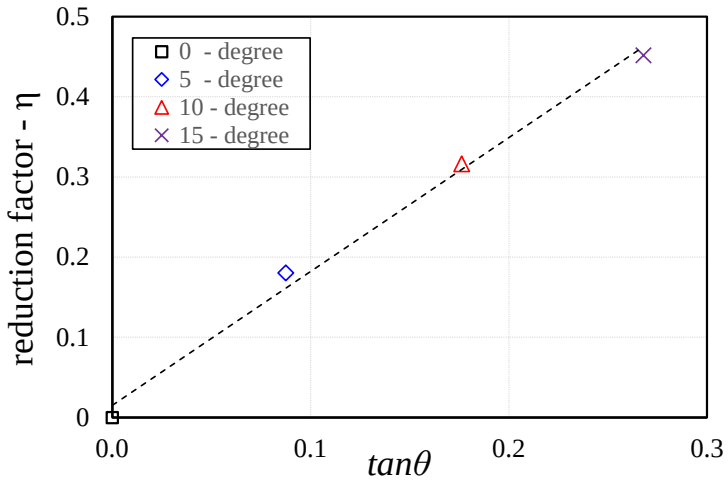

Figure 6.12 Relation of impact force reduction factor and tangent value of bed slopes.

A perfect linear fitness can be obtained between the reduction factor and the tangent values of bed slopes, which demonstrated that the reduction factor can be calculated by the formula of slope. In order to involve the scale effects, the dimensionless reduction factor, η can be expressed by equation:

$$\eta = \sqrt{\frac{L_0}{H}} \tan\theta \tag{6.15}$$

Where, L_0 is the length between the reservoir and the vertical wall, H is the initial impoundment depth, θ is the bed slope.

6.5 Discussion

The present study was conducted to investigate the slope effects on the hydrodynamic loading generated by a dam break flow impact on a vertical wall in terms of dynamic pressure and integrated impact force, using an experimental approach and numerical modeling. In previous experimental work on the dam break flow on a horizontal bed, the time history of the dynamic pressure was shown to be similar and consistent with the previous physical tests (Kamra et al., 2018; Lobovsky et al., 2014; Shen et al., 2020). Unlike the previous experimental research (Lobovsky et al., 2014) and the numerical study in this paper, negative pressure was qualitatively monitored by transducer 5 in all tests. This is attributed to the negative pressure ("suction") effects of the rapidly running up surge.

In the previous research on tsunami-like waves on structures, the horizontal impact force initially increased to a peak value then gradually decreased for the case of slender structures (Nouri et al., 2010), while further steadily fluctuating since the impact was observed for the partially-blocking structure (Wuthrich et al., 2018a, 2018b). However, in this study, the horizontal impact force first increased to the first smaller peak value, then further decreased and held steady in a short plateau area, followed by the s second peak, and finally decreased to zero along with the wave after it receded. This observation revealed that the pattern of the interaction between the dam break wave and fully-blocking structure was different than that observed for the case of slender structures (Nouri et al., 2010) or of the partially-blocking ones (Wuthrich et al., 2018a, 2018b).

The hydrodynamic force comparison study proved that the simplified force integrated formula could predict the peak value of the impact force, for both the propagation of the bore

over the horizontal and inclined beach slopes. When compared with the maximum impact force prescribed by the provisions of SMBTR and ASCE - 7/22, it was shown that both the SMNTR and ASCE - 7/22 return a conservative force calculation. By comparison, ASCE - 7/22 exhibited a maximum force closer to the maximum experimental force in this study, while the force calculated using the SMBTR was almost twice as large as the experimentally-determined force.

To consider the scale effects, the dimensionless factor, η was proposed and presented with its calculation equation, which is similar to the surf similarity parameter (Safari Ghaleh et al., 2021; Yamini et al., 2017). This reduction factor was first presented in dam-break research to estimate the slope effects on the maximum impact force. It should be noted that the equation was derived based on the experimental data with limited number of slopes and one bed length. Future study should be carried out to consider different bed lengths and slopes to further investigate and develop a potential equation to be adapted to wider situations, i.e., consider the bed and slope roughness caused by amors (Safari Ghaleh et al., 2021; Yamini et al., 2017) .

This study provided a simplified methodology to predict the impact force on a fully-flow blocking fixed structure wall by using experimental observations and numerical modeling. It should be noticed that the discrepancies between the force determined from experiments and that from the numerical simulations were mainly caused by insufficient spatially distributed pressure data, a fact more obvious in the sloped beach cases. Thus, the experiments can be improved by installing more closely spaced pressure transducers on the wall, something which would lead to more detailed spatial distribution of the dynamic pressure. To better validate the force calculation method in current research, a specifically designed force load cell can be installed at the wall bottom to measure and record more components of hydrodynamic loading, i.e., force and

moments in all directions (Wuthrich et al., 2018a, 2018b, 2019b). Furthermore, regarding the current experiment, conducting it in a longer tank, employing beaches with different slopes and bed roughness, as well as investigating the scale effects on the experimental results should be taken into consideration in future studies.

6.6 Conclusions

Beach slope effects on the hydrodynamic loading generated by a tsunami-like bore onto a fully-blocking flow wall was investigated in this study via both experimental monitoring and numerical simulations using two models, OpenFOAM and DualSPHysics. The experimental dynamic pressure and the integrated impact force were compared with the numerical simulation, and two of the existing design codes for the latter. A dimensionless reduction factor was first presented to estimate the slope effects on the impact force of dam-break flow. The conclusions are summarized as follows:

- Good agreement between the experimental dynamic pressure and the numerically-calculated ones using by OpenFOAM and DualSPHysics was observed. This demonstrated that the recorded pressure data by miniatured transducers was reliable. The pressure comparison between the first and second lowest transducers showed that the slope decreased the maximum value of the first peak pressure whereas the pressure values around the second peak were close in magnitude. Furthermore, the slope increased the dynamic pressure of the transducers located at the same level when compared with the gentler slope cases.
- The force comparison between the experimental data and the numerical results demonstrated that the proposed simplified force estimation method and formula can adequately predict the impact force exerted over the entire wall area by integrating the dynamic pressure data.

- The experimental force comparison revealed that the slope reduced the impact force of exerted on the wall. Furthermore, the experimental results exhibited that dynamic pressure exerted at lower levels plays a significant role on the magnitude of the peak impact force. Thus, it can be feasible to predict the impact force of dam-break wave by installing limited pressure transducers on the lower area of the infrastructure wall.
- Regarding the trends and maximum values of impact force between experiments and numerical simulation, the good agreement demonstrated the feasibility of the simplified calculation methodology for the calculation of horizontal resultant force. However, it was shown that the maximum design forces prescribed by the provisions of ASCE - 7/22 and SMBTR are conservative.
- A linear fitness was demonstrated between the force reduction ratios and tangent values of bed slopes, which demonstrated to be a reasonable method for developing an equation for the reduction factor. The dimensionless reduction factor and its formula obtained in this study demonstrated a new approach in the hydrodynamic loading study of dam-break flow, which could be extended to other different situations.

The experimental results, numerical simulation and findings of this study can be of assistance to coastal engineering in the case where the estimation of impact force due to tsunami inundation on infrastructure and slope effects needs to be taken into consideration.

Chapter 7 Conclusions and Recommendations for Future Work

7.1 Conclusions

The objective of the present study was to investigate the effects of inclined beaches on the propagation, kinematics and hydrodynamic loading of tsunami-like waves. In order to achieve this goal, a series of dam break experiments were designed and conducted in a glass tank equipped with several bed slopes. Several pressure transducers and sonic sensor were used to capture the hydrodynamic features of the dam-break wave and its impact on the right vertical wall of the tank. In addition, numerical simulations using OpenFOAM and a modified DualSPHysics were conducted to reproduce the results of the physical tests and provide comparisons of the numerical data with those of the experimental results. The conclusions are summarized in this chapter.

In the first part (Chapter 3), the study of solid boundary treatment in SPH was conducted to numerically investigate the performance of the ghost particle method and dynamic boundary condition method. The numerical results demonstrated that ghost particle method can simulate the fluid closer to the solid boundary, but the dynamic boundary condition method can actually eliminate the particle leakage. For the global accuracy of numerical simulation, the dynamic boundary condition is recommended. Furthermore, in the numerical study of parts 3 and 4, a modified dynamic boundary condition (mDBC) was applied in the DualSPHysics model to better simulate the free surface profile and capture the dynamic pressure with improved stability and accuracy.

In the second part (Chapter 4), a glass tank equipped with gate system, measurement devices were applied to investigate the various dynamic features of the impact of the dam-break wave over a horizontal dry bed on the vertical right wall. The maximum wave run up height on the wall was found to be ratio-correlated to the initial impoundment depth *H*, 2.1, 2.15, 2.35 times for the cases of *H*= 200mm, 250mm and 300mm, respectively. The experimental results revealed an inverse relation between the exerted dynamic pressure and surge height on the right wall. The ratio of dynamic pressure to static pressure caused by the surge height demonstrated the dominant role of the dynamic pressure during the impact.

The third part (Chapter 5) was designed to investigate the effects of bed slope on the kinematics of dam-break wave by adding four bed slopes in front of and against the right wall of the tank apparatus. The digitized free water surface profile comparison between test cases revealed that the wave shape only changed when running over the bed slopes, while it remained the same during its propagation onto horizontal bed section. The slope decelerated the wave runup on the wall and, thus, lower surge heights were observed in the sloped cases when compared to the propagating over horizontal bed. The test results also demonstrated the deceleration effects of slope on the wave propagation, a fact revealed by the calculated average wavefront velocity.

In the fourth part (Chapter 6), the bed slope effects on the hydrodynamic loading onto the wall were investigated both experimentally and numerically in OpenFOAM and DualSPHysics. The comparison study showed good performance of OpenFOAM and DualSPHysics in reproducing the physical tests results. The experimental results revealed that the bed slope reduced the peak pressure exerted onto the wall, for the first and second lowest pressure

transducers. The comparison between the experiments and numerical simulation demonstrated that the simplified force calculation method could be used to predict the maximum impact loading. While comparing the impacting force observed in the horizontal bed case with those proposed by some of the current design codes, it was found that the ASCE - 7/22 and SMBTR formulae were conservative. Based on the linear relation between the ratio of force decrease to the slopes employed, a force reduction factor was proposed to estimate the slope effects on hydrodynamic loading due to the dam-break wave.

7.2 Recommendations for future studies

This study provided a comprehensive investigation on the hydrodynamic loading due to tsunami-like bores on a wall, using experimental tests and numerical simulations; in particular, the bed slope effects were investigated. However, there may be some limitations due to the experimental techniques and numerical simulation methodologies, which could be improved in the future research work.

- The boundary treatment method in the SPH models has been an intense research subject and is still work in progress due to its significant effect on the numerical results. The dynamic boundary condition method) was studied and showed better performance when compared with other methods and its modified version (mDBC) was successfully applied in the numerical simulation of this study. The boundary treatment methods could be studied further to ensure a more accurate and physically-meaningful results.
- The relationship between the dynamic pressure at the lowest transducer and surge height was investigated and presented. However, different from some studies, there was a second spike after the initial peak pressure in which was recorded by the lowest transducer which will need to be investigated further. Furthermore, newer pressure transducers could be applied in this experimental setting to improve the accuracy and precision of the measurements.
- The experiments were conducted using smooth plexiglass bed to investigate the characteristics of dam-break wave propagation. However, in real coastal areas, bed roughness is an important factor which should be included in future studies to

simulate the real coastal conditions. As the experiments were conducted in a 1.1 m rectangular tank with 3 different bed slopes, larger flumes fitted with a wider range of slopes to reduced scale effects should be considered in future studies.

- Velocity monitoring using advanced methods such as Particle Image Velocimetry is recommended to better understand the dynamics of the bore propagation.

Appendix: Wall Effects and Air Entrainment in Dam-break Experiment

A.1 Wall effects

In the experimental investigation of this study, a glass tank was applied to investigate the characteristics of dam-break wave in laboratory. The right wall of the tank was used to simulate the vertical wall of the coastal infrastructures. It should be noticed that in the practical coastal engineering, there is no side and left walls which formed the reservoir in experiment, together with the gate for generating wave.

For the dam-break experiments in a tank or flume, there will be wall effects which will affect the wave propagation close to the side walls. For example, in Figure 4.5 (b) at t=0.233ss, the wave front near the side wall was slightly dragged due to the wall roughness. Further in Figure 4.5 (c) at t=0.4167s, it can be observed that the wave front initially impacted on the right wall in the middle area. However, there is no impact phenomenon for the wave front near the side wall which demonstrated that the wall decelerated the wave propagation. In Figure 4.5 (d) at t=0.7667s, the main sketch of the wave flow on the could be clearly observed on the side wall, but there is splashing wave near the side walls. Thus, there will be slightly asynchronous differences in the wave propagation in the middle and side areas. This asynchronous phenomenon could explain the tiny discrepancies in the well-matched pressure curves from the transducers at same level, as shown in Figure 4.4.

In the real tsunami event, the wave propagated to the shoreline in wide range, sometime to tens of kilometres. In this situation, the wall effects in this study could be negligible when considering wave impact on infrastructures.

A.2 Air entrainment

In the free surface profile study, it can be observed that after the stages of wave falling down and rotating back, a cavity formed with air entrained inside, as shown in Figure 4.5 (d) and (e). When the wave rotated back and developed further, the cavity was compressed by the wave, breaking together with the plunging wave, as shown in Figure 4.5 (f) at t=1.1833s.

The cavity formed by air entrainment can be captured by numerical simulation (Peng et al., 2021; Liu et al., 2018). However, in the experimental study, the air entrainment was not obvious especially when the cavity was compressed by the rotating and falling wave. Meanwhile, due to wall effects, the asynchronously developed splashing wave will also affect the observation of air entrainment.

During the air entrained cavity and plunging wave breaking, there will be remarkable kinematic energy dissipation (Lubin et al., 2006; Bahmanpouri et al., 2021; Felder et al., 2018). Thus, the returning back wave only climbed to half of the initial impoundment depth on the left wall. Also, the breaking plunging wave and entrained air will lead impact force on the bed which can enhance the process of sediment transport(Felder et al., 2018). This phenomenon was not observed in current test as rigid bed was applied in the tank.

References

Nistor I., Saatcioglu M., and Ghobarah A. 2005. "The 26 December 2004 Earthquake and Tsunami Hydrodynamic forces on physical infrastructure in Thailand and Indonesia." In *Proceedings 2005 Canadian Coastal Engineering Conference.* Halifax, Canada.

Saatcioglu M., Ghobarah A., and Nistor I. 2005. 'Effects of the December 26, 2004 Sumatra earthquake and tsunami on physical infrastructure', *ISET Journal of Earthquake Technology*, 42: 79-94.

Ghobarah A., Saatcioglu M., and Nistor I. 2006. 'The impact of the 26 December 2004 earthquake and tsunami on structures and infrastructure', *Engineering Structures*, 28: 312-326.

Palermo D., Nistor I., Saatcioglu M., and Ghobarah A. 2013. 'Impact and damage to structures during the 27 February 2010 Chile tsunami', *Canadian Journal of Civil Engineering*, 40: 750-758.

Mikami T., Shibayama T., Esteban M., Takabatake T., Nakamura R., Nishida Y., Achiari H., Rusli, Marzuki A. G., Marzuki M. F. H., Stolle J., Krautwald C., Robertson I., Aránguiz R., and Ohira K. 2019. 'Field Survey of the 2018 Sulawesi Tsunami: Inundation and Run-up Heights and Damage to Coastal Communities', *Pure and Applied Geophysics*, 176: 3291-3304.

Palermo D., Nistor I., Nouri Y., and Cornett A. 2009. 'Tsunami loading of near-shoreline structures: a primer', *Canadian Journal of Civil Engineering*, 36: 1804-1815.

Nouri Y., Nistor I., Palermo D., and Cornett A. 2010. 'Experimental Investigation of Tsunami Impact on Free Standing Structures', *Coastal Engineering Journal*, 52: 43-70.

Al-Faesly T., Palermo D., Nistor I., and Cornett A. 2012a. 'Experimental modeling of extreme hydrodynamic forces on structural models', *International Journal of Protective Structures*, 3(4): 477-505.

Yeh H., Barbosa A., Ko H., and Cawley J. 2014. "Tsunami loadings on structures: Review and analysis." In *Coastal Engineering Proceedings*.

Suppasri A., Pakoksung K., Charvet I., Chua C., Takahashi, Ornthammarath T., Latcharote P., Leelawat N., Fumihiko, and Imamura. 2019. 'Load-resistance analysis : An alternative approach to tsunami damage assessment applied 1 to the 2011 Great East Japan tsunami', *Nat. Hazards Earth Syst. Sci.*, 19: 1807-1822.

Chanson H. 2005. "Analytical Solution of Dam Break Wave With Flow Resistance . Application To Tsunami Surges." In *31st IAHR Biennial Congress*, 3341-3353. Seoul, Korea.

Chanson H. 2006a. 'Tsunami Surges on Dry Coastal Plains: Application of Dam Break Wave Equations', *Coastal Engineering Journal*, 48: 355-370.

Ginting B., and Mundani R.-P. 2019. 'Comparison of Shallow Water Solvers: Applications for Dam-Break and Tsunami Cases with Reordering Strategy for Efficient Vectorization on Modern Hardware', *Water*, 11: 639.

St-Germain P., Nistor I., and Townsend R. 2012. "Numerical modeling of tsunami-induced hydrodynamic forces on onshore structures using SPH." In *In Proc. of the 33rd Int. Conf.*

on Coast. Eng., structures. 81. Santander, Sapin, 1-6 July 2012: ASCE: Reston, VA, USA.

Wuthrich D., Pfister M., and Schleiss A. J. 2019a. 'Effect of bed roughness on tsunami-like waves and induced loads on buildings', *Coastal Engineering*, 152.

Kamra M. M., Mohd N., Liu C., Sueyoshi M., and Hu C. H. 2018. 'Numerical and experimental investigation of three-dimensionality in the dam-break flow against a vertical wall', *Journal of Hydrodynamics*, 30: 682-693.

Lauber G., and Hager W. H. 1998. 'Experiments to dambreak wave: Horizontal channel', *Journal of Hydraulic Research*, 36: 291-307.

Lobovsky L., Botia-Vera E., Castellana F., Mas-Soler J., and Souto-Iglesias A. 2014. 'Experimental investigation of dynamic pressure loads during dam break', *Journal of Fluids and Structures*, 48: 407-434.

Chanson H. 2009. 'Application of the method of characteristics to the dam break wave problem', *Journal of Hydraulic Research*, 47: 41-49.

Kleefsman K. M. T., Fekken G., Veldman A. E. P., Iwanowski B., and Buchner B. 2005. 'A Volume-of-Fluid based simulation method for wave impact problems', *Journal of Computational Physics*, 206: 363-393.

Zhou Z. Q., Kat J. O. D., and Buchner B. 1999. "A nonlinear 3D approach to simulate green water dynamics on deck." In *7th Int. Conf. on Numer. Sh. Hydrodyn.* Nantes, France, 31 Dec 1998.

Wuthrich D., Pfister M., Nistor I., and Schleiss A. J. 2018a. 'Experimental study on forces exerted on buildings with openings due to extreme hydrodynamic events', *Coastal Engineering*, 140: 72-86.

Wuthrich D., Pfister M., Nistor I., and Schleiss A. J. 2018b. 'Experimental study on the hydrodynamic impact of tsunami-like waves against impervious free-standing buildings', *Coastal Engineering Journal*, 60: 180-199.

Sánchez-Cordero E., Gómez M., and Bladé E. 2017. 'Three-dimensional numerical analysis of a dam-break using OpenFOAM', *Proc. of the Inst. for System Program. of the RAS*, 29: 311-320.

Xie P., and Chu V. H. 2019. 'The forces of tsunami waves on a vertical wall and on a structure of finite width', *Coastal Engineering*, 149: 65-80.

Nguyen V.-B., Do Q.-V., and Pham V.-S. 2020. 'An OpenFOAM solver for multiphase and turbulent flow', *Phy. of Fluids*, 32: 043303.

Larocque L. A., Imran J., and Chaudhry M. H. 2013. '3D numerical simulation of partial breach dam-break flow using the LES andk–ϵ turbulence models', *Journal of Hydraulic Research*, 51: 145-157.

Evtushok G. Y., Boiko A. V., Yakovenko S. N., Yakovenko E. E., and Chang K. C. 2021. 'MODIFICATION AND VERIFICATION OF NUMERICAL ALGORITHMS FOR DAM-BREAK FLOW OVER A HORIZONTAL BED', *Journal of Applied Mechanics and Technical Physics*, 62: 255-265.

Gomez-Gesteira M., Rogers B. D., Crespo A. J. C., Dalrymple R. A., Narayanaswamy M., and Dominguez J. M. 2012a. 'SPHysics – development of a free-surface fluid solver – Part 1: Theory and formulations', *Comput. & Geosci.*, 48: 289-299.

Crespo A. J. C., Domínguez J. M., Rogers B. D., Gómez-Gesteira M., Longshaw S., Canelas R., Vacondio R., Barreiro A., and García-Feal O. 2015a. 'DualSPHysics: Open-source parallel CFD solver based on Smoothed Particle Hydrodynamics (SPH)', *Comput. Phys. Commun.*, 187: 204-216.

Gu S., Zheng X., Ren L., Xie H., Huang Y., Wei J., and Shao S. 2017. 'SWE-SPHysics Simulation of Dam Break Flows at South-Gate Gorges Reservoir', *Water*, 9: 387.

English A., Domínguez J. M., Vacondio R., Crespo A. J. C., Stansby P. K., Lind S. J., Chiapponi L., and Gómez-Gesteira M. 2021. 'Modified dynamic boundary conditions (mDBC) for general-purpose smoothed particle hydrodynamics (SPH): application to tank sloshing, dam break and fish pass problems', *Comput. Part. Mech.*, 9: 911-925.

English A., Domínguez J. M., Vacondio R., Crespo A. J. C., Stansby P. K., Lind S. J., and Gómez-Gesteira M. 2019. "Correction for Dynamic Boundary Conditions." In *Proc. of the 14th Int. SPHERIC Workshop*. Exeter, UK, 25-27 June 2019.

Peng L., Zhang T., Rong Y., Hu C., and Feng P. 2021. 'Numerical investigation of the impact of a dam-break induced flood on a structure', *Ocean Engineering*, 223: 108669.

ASCE. 2022. *Minimum design loads and associated criteria for buildings and other structures: ASCE/SEI 7-16* (American Society of Civil Engineers: Reston, Virginia, USA).

Okada T., Sugano T., Ishikawa T., Ohgi T., Takai S., and Hamabe C. 2005a. "Structural Design Methods of Buildings for Tsunami Resistance (SMBTR)." In. Japan: The Building Centre of Japan.

Satake K. 1988. 'Effects of bathymetry on tsunami propagation: Application of ray tracing to tsunamis', *Pure and Applied Geophysics*, 126: 27-36.

Nistor I., Palermo D., Cornett A., and Al-Faesly T. 2011. 'Experimental and Numerical Modeling of Tsunami Loading on Structures', *Coastal Engineering Proceedings*, 1: currents.2.

Saint-Venant A. B. d. 1871. 'Théorie du mouvement non permanent des eaux, avec application aux crues des rivières et à l'introduction de marées dans leurs lits', *Comptes Rendus des Séances de l'Académie des Sciences*, 73: 147-154 and 237-240.

Ritter A. 1892. 'Die Fortpflanzung der Wasserwellen (The propagation of water waves)', *Zeitschrift verein Deutscher Ingenieure*, 36: 947-954.

Castro-Orgaz O., and Chanson H. 2017a. 'Ritter's dry-bed dam-break flows: positive and negative wave dynamics', *Environmental Fluid Mechanics*, 17: 665-694.

Deng X. H., Liu H. J., and Lu S. X. 2018. 'Analytical Study of Dam-Break Wave Tip Region', *Journal of Hydraulic Engineering*, 144.

Yang S., Yang W., Qin S., and Li Q. 2018a. 'Comparative study on calculation methods of dam-break wave', *Journal of Hydraulic Research*, 57: 702-714.

St-Germain P., Nistor I., Townsend R., and Shibayama T. 2014. 'Smoothed-Particle Hydrodynamics Numerical Modeling of Structures Impacted by Tsunami Bores', *Journal of Waterway Port Coastal and Ocean Engineering*, 140: 66-81.

Rossetto T., Allsop W., Charvet I., and Robinson D. I. 2011. 'Physical modelling of tsunami using a new pneumatic wave generator', *Coastal Engineering*, 58: 517-527.

Nistor I., Goseberg N., Stolle J., Mikami T., Shibayama T., Nakamura R., and Matsuba S. 2017. 'Experimental Investigations of Debris Dynamics over a Horizontal Plane', *Journal of Waterway Port Coastal and Ocean Engineering*, 143: 04016022.

Stolle J., Takabatake T., Hamano G., Ishii H., Iimura K., Shibayama T., Nistor I., Goseberg N., and Petriu E. 2019a. 'Debris transport over a sloped surface in tsunami-like flow conditions', *Coastal Engineering Journal*, 61: 241-255.

Dressler R. F. 1952. 'Hydraulic Resistance Effect Upon the Dam-Break Functions', *Journal of Research of the National Bureau of Standards*, 49: 217-225.

Dressler R. F. 1954. 'Comparison of theories and experiments for the hydraulic dam-break wave', *International Association of Scientific Hydrology*, 3: 319-328.

Martin J. C., and Moyce W. J. 1952. 'An Experimental Study of the Collapse of Liquid Columns on a Rigid Horizontal Plane', *Philosophical Transactions of the Royal Society of London Series a-Mathematical and Physical Sciences*, 244: 312-324.

Stansby P. K., Chegini A., and Barnes T. C. D. 1998. 'The initial stages of dam-break flow', *Journal of Fluid Mechanics*, 374: 407-424.

Hu C. H., and Sueyoshi M. 2010. 'Numerical Simulation and Experiment on Dam Break Problem', *Journal of Marine Science and Application*, 9: 109-114.

Wüthrich D., Pfister M., and Schleiss A. 2016. "Example of wave impact on a residential house." In *In Sustainable Hydraulics in the Era of Globle Change, Proceedings of the 4th IAHR European Congress*, 404-408. Liege,Belgium, 27-29 July 2016: CRC Press: Boca Raton, FL, USA, 2016.

Chanson H. 2006b. "Analytical Solutions of Laminar and Turbulent Dam Break Wave." In *International Conference on Fluvial Hydraulics River Flow*, 465-474. Lisbon, Portugal.

Whitham G. B. 1955. 'The Effects of Hydraulic Resistance in the Dam-Break Problem', *Proceedings of the Royal Society of London Series a-Mathematical and Physical Sciences*, 227: 399-407.

Ozmen-Cagatay H., and Kocaman S. 2010. 'Dam-break flows during initial stage using SWE and RANS approaches', *Journal of Hydraulic Research*, 48: 603-611.

Nguyen-Thi L.-Q., Nguyen V.-D., Pierens X., and Coorevits P. 2021. 'An experimental and numerical study of the influence of viscosity on the behavior of dam-break flow', *Theoretical and Computational Fluid Dynamics*, 35: 345-362.

Yang S., Yang W., Zhang C., Qin S., Wei K., and Zhang J. 2022. 'Experimental and numerical study on the evolution of wave front profile of dam-break waves', *Ocean Engineering*, 247: 110681.

Wang B., Liu X., Zhang J., Guo Y., Chen Y., Peng Y., Liu W., Yang S., and Zhang F. 2020. 'Analytical and Experimental Investigations of Dam-Break Flows in Triangular Channels with Wet-Bed Conditions', *Journal of Hydraulic Engineering*, 146: 04020070.

Leal J. G., Ferreira R. M., and Cardoso A. H. 2006. 'Dam-Break Wave-Front Celerity', *Journal of Hydraulic Engineering*, 132: 69-76.

Castro-Orgaz O., and Chanson H. 2017b. 'Ritter’s dry-bed dam-break flows: positive and negative wave dynamics', *Environmental Fluid Mechanics*, 17: 665-694.

Yilmaz A., Kocaman S., and Demirci M. 2021. 'Numerical modeling of the dam-break wave impact on elastic sluice gate: A new benchmark case for hydroelasticity problems', *Ocean Engineering*, 231: 108870.

Lee T. H., Zhou Z. Q., and Cao Y. S. 2002. 'Numerical simulations of hydraulic jumps in water sloshing and water impact', *Journal of Fluids Engineering*, 124: 215-226.

Wemmenhove R., Gladsø R., Iwanowski B., and Lefranc M. 2010. "Comparison of CFD Calculations And Experiment For the Dambreak Experiment With One Flexible Wall." In *The 20th Int. Offshore and Polar Eng. Conf.* , 6. Beijing, China, June 20 2010: International Society of Offshore and Polar Engineers: Mountain View, CA, USA.

Xie W., and Shimozono T. 2022. 'Water surge impingement onto a vertical wall: Laboratory experiments and stochastic analysis on impact pressure', *Ocean Engineering*, 248: 110422.

Asakura R., Iwase K., Ikeya T., Takao M., Kaneto K., Fujii N., and Omori M. 2000. "An Experimental Study on Wave Force Acting on On-Shore Structures due to Overflowing Tsunamis." In *Int. Proc. of the 28th Int. Conf. on Coast. Eng.*, 1191-1202. Cardiff, Wales, 7-12 July 2002.

Okada T., Sugano T., Ishikawa T., Ohgi T., Takai S., and Hamabe C. 2005b. 'Structural design methods of buildings for tsunami resistance (SMBTR)', *The Building Center of Japan, Japan*.

Chock G. Y. K. 2016. 'Design for Tsunami Loads and Effects in the ASCE 7-16 Standard', *Journal of Structural Engineering*, 142: 04016093.

Stolle J., Takabatake T., Nistor I., Mikami T., Nishizaki S., Hamano G., Ishii H., Shibayama T., Goseberg N., and Petriu E. 2018. 'Experimental investigation of debris damming loads under transient supercritical flow conditions', *Coastal Engineering*, 139: 16-31.

Wuthrich D., Pfister M., Nistor I., and Schleiss A. J. 2019b. 'Effect of building overtopping on induced loads during extreme hydrodynamic events', *Journal of Hydraulic Research*, 58: 289-304.

Zhainakov A. Z., and Kurbanaliev A. Y. 2013. 'Verification of the open package OpenFOAM on dam break problems', *Thermophysics and Aeromechanics*, 20: 451-461.

Sarjamee S., Nistor I., and Mohammadian A. 2017. 'Numerical investigation of the influence of extreme hydrodynamic forces on the geometry of structures using OpenFOAM', *Natural Hazards*, 87: 213-235.

Ferro P., Landel P., Pescheux M., and Guillot S. 2022. 'Development of a free surface flow solver using the Ghost Fluid Method on OpenFOAM', *Ocean Engineering*, 253: 111236.

Gomez-Gesteira. 2013. 'SPHERIC SPH benchmark test cases: Test 1-force exerted by a schematic 3D dam break on a square cylinder'.

Al-Faesly T., Palermo D., Nistor I., and Cornett A. 2012b. 'Experimental Modeling of Extreme Hydrodynamic Forces on Structural Models', *International Journal of Protective Structures*, 3: 477-505.

Noh W. F., and Woodward P. 1976. "SLIC (Simple Line Interface Calculation)." In *Proceedings of the Fifth International Conference on Numerical Methods in Fluid Dynamics June 28 – July 2, 1976 Twente University, Enschede*, edited by Adriaan I. van de Vooren and Pieter J. Zandbergen, 330-340. Berlin, Heidelberg: Springer Berlin Heidelberg.

Hirt C. W., and Nichols B. D. 1981. 'Volume of fluid (VOF) method for the dynamics of free boundaries', *Journal of Computational Physics*, 39: 201-225.

Gomez-Gesteira M., Crespo A. J. C., Rogers B. D., Dalrymple R. A., Dominguez J. M., and Barreiro A. 2012b. 'SPHysics – development of a free-surface fluid solver – Part 2: Efficiency and test cases', *Computers & Geosciences*, 48: 300-307.

Crespo A. C., Dominguez J. M., Barreiro A., Gómez-Gesteira M., and Rogers B. D. 2011. 'GPUs, a New Tool of Acceleration in CFD: Efficiency and Reliability on Smoothed Particle Hydrodynamics Methods', *PLOS ONE*, 6: e20685.

Morris M. 2000. "CADAM: Concerted Action on Dambreak Modeling–Final Report." In. HR Wallingford: Wallingford, UK.

Mokos A., Rogers B. D., Stansby P. K., and Domínguez J. M. 2015. 'Multi-phase SPH modelling of violent hydrodynamics on GPUs', *Computer Physics Communications*, 196: 304-316.

Gingold R. A., and Monaghan J. J. 1977. 'Smoothed Particle Hydrodynamics - Theory and Application to Non-Spherical Stars', *Monthly Notices of the Royal Astronomical Society*, 181: 375-389.

Lucy L. B. 1977. 'Numerical Approach to Testing of Fission Hypothesis', *Astronomical Journal*, 82: 1013-1024.

Monaghan J. J. 1994. 'Simulating Free-Surface Flows with SPH', *Journal of Computational Physics*, 110: 399-406.

Randles P. W., and Libersky L. D. 1996. 'Smoothed Particle Hydrodynamics: Some recent improvements and applications', *Computer Methods in Applied Mechanics and Engineering*, 139: 375-408.

Monaghan J. J., and Kos A. 1999. 'Solitary waves on a Cretan beach', *Journal of Waterway Port Coastal and Ocean Engineering-Asce*, 125: 145-154.

Libersky L. D., Petschek A. G., Carney T. C., Hipp J. R., and Allahdadi F. A. 1993. 'High-Strain Lagrangian Hydrodynamics - a 3-Dimensional Sph Code for Dynamic Material Response', *Journal of Computational Physics*, 109: 67-75.

Liu M. B., Liu G. R., Zong Z., Lam K. Y., and Chen X. L. 2001. 'Numerical simulation of incompressible flows by SPH', *Internatinal Conference On Scientific & Engineeriing Computing*.

Ferrari A., Dumbser M., Toro E. F., and Armanini A. 2009. 'A new 3D parallel SPH scheme for free surface flows', *Computers & Fluids*, 38: 1203-1217.

Dalrymple R. A., and Knio O. 2001. *SPH modelling of water waves* (Amer Soc Civil Engineers: New York).

Gomez-Gesteira M., Cerqueiroa D., Crespoa C., and Dalrymple R. A. 2005. 'Green water overtopping analyzed with a SPH model', *Ocean Engineering*, 32: 223-238.

Gomez-Gesteira M., Rogers B. D., Dalrymple R. A., and Crespo A. J. C. 2010. 'State-of-the-art of classical SPH for free-surface flows', *Journal of Hydraulic Research*, 48: 6-27.

Crespo A. J. C., Gómez-Gesteira M., and Dalrymple R. A. 2007a. 'Boundary conditions generated by dynamic particles in SPH methods', *CMC: Comput. Mater. Contin.*, 5: 173-184.

Shao J. R., Li H. Q., Liu G. R., and Liu M. B. 2012. 'An improved SPH method for modeling liquid sloshing dynamics', *Computers & Structures*, 100: 18-26.

Monaghan J. J., and Lattanzio J. C. 1985. 'A Refined Particle Method for Astrophysical Problems', *Astronomy & Astrophysics*, 149: 135-143.

Monaghan J. J. 1989. 'On the Problem of Penetration in Particle Methods', *Journal of Computational Physics*, 82: 1-15.

Shafieefar M., Valizadeh A., Monaghan J. J., and Salehi Neyshaboori S. A. A. 2008. 'Modeling Two-Phase Flows Using SPH Method', *Journal of Applied Sciences*, 8: 3817-3826.

Morris J. P., Fox P. J., and Zhu Y. 1997. 'Modeling Low Reynolds Number Incompressible Flows Using SPH', *Journal of Computational Physics*, 136: 214-226.

Colagrossi A., and Landrini M. 2003. 'Numerical simulation of interfacial flows by smoothed particle hydrodynamics', *Journal of Computational Physics*, 191: 448-475.

Monaghan J. J. 1992. 'Smoothed Particle Hydrodynamics', *Annual Review of Astronomy and Astrophysics*, 30: 543-574.

Liu M. B., and Li S. M. 2016. 'On the modeling of viscous incompressible flows with smoothed particle hydrodynamics', *Journal of Hydrodynamics*, 28: 731-745.

Crespo A. J. C., Dominguez J. M., Rogers B. D., Gomez-Gesteira M., Longshaw S., Canelas R., Vacondio R., Barreiro A., and Garcia-Feal O. 2015b. 'DualSPHysics: Open-source parallel CFD solver based on Smoothed Particle Hydrodynamics (SPH)', *Comput. Phy. Commun.*, 187: 204-216.

Ramachadran P. 2016. "PySPH: a reproducible and high-performance framework for smoothed particle hydrodynamics." In *Proceedings of the 15th Python in Science Conference*, 127-135.

Ramachandran P., and Puri K. 2013. "PySPH: A framework for parallel particle simulations." In *Proceedings of the 3rd International Conference on Particle-Based Methods*

Crespo A. J. C., Gomez-Gesteira M., and Dalrymple R. A. 2007b. '3D SPH Simulation of large waves mitigation with a dike', *Journal of Hydraulic Research*, 45: 631-642.

Go´mez-Gesteira M., and Dalrymple R. A. 2004. 'Using a three-dimensional smoothed particle hydrodynamics method for wave impact on a tall structure', *Journal of Waterway, Port, Coastal and Ocean Engineering*, 130: 63-69.

Ren B., He M., Dong P., and Wen H. J. 2015. 'Nonlinear simulations of wave-induced motions of a freely floating body using WCSPH method', *Applied Ocean Research*, 50: 1-12.

Shibayama A., Kihara N., Miyagawa Y., Takabatake D., and Kaida H. 2015. "Large Scale Experiments on Response of RC Tide Wall to Tsunami Debris Impact." In *In Proceedings of the Twenty-fifth International Ocean and Polar Engineering Conference*, 5. Kona, Hawaii, USA, 21-26 June 2015.

Nistor I., Palermo D., Nouri Y., Murty T., and Saatcioglu M. 2009. 'Tsunami-Induced Forces on Structures.' in Young C Kim (ed.), *Handbook of Coastal and Ocean Engineering* (World Scientific: Singapore).

Wuthrich D., Pfister M., Nistor I., and Schleiss A. J. 2018c. 'Experimental Study of Tsunami-Like Waves Generated with a Vertical Release Technique on Dry and Wet Beds', *Journal of Waterway Port Coastal and Ocean Engineering*, 144: 04018006.

Stolle J., Ghodoosipour B., Derschum C., Nistor I., Petriu E., and Goseberg N. 2019b. 'Swing gate generated dam-break waves', *Journal of Hydraulic Research*, 57: 675-687.

Häfen H. V., Stolle J., Goseberg N., and Nistor I. "Lift and Swing Gate Modelling For Dam-break Generation With A Particle-Based Method." In *7th IAHR International Symposium on Hydrolic Strcutures*. Aachen, Germany, 15-18 May 2018.

Hernández-Fontes J. V., Vitola M. A., Silva M. C., Esperança P. d. T. T., and Sphaier S. H. 2018. 'On the Generation of Isolated Green Water Events Using Wet Dam-Break', *Journal of Offshore Mechanics and Arctic Engineering*, 140: 051101.

Hernández-Fontes J. V., Esperança P. d. T. T., Graniel J. F. B., Sphaier S. H., and Silva R. 2019. 'Green Water on A Fixed Structure Due to Incident Bores: Guidelines and Database for Model Validations Regarding Flow Evolution', *Water*, 11: 2584.

Hernández-Fontes J. V., Vitola M. A., Esperança P. T. T., Sphaier S. H., and Silva R. 2020a. 'Patterns and vertical loads in water shipping in systematic wet dam-break experiments', *Ocean Engineering*, 197: 106891.

Hernández-Fontes J. V., Esperança P. T. T., Silva R., Mendoza E., and Sphaier S. H. 2020b. 'Violent water-structure interaction: Overtopping features and vertical loads on a fixed structure due to broken incident flows', *Marine Structures*, 74: 102816.

Soares-Frazao S., and Zech Y. 2007. 'Experimental study of dam-break flow against an isolated obstacle', *Journal of Hydraulic Research*, 45: 27-36.

Soares-Frazao S., Canelas R., Cao Z. X., Cea L., Chaudhry H. M., Moran A. D., El Kadi K., Ferreira R., Cadorniga I. F., Gonzalez-Ramirez N., Greco M., Huang W., Imran J., Le Coz J., Marsooli R., Paquier A., Pender G., Pontillo M., Puertas J., Spinewine B., Swartenbroekx C., Tsubaki R., Villaret C., Wu W. M., Yue Z. Y., and Zech Y. 2012. 'Dam-break flows over mobile beds: experiments and benchmark tests for numerical models', *Journal of Hydraulic Research*, 50: 364-375.

Karunya R., Rebeca Roldan G., Hocine O., Stefan S., Matthias K., Koen Van D., Julien De R., Tom V., and Koen T. 2012. "Loading of Vertical Walls by Overtopping Bores using Pressure and Force Sensors - A Large Scale Model Study." In *In Proceedings of Coastal Engineering Proceedings, currents. 44*, currents.44, 41-15. Santander, Spain, 1–6 July 2012: ASCE: Reston, VA, USA , 2012.

Kocaman S., and Ozmen-Cagatay H. 2012. 'The effect of lateral channel contraction on dam break flows: Laboratory experiment', *Journal of Hydrology*, 432: 145-153.

Liu S., Nistor I., and Mohammadian M. 2018. 'Evaluation of the Solid Boundary Treatment Methods in SPH', *International Journal of Ocean and Coastal Engineering*, 01: 1840002.

Kim S.-Y., Kim K.-H., and Kim Y. 2015. 'Comparative study on pressure sensors for sloshing experiment', *Ocean Engineering*, 94: 199-212.

Okada T., Sugano T., Ishikawa T., Ohgi T., Takai S., and Hamabe C. 2005c. "Structural Design Method of Buildings for Tsunami Resistance (SMBTR)." In. Japan: The Building Center of Japan.

Hernández I. D., Hernández-Fontes J. V., Vitola M. A., Silva M. C., and Esperança P. T. T. 2018. 'Water elevation measurements using binary image analysis for 2D hydrodynamic experiments', *Ocean Engineering*, 157: 325-338.

Kocaman S., Güzel H., Evangelista S., Ozmen-Cagatay H., and Viccione G. 2020. 'Experimental and Numerical Analysis of a Dam-Break Flow through Different Contraction Geometries of the Channel', *Water*, 12: 1124.

Hsu H.-C., Torres-Freyermuth A., Hsu T.-J., Hwung H.-H., and Kuo P.-C. 2014. 'On dam-break wave propagation and its implication to sediment erosion', *Journal of Hydraulic Research*, 52: 205-218.

Yang S., Yang W., Qin S., Li Q., and Yang B. 2018b. 'Numerical study on characteristics of dam-break wave', *Ocean Engineering*, 159: 358-371.

Mitchell M., Muftakhidinov B., and Winchen T. 2021. 'Engauge Digitizer Software'. http://markummitchell.github.io/engauge-digitizer.

Shen J., Wei L., Wu D., Liu H., and Huangfu J. 2020. 'Spatiotemporal characteristics of the dam-break induced surge pressure on a vertical wall', *Coastal Engineering Journal*, 62: 566-581.

Lu S. X., Liu H. J., and Deng X. H. 2018. 'An Experimental Study of the Run-Up Process of Breaking Bores Generated by Dam-Break Under Dry- and Wet-Bed Conditions', *J. Earthq. Tsunami*, 12: 1840005.

Kihara N., Niida Y., Takabatake D., Kaida H., Shibayama A., and Miyagawa Y. 2015. 'Large-scale experiments on tsunami-induced pressure on a vertical tide wall', *Coastal Engineering*, 99: 46-63.

Farvizi F., Melville B. W., Shamseldin A. Y., and Shafiei S. 2021. 'Experimental Investigation of Tsunami Bore-Induced Forces on Skewed Deck Girder Section Bridges', *Journal of Hydraulic Engineering*, 147: 04021027.

City and County of Honolulu building code (CCH). 2000. (Department of Planning and Permitting of Honolulu Hawaii: Honalulu, Hawaii, USA).

Liu S., Nistor I., Mohammadian M., and Azimi A. 2022a. "Experimental Investigation of Beach Slope Effects on the Kinemactic Behaviors of Dam Break Flow." In *Proc. of the 39th IAHR World Cong.*, 382. Ganada, Spain, 19-24 June 2022.

Ming F. R., Zhang A. M., Cheng H., and Sun P. N. 2018. 'Numerical simulation of a damaged ship cabin flooding in transversal waves with Smoothed Particle Hydrodynamics method', *Ocean Engineering*, 165: 336-352.

Lind S. J., Rogers B. D., and Stansby P. K. 2020. 'Review of smoothed particle hydrodynamics: towards converged Lagrangian flow modelling', *Proc Math Phys Eng Sci*, 476: 20190801.

Liu S., Nistor I., Mohammadian M., and Azimi A. 2022b. 'Experimental Investigation on the Impact of Dam-break Induced Surges on a Vertical Wall', *Fluids*, 7: 258.

Menter F. R. 1994. 'Two-equation eddy-viscosity turbulence models for engineering applications', *AIAA Journal*, 32: 1598-1605.

Lopez-Jimenez P. A., and Bayon-Barrachina A. 2015. 'Numerical analysis of hydraulic jumps using OpenFOAM', *J. Hydroinf.*, 17: 662-678.

Romanova D., Ivanov O., Trifonov V., Ginzburg N., Korovina D., Ginzburg B., Koltunov N., Eglit M., and Strijhak S. 2022. 'Calibration of the k-ω SST Turbulence Model for Free Surface Flows on Mountain Slopes Using an Experiment', *Fluids*, 7: 111.

Safari Ghaleh R., Aminoroayaie Yamini O., Mousavi S. H., and Kavianpour M. R. 2021. 'Numerical Modeling of Failure Mechanisms in Articulated Concrete Block Mattress as a Sustainable Coastal Protection Structure', *Sustainability*, 13: 12794.

Yamini O. A., Kavianpour M. R., and Mousavi S. H. 2017. 'Wave run-up and rundown on ACB Mats under granular and geotextile filters' condition', *Mar. Georesour. & Geotechnol.*, 36: 895-906.

Lubin P., Vincent S., Abadie S., and Caltagirone J.-P. 2006. 'Three-dimensional Large Eddy Simulation of air entrainment under plunging breaking waves', *Coastal Engineering*, 53: 631-655.

Bahmanpouri F., Daliri M., Khoshkonesh A., Montazeri Namin M., and Buccino M. 2021. 'Bed compaction effect on dam break flow over erodible bed; experimental and numerical modeling', *Journal of Hydrology*, 594: 125645.

Felder S., and Chanson H. 2018. 'Air–Water Flow Patterns of Hydraulic Jumps on Uniform Beds Macroroughness', *Journal of Hydraulic Engineering*, 144.